

## CONTENTS

<b>Andrzej Koszewnik</b> <i>The Parrot UAV Controlled by PID Controllers.....</i>	65
<b>Włodzimierz Balicki, Paweł Głowacki, Stefan Szczeciński, Ryszard Chachurski, Jerzy Szczeciński</b> <i>Effect of the Atmosphere on the Performances of Aviation Turbine Engines.....</i>	70
<b>Wojciech Walendziuk</b> <i>Measurement Uncertainty Analysis of the Strain Gauge Based Stabilographic Platform.....</i>	74
<b>Przemysław Stasiuk, Aleksander Karolczuk, Wiesław Kuczko</b> <i>Analysis of Non-Uniform Distribution of the Equivalent Stress by Selected Multiaxial Fatigue Criteria in Butt-Welded Joint .....</i>	79
<b>Roman Kulchytsky-Zhyhailo, Waldemar Kołodziejczyk</b> <i>Stress Distribution in a Composite Coating by Local Loading of the Free Surface .....</i>	83
<b>Sławomir Romaniuk, Zdzisław Gosiewski</b> <i>Kalman Filter Realization for Orientation and Position Estimation on Dedicated Processor .....</i>	88
<b>Mieczysław Płocica, Jadwiga Pisula</b> <i>The Influence of Changes in the Geometry of the Tooth Surface of the Pinion Bevel Gear on the Kinematic Accuracy of Pair Mesh .....</i>	95
<b>Jozef Bocko, Iveta Glodová, Pavol Lengvarský</b> <i>Some Differential Equations of Elasticity and Their Lie Point Symmetry Generators.....</i>	99
<b>Andrzej Kurek, Adam Niesłony, Marta Kurek</b> <i>Stress Concentration Resulting from Irregular Shape of Explosively Cladded Materials Connections – FEM Simulation.....</i>	103
<b>Adam Tomczyk</b> <i>Friction Effect in a Plane Problem of Punch Acting on a Half-Space Weakened by Cracks .....</i>	107
<i>Abstracts.....</i>	115

## ABSTRACTS

### **Andrzej Koszewnik**

#### *The Parrot UAV Controlled by PID Controllers*

The paper presents the process of modeling and designing control laws for four-rotor type of the Parrot UAV. The state space model is obtained by using several phenomena like gyroscopic effects for rigid bodies, propellers and rotors. The obtained model has been used to design PID control laws for roll, pitch, yaw angle and altitude, respectively. The numerical simulations of the closed loop model are shown that system in satisfy way stabilize flight of the quadro-rotor in all considered directions.

### **Włodzimierz Balicki, Paweł Głowacki, Stefan Szczeciński, Ryszard Chachurski, Jerzy Szczeciński**

#### *Effect of the Atmosphere on the Performances of Aviation Turbine Engines*

The paper presents how the parameters defining the state of the atmosphere: pressure, temperature, humidity, are affecting performance of the aircraft turbine engines and their durability. Also negative impact of dust pollution level is considered as an important source of engine deterioration. Article highlights limitation of the aircraft takeoff weight (TOW) and requirements for length of the runways depending on weather condition changes. These problems stem from the growing "demand" of gas turbine engines for an air. The highest thrust engines have air mass flow more than 1000 kg/s. Engine inlet ice formation is presented as a result of weather conditions and inlet duct design features.

### **Wojciech Walendziuk**

#### *Measurement Uncertainty Analysis of the Strain Gauge Based Stabilographic Platform*

The present article describes constructing a stabilographic platform which records a standing patient's deflection from their point of balance. The constructed device is composed of a toughened glass slab propped with 4 force sensors. Power transducers are connected to the measurement system based on a 24-bit ADC transducer which acquires slight body movements of a patient. The data is then transferred to the computer in real time and data analysis is conducted. The article explains the principle of operation as well as the algorithm of measurement uncertainty for the COP (Centre of Pressure) surface  $(x,y)$ .

### **Przemysław Stasiuk, Aleksander Karolczuk, Wiesław Kuczko**

#### *Analysis of Non-Uniform Distribution of the Equivalent Stress by Selected Multiaxial Fatigue Criteria in Butt-Welded Joint*

Welded joints are areas of increased stresses in construction. The reason for this phenomenon is associated with the nonhomogeneous mechanical, structural and geometrical properties of the weld seams. Generally, in the majority of the calculation it is assumed that the shape of the weld is uniform over the entire length and it is not deviating from the theoretical one. This article shows the distribution of stress in the butt-weld made of S355J2+N steel specimens. The shape of a joint was transferred to the finite element analysis by application of 3D scanning. Selected multiaxial fatigue criteria and probability mass function were used for a description of the results. Theoretical model prepared for comparison to the scanned joints was consistent with recommendations of International Institute of Welding for the effective notch method.

### **Roman Kulchytsky-Zhyhailo, Waldemar Kołodziejczyk**

#### *Stress Distribution in a Composite Coating by Local Loading of the Free Surface*

A three-dimensional problem of the theory of elasticity for halfspace with multilayered coating with periodical structure is considered. The fundamental layer consists of two layers with different thicknesses and different mechanical properties. The coating is described by the homogenized model with microlocal parameters. The solution is derived by using integral Fourier transform. Calculations were conducted with the assumption of elliptical distribution of normal and tangential tractions applied to the surface of the layered system in a circular area. Analysis of the stresses was restricted to the first principal stress distribution.

### **Sławomir Romaniuk, Zdzisław Gosiewski**

#### *Kalman Filter Realization for Orientation and Position Estimation on Dedicated Processor*

This paper presents Kalman filter design which has been programmed and evaluated in dedicated STM32 platform. The main aim of the work performed was to achieve proper estimation of attitude and position signals which could be further used in unmanned aerial vehicle autopilots. Inertial measurement unit and GPS receiver have been used as measurement devices in order to achieve needed raw sensor data. Results of Kalman filter estimation were recorded for signals measurements and compared with raw data. Position actualization frequency was increased from 1 Hz which is characteristic to GPS receivers, to values close to 50 Hz. Furthermore it is shown how Kalman filter deals with GPS accuracy decreases and magnetometer measurement noise.

**Mieczysław Płocica, Jadwiga Pisula**

*The Influence of Changes in the Geometry of the Tooth Surface of the Pinion Bevel Gear on the Kinematic Accuracy of Pair Mesh*

The paper describes the possibilities of bevel gears kinematics design on the basis of the motion graph and improving modifications to cut the pinion teeth flanks. The result is the ability to increase the accuracy of the kinematic transmission. The issue of changing the geometry of the pinion gear is considered in respect of a gear intended for the use in aviation, which requires the cooperation of high quality meshing. The basic geometric features that have been modified include the profile angle, the angle of tooth line, crowning transverse and longitudinal and lateral surface twist angle of the tooth. The modification of each of the selected geometrical parameters has had a different effect on the chart of transmission. It has been shown that the effect of the intended changes in the geometry of the pinion may reduce the deviation of motion delays gear and an improve the gear transmission chart.

**Jozef Bocko, Iveta Glodová, Pavol Lengvarský**

*Some Differential Equations of Elasticity and Their Lie Point Symmetry Generators*

The formal models of physical systems are typically written in terms of differential equations. A transformation of the variables in a differential equation forms a symmetry group if it leaves the differential equation invariant. Symmetries of differential equations are very important for understanding of their properties. It can be said that the theory of Lie group symmetries of differential equations is general systematic method for finding solutions of differential equations. Despite of this fact, the Lie group theory is relatively unknown in engineering community. The paper is devoted to some important questions concerning this theory and for several equations resulting from the theory of elasticity their Lie group infinitesimal generators are given.

**Andrzej Kurek, Adam Niesłony, Marta Kurek**

*Stress Concentration Resulting from Irregular Shape of Explosively Cladded Materials Connections – FEM Simulation*

The paper contains a numerical analysis of interface zone steel-titanium bimetal obtained by explosive cladding method. Due to the waviness of the zone, and various properties of the constituent material of the materials type contain structural notch. Therefore it is important inter alia in terms of presentation of the results of fatigue are the maximum stresses that occur just in the area of the zone. In the paper the stress concentration factor and the proposed method of modelling the joint zone of a sinusoidal profile, characterized by the same coefficient of stress concentration at the actual profile.

**Adam Tomczyk**

*Friction Effect in a Plane Problem of Punch Acting on a Half-Space Weakened by Cracks*

This work makes use of singular integral equations method to solve plane contact problem for a half-space containing cracks. This method is based on complex variables. Relationships are presented which help find the contact pressure under the punch and the value of stress intensity factors at the crack tips. A detailed solution is presented for the problem of a punch pressed to the surface of a half-space weakened by a single straight crack. It includes both a situation where the punch has a flat and parabolic base. The influence of friction and the position of the crack on the distribution of the values of stress intensity factors  $K_{I}$  i  $K_{II}$  in the functions of crack length and distance from the contact zone was analyzed in detail.

# THE PARROT UAV CONTROLLED BY PID CONTROLLERS

Andrzej KOSZEWNIK\*

\*Faculty of Mechanical Engineering, Department of Automatic Control and Robotics, Bialystok University of Technology, ul. Wiejska 45C, 15-131 Bialystok, Poland

[a.koszewnik@pb.edu.pl](mailto:a.koszewnik@pb.edu.pl)

**Abstract:** The paper presents the process of modeling and designing control laws for four-rotor type of the Parrot UAV. The state space model is obtained by using several phenomena like gyroscopic effects for rigid bodies, propellers and rotors. The obtained model has been used to design PID control laws for roll, pitch, yaw angle and altitude, respectively. The numerical simulations of the closed loop model are shown that system in satisfy way stabilize flight of the quadro-rotor in all considered directions.

**Key words:** PID Control, Parrot, Quadro-Rotor, Modeling

## 1. INTRODUCTION

Autonomous Unmanned Air Vehicle (UAV) are increasingly popular platforms, due to their use in military applications, traffic surveillance, environment exploration, structure inspections, mapping and aerial cinematography. For these applications, the ability of quadro-rotor to take off and land vertically, to perform hover flight as well as their agility, make them ideal vehicles.

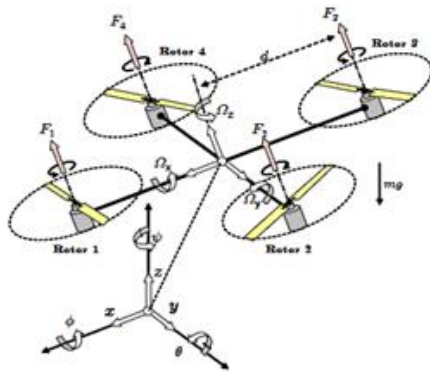


Fig.1. Four-rotor copter and photo of the Parrot

Four rotors helicopters Fig.1 have several basic advantages over manned systems including increased manoeuvrability, low cost, reduced radar signatures. Vertical take-off and landing type

UAV's exhibit further advantages in the manoeuvrability features. Such vehicles require little human intervention from take-off to landing. This helicopter is one of the most complex flying system that exist. This is partly due to the number of physical effects (aerodynamics effects, gravity, gyroscopic, friction and inertial counter torques) acting on the system (Derafa et al., 2007; Kimon, 2007).

Helicopters and quadro-rotors are dynamically unstable and therefore suitable control methods are needed to stabilize them. In order to be able to optimize the operation of the control loop in terms of stability, precision and reaction time, it is essential to know the dynamic behavior of the process which can be established by a representative mathematical model.

## 2. DYNAMIC MODELING OF THE PARROT

The Parrot is equipped with the four-rotor helicopter. Each rotor includes a dedicated brush-less direct current motor, a gear-box and a propeller. The two pairs of propellers (1, 3) and (2, 4) turn in opposite directions. Forward motion is accomplished by increasing the speed of the rear rotor while simultaneously reducing the forward rotor by the same amount. Left and right motion work in same way. Yaw command is accomplished by accelerating the two clockwise rotating rotors while decelerating the counter-clockwise rotating rotors. Parameters of the Parrot are collected in Tab. 1.

Tab. 1. Parameters of the Parrot (Developer Guide SDK 1.7)

Parameter	Value	Meaning
$m$	0.38 kg (outdoor)	Mass (including the support)
$l$	0.17 m	Distance between rotor and center of mass
$\Omega$	28 500 rpm	Max angular speed of the rotor –inrunner -14.5 V
$\eta$	1/8.75	Ratio of angular speed propeller to rotor
$\beta$	8x3.8	Diameter x stroke of propeller

The quadrotor dynamic model is connected with twelve degrees of freedom. The absolute position of the center of mass of quadrotor is described by  $\xi = [x, y, z]^T$  and its attitude by the three Euler's angles  $\alpha = [\varphi, \theta, \psi]^T$ . Moreover the model is described by derivatives of absolute position and Euler's angles  $[\dot{x}, \dot{y}, \dot{z}, \dot{\varphi}, \dot{\theta}, \dot{\psi}]^T$ . These three angles are respectively pitch angle  $(-\frac{\pi}{2} \leq \phi \leq \frac{\pi}{2})$ , roll angle  $-\frac{\pi}{2} \leq \theta \leq \frac{\pi}{2}$  and yaw angle  $-\pi \leq \psi \leq \pi$ .

The dynamic model of the quadrotor describing the roll, pitch and yaw rotations contains three terms which are: the gyroscopic effect resulting from the rigid body rotation, the gyroscopic effect resulting from the propeller rotation coupled with the body rotation and finally the action of the actuators:

$$\begin{aligned} I_{XX}\ddot{\phi} &= \dot{\theta}\dot{\psi}(I_{YY} - I_{ZZ}) + J_r\dot{\theta}\Omega_r + l(-\Omega_2^2 + \Omega_4^2) \\ I_{YY}\ddot{\theta} &= \dot{\phi}\dot{\psi}(I_{ZZ} - I_{XX}) - J_r\dot{\theta}\Omega_r + l(-\Omega_1^2 + \Omega_3^2) \\ I_{ZZ}\ddot{\psi} &= \dot{\phi}\dot{\theta}(I_{XX} - I_{YY}) + J_r\dot{\theta}\Omega_r \end{aligned} \quad (1)$$

where:  $I_{XX}$  – moment of inertia about X axis,  $I_{YY}$  – moment of inertia about Y axis,  $I_{ZZ}$  – moment of inertia about Z axis,  $\Omega_1, \Omega_2, \Omega_3, \Omega_4$  – angular speeds of the rotors,  $\Omega_r$  – angular speed of the propeller

Moreover the quadrotor model describes the position of the Parrot versus the horizon. Neglecting hub forces and friction action, the equations in x,y,z directions are determined via the Newton-Euler formalism:

$$\begin{aligned} m\ddot{z} &= mg - (\cos\psi - \cos\phi) \sum_{i=1}^4 \Omega_i^2 \\ m\ddot{x} &= (\cos\phi\sin\theta\cos\psi + \sin\phi\sin\psi) \sum_{i=1}^4 \Omega_i^2 \\ m\ddot{y} &= (\cos\phi\sin\theta\sin\psi - \sin\phi\cos\psi) \sum_{i=1}^4 \Omega_i^2 \end{aligned} \quad (2)$$

In the next step, the model of the Parrot described by Eq(1) and Eq(2) is simplified, by inserting new constant values ( $a_1, \dots, a_5$  and  $b_1, \dots, b_3$ ), input signals  $U_1, \dots, U_4$  and parameters  $u_x$  and  $u_y$ . Then the model of the quadrotor is transformed to (Clavel et al., 2007):

$$\dot{X} = f(X, U) = \begin{pmatrix} \dot{\phi} \\ \dot{\theta}\dot{\psi}a_1 + \dot{\theta}a_2\Omega_r + b_1U_2 \\ \dot{\theta} \\ \dot{\phi}\dot{\psi}a_3 + \dot{\phi}a_4\Omega_r + b_2U_3 \\ \dot{\psi} \\ \dot{\theta}\dot{\phi}a_5 + b_3U_4 \\ \dot{z} \\ -g + (\cos\phi\cos\theta)\frac{1}{m}U_1 \\ \dot{x} \\ u_x\frac{1}{m}U_1 \\ \dot{y} \\ u_y\frac{1}{m}U_1 \end{pmatrix} \quad (3)$$

with

$$\begin{cases} a_1 = (I_{YY} - I_{ZZ})/I_{XX} & a_5 = (I_{XX} - I_{YY})/I_{ZZ} \\ a_2 = -J_r/I_{XX} & b_1 = l/I_{XX} \\ a_3 = (I_{ZZ} - I_{XX})/I_{YY} & b_2 = l/I_{YY} \\ a_4 = J_r/I_{YY} & b_3 = l/I_{ZZ} \end{cases} \quad (4)$$

and

$$\begin{aligned} u_x &= (\cos\phi\sin\theta\cos\psi + \sin\phi\sin\psi) \\ u_y &= (\cos\phi\sin\theta\sin\psi - \sin\phi\cos\psi) \end{aligned}$$

and

$$\begin{cases} U_1 = b(\Omega_1^2 + \Omega_2^2 + \Omega_3^2 + \Omega_4^2) \\ U_2 = b(-\Omega_2^2 + \Omega_4^2) \\ U_3 = b(\Omega_1^2 - \Omega_3^2) \\ U_4 = d(-\Omega_1^2 + \Omega_2^2 - \Omega_3^2 + \Omega_4^2) \end{cases} \quad (5)$$

where:  $b$  - thrust coefficient of rotor,  $d$  - drag coefficient of rotor.

As we can see in Eq(3) the model of the quadrotor is rewritten in the state space form  $\dot{X} = f(x, u)$  with the inputs vector  $u$  and the state vector  $x$  chosen as follows:

$$\begin{aligned} x &= [\phi \ \dot{\phi} \ \theta \ \dot{\theta} \ \psi \ \dot{\psi} \ z \ \dot{z} \ x \ \dot{x} \ y \ \dot{y}]^T \\ u &= [U_1 \ U_2 \ U_3 \ U_4]^T \end{aligned} \quad (6)$$

Then the obtained model in the state space form is expressed by:

$$\begin{aligned} \dot{X} &= \mathbf{A}x + \mathbf{B}u \\ y &= \mathbf{C}x + \mathbf{D}u \end{aligned} \quad (7)$$

where:

$$\mathbf{A}_{12 \times 12} = \begin{bmatrix} 0 & 1 & 0 & 0 & 0 & 0 & 0 & 0 & 0 & 0 & 0 & 0 \\ 0 & 0 & 0 & a_{24} & 0 & 0 & 0 & 0 & 0 & 0 & 0 & 0 \\ 0 & a_{32} & 0 & 1 & 0 & 0 & 0 & 0 & 0 & 0 & 0 & 0 \\ 0 & 0 & 0 & 0 & 0 & 0 & 0 & 0 & 0 & 0 & 0 & 0 \\ 0 & 0 & 0 & 0 & 0 & 1 & 0 & 0 & 0 & 0 & 0 & 0 \\ 0 & 0 & 0 & 0 & 0 & 0 & 0 & 0 & 0 & 0 & 0 & 0 \\ 0 & 0 & 0 & 0 & 0 & 0 & 0 & 1 & 0 & 0 & 0 & 0 \\ 0 & 0 & 0 & 0 & 0 & 0 & 0 & 0 & 0 & 0 & 0 & 0 \\ 0 & 0 & 0 & 0 & 0 & 0 & 0 & 0 & 0 & 1 & 0 & 0 \\ 0 & 0 & 0 & 0 & 0 & 0 & 0 & 0 & 0 & 0 & 0 & 1 \\ 0 & 0 & 0 & 0 & 0 & 0 & 0 & 0 & 0 & 0 & 0 & 0 \end{bmatrix}$$

where:

$$\begin{aligned} a_{32} &= \psi \cdot a_3 + a_4 \cdot \Omega_r, \\ a_{24} &= \psi \cdot a_1 + a_2 \cdot \Omega_r, \end{aligned}$$

$$\mathbf{B}_{12 \times 4} = \begin{bmatrix} 0 & 0 & 0 & 0 \\ 0 & b_1 & 0 & 0 \\ 0 & 0 & 0 & 0 \\ 0 & 0 & b_2 & 0 \\ 0 & 0 & 0 & 0 \\ 0 & 0 & 0 & b_3 \\ 0 & 0 & 0 & 0 \\ (\cos\phi\cos\theta)/m & 0 & 0 & 0 \\ 0 & 0 & 0 & 0 \\ u_x/m & 0 & 0 & 0 \\ 0 & 0 & 0 & 0 \\ u_y/m & 0 & 0 & 0 \end{bmatrix}$$

$$C_{12 \times 12} = \begin{bmatrix} 1 & \dots & 0 \\ \vdots & \ddots & \vdots \\ 0 & \dots & 1 \end{bmatrix}; \quad D_{12 \times 4} = \begin{bmatrix} 0 & \dots & 0 \\ \vdots & \ddots & \vdots \\ 0 & \dots & 0 \end{bmatrix}$$

The dynamic model of the open loop system is expressed by matrices which values are derived from calculations and assumptions. Some of these parameters are calculated on basic parameters given in Tab.1 and Tab. 2.

**Tab. 2.** The parameters calculated and assumed for simulation (Parrot Ar Drone)

Parameter	Values	Information
$J_{xx}$	0.0086 [kgm <sup>2</sup> ]	Calculated
$J_{yy}$	0.0086 [kgm <sup>2</sup> ]	Calculated
$J_{zz}$	0.0172 [kgm <sup>2</sup> ]	Calculated
$b$	3.13e-5	Assumed
$d$	7.5e-7	Assumed
$J_r$	6e-5 [kgm <sup>2</sup> ]	Assumed

### 3. DESIGN OF THE CONTROL LAW

The main objective is to design the classic control law in order to stabilize the yaw, pitch and roll angles and the altitude of the

Parrot. Stabilization of the platform is achieved by designing four separate PID controllers controlling pitch, yaw roll angles and the altitude position, respectively. Since the input signals of the model are angular velocities of particular rotors, so the obtained values of the control signals in the closed loop system need to be multiplied by the gain matrix  $K$ , represents transformation controller outputs to speed inputs for each rotor. The obtained block diagram with all controllers is shown in Fig. 3.

$$\Omega_i = U_i * K \tag{8}$$

where:  $i$ - $i$ -th rotor of the Parrot ( $i=1, \dots, 4$ )

$$K = \begin{bmatrix} \frac{1}{4b} & \frac{1}{4b} & \frac{1}{4b} & \frac{1}{4b} \\ 0 & -\frac{1}{2bl} & 0 & \frac{1}{2bl} \\ \frac{1}{2bl} & 0 & -\frac{1}{2bl} & 0 \\ -\frac{1}{4d} & \frac{1}{4d} & -\frac{1}{4d} & \frac{1}{4d} \end{bmatrix} = 1e5 \cdot \begin{bmatrix} 0.0799 & 0.0799 & 0.0799 & 0.0799 \\ 0 & -0.9397 & 0 & 0.9397 \\ 0.9397 & 0 & -0.9397 & 0 \\ -3.333 & 3.333 & -3.333 & 3.333 \end{bmatrix}$$

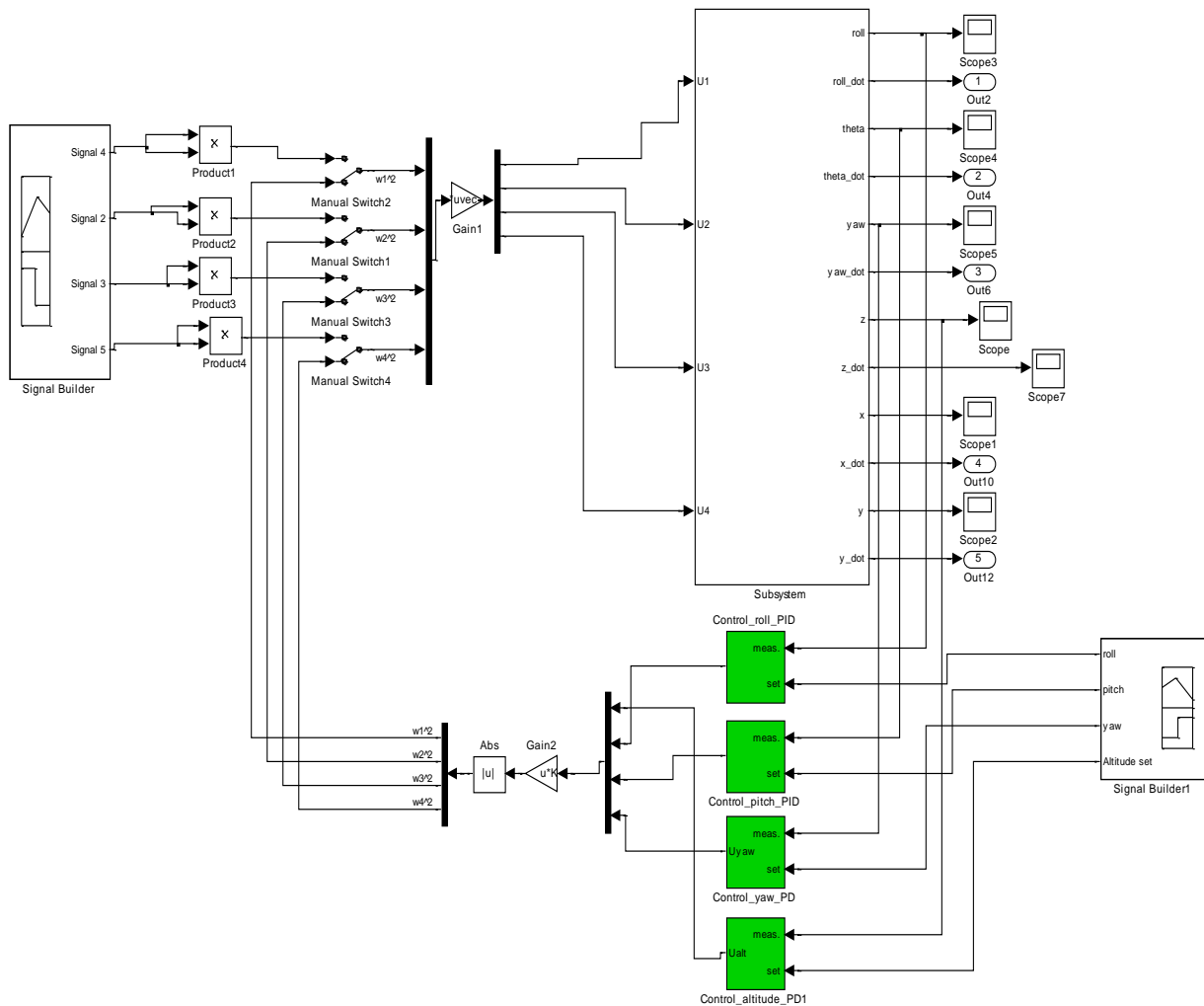


**Fig. 2.** Block diagram of the closed-loop system

In the first step the altitude controller is designed to stabilize the vertical position of the platform. The first input of the controller is the altitude error that is the difference between the altitude value and the measurement value and the second - velocity in Z direction –  $\dot{z}$  as altitude\_d\_error. The control law of this PID controller is as follows (Bouabdalth and North, 2004):

$$\begin{aligned} \dot{e}_z &= \dot{z}; \\ e_z &= z_{SET} - z; \\ u_z &= k_p \cdot e_z + k_i \cdot e_z - k_d \cdot \dot{e}_z \end{aligned}$$

where:  $\dot{z}$  – velocity of the Parrot in Z direction,  $z_{SET}$  – desired altitude of the Parrot in Z direction.

Finally, the transfer function of the controller is:

$$PID(s) = k_d s + k_i / s + k_p \quad (9)$$

During the simulations the changes of pitch, roll and yaw angles are assumed as zero. As a result, the PID controller generated only control signal U1 that caused hovering or falling of the model in vertical direction. Ipso facto all lift forces generated by rotors have the same value. Parameters of such PID controller are chosen by using the trial and error method and equal to:  $k_{p\_alt}=12$ ,  $k_{i\_alt}=1.5$ ,  $k_{d\_alt}=6$ , respectively.

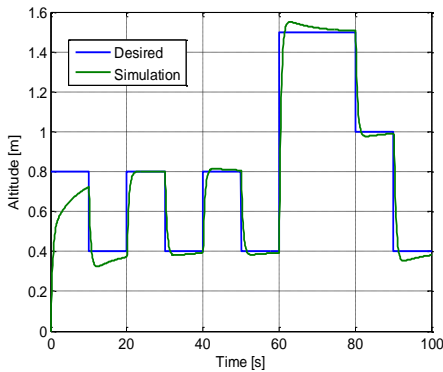


Fig. 3. Altitude response of the closed-loop system

As we can see in Fig.3, the closed loop system is characterized by very short time constant, specially in time range 20-100 s. Taking into account the first 20 seconds of simulation we can see that the system does not achieve desired value of 0.8m. Perhaps it was caused by earlier assumption that the initial conditions of simulation equal to zero.

The next step of the simulation is connected with the design of the pitch controller. Once again, based on two signals: pitch angle and velocity change of pitch angle –  $\theta_{dot}$  the parameters of the controller are chosen as follows:  $k_{p\_teta}=0,2$ ,  $k_{i\_teta}=0$ ,  $k_{d\_teta}=0,15$ , respectively. Finally the transfer function of the controller is:

$$PID\_teta(s) = 0.15s + 0.2 \quad (10)$$

The controller  $PID\_teta(s)$  generates the control signal U3 directly influencing the angular velocity of both front and rear rotors and indirectly influencing control signals U1 and U4. Therefore, in order to verify the parameters of the pitch controller the desired trajectory of pitch and roll angles and the altitude should be included.

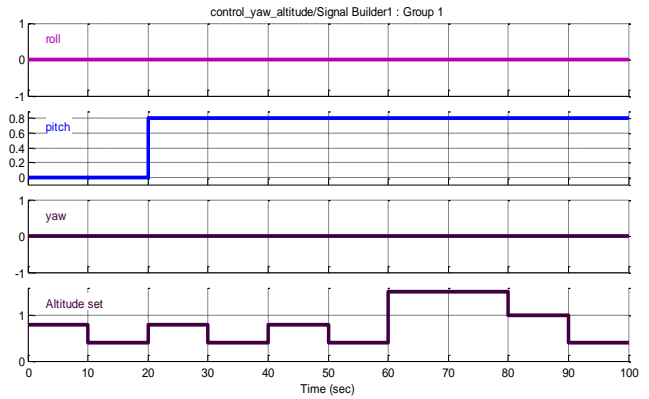


Fig. 4. Desired trajectory of the pitch angle and the altitude

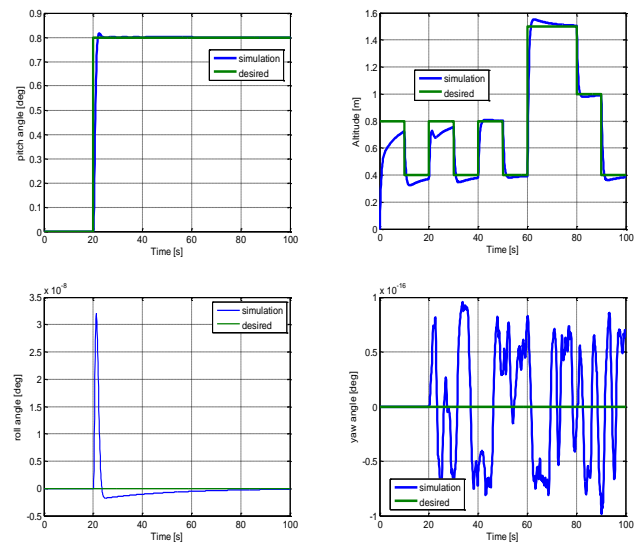


Fig. 5. Response of the closed loop system to the desired trajectory of the pitch angle and the altitude

According to Fig.5 the parameters of the pitch controller are correct. Measurement value of the pitch angle follows the desired trajectory. Moreover both pitch and altitude signals are coupled what is shown on appropriate plots. The small overshoot of the pitch angle at the 22 second of simulation caused small falling of the model. After that both signals once again tried achieve the set value. At this same times others signals: roll and yaw angle still have values of zero. Such behaviour of the closed loop model of course it is a correct.

The next stage of simulation is connected with the design of the yaw controller. In order to choose proper values the parameters of the controller yaw and yaw\_dot signals are taken as inputs. Finally, the parameters of the controller are as follow:  $k_{p\_yaw}=0,1$ ,  $k_{i\_yaw}=0$ ,  $k_{d\_yaw}=0,06$ , respectively, which lead to the transfer function described as:

$$PID\_yaw(s) = 0.06s + 0.1 \quad (11)$$

The yaw controller generated the control signal U4 which influenced only the yaw angle. Thus, change of yaw angle does not caused change of other angles and altitude of the model. Moreover, how we can see in Fig.7 the model with  $PID\_yaw$  controller very fast achieved desired value. So, the closed loop model according with desired impulse very fast in first step rotates in right side and next left side.

#### 4. SUMMARY AND CONCLUSIONS

The paper shows the modelling and control of the quadro-rotor of the Parrot. The first part is connected with derivation of the mathematical model by using Newton-Euler method. The obtained model is a MIMO model, so in the next step the model is simplified and rewritten to the state space form with 12 variables of the state space vector.

Then the model is decoupled and for each signals: roll, pitch and yaw angles and the altitude the PID controllers are designed. The obtained results for all controllers proved that the whole closed loop system correctly stabilizes the motion of the Parrot.

In further investigations, the design of the global control law between two Parrots will be considered. One of them will be a leader and the second will be a follower. Then, the results of such simulations for both Parrots (Leader-Follower) will be implemented to the auto-pilot in order to verify the control algorithms.

#### REFERENCES

1. **Ambroziak L., Gosiewski Z., Ołdziej D.** (2012), *Modeling four rotors Helicopter*, Chapter in monograph: *Elements of autonomous flight of UAV*, Białystok University of Technology (in Polish).
2. **Astrom K.** (2002), *Control System Design*, Chapter PID control, <http://www.cds.caltech.edu/~murray/courses/cds101/fa02/caltech/astrom-ch6.pdf> (20.02.2014).
3. **Bouabdalth S., Noth A.** (2004), *PID vs LQ Control Techniques Applied to Indoor Micro Quadrotor*, IROS.
4. **Clavel R. Siegwert R., Corke P.** (2007), *Design and Control Quadrotors with Application to Autonomous Flying*, Monography with Ecole Polytechnique Federale de Laussane.
5. **De Silva D.** (2012), *Formation Control for Unmanned Aerial Vehicles*, [https://fenix.tecnico.ulisboa.pt/downloadFile/395144217739/Resumo\\_Alargado.pdf](https://fenix.tecnico.ulisboa.pt/downloadFile/395144217739/Resumo_Alargado.pdf) (20.02.2014).
6. **Derafa L., Madani T., Benallegue A.** (2006), *Dynamic Modeling and Experimental Identification of Four Rotors Helicopter Parameters*, *IEEE International Conference on Industrial Technology*, pp.265-272.
7. **Derafa L., Madani T., Ouladi A., Benallegue A.** (2007), *Four Rotors Helicopter Yaw Altitude Stabilization*, *Proceedings of the World Congress on Engineering*, Vol. I, pp.104-110
8. **Kimon P.** (2007), *Advances in Unmanned Aerial Vehicle. State of the Art and Road to Autonomy*, Publisher: Springer
9. **McKerrow P.** (2004), *Modeling the Dragonflyer Four-Rotor Helicopter*, *International Conference on Robotics & Automation*, pp.3596-3601.
10. **Parrot Ar Drone, Developer Guide SDK 1.7.**

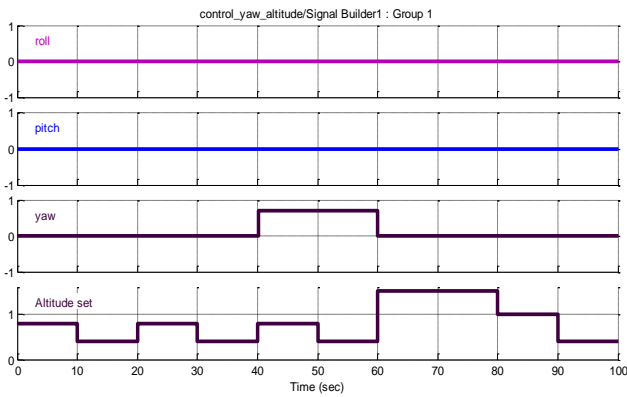


Fig. 6. Desired trajectory of the yaw angle and the altitude

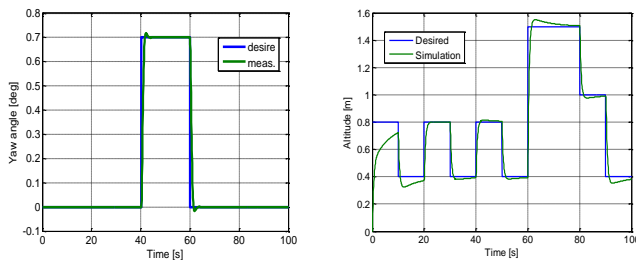


Fig. 7. The closed loop system response with PID\_yaw and PID\_altitude controllers

The last controller is the roll controller. Once again and similar to previous cases, the roll and roll\_dot signals are chosen as input signals. Based on the simulations the parameters of the controller are chosen and equal:  $k_p\_yaw=0.3$ ,  $k_i\_yaw=0.01$ ,  $k_d\_yaw=0.25$ , respectively.

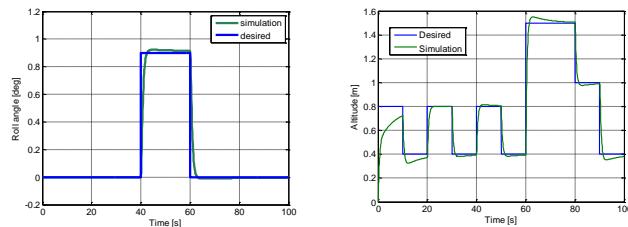


Fig. 8. The closed loop system response with PID\_roll and PID\_altitude controllers

As we can see in Fig.8 also in this case the controller immediately stabilizes the roll angle. Especially, it is shown in the roll angle plot where the rising and falling times are very short. Furthermore, according to Fig.8 the change of the angular velocity of all rotors caused by the change of the control signal U2 does not influence the altitude of the model. Such situation is also correct, because stabilization of the altitude is achieved by the independent altitude controller.

## EFFECT OF THE ATMOSPHERE ON THE PERFORMANCES OF AVIATION TURBINE ENGINES

Włodzimierz BALICKI\*, Paweł GŁOWACKI\*, Stefan SZCZECIŃSKI\*, Ryszard CHACHURSKI\*\*, Jerzy SZCZECIŃSKI\*\*\*

\*Aviation Institute, Propulsion Department, Al. Krakowska 110/114, 02-256 Warszawa, Poland

\*\*Military University of Technology, Faculty of Mechatronics and Aviation, ul. Sylwestra Kaliskiego 2, 00-908 Warszawa, Poland

\*\*\*GE Poland, Al. Krakowska 110/114, 02-256 Warszawa, Poland

[Balicki@ILot.edu.pl](mailto:Balicki@ILot.edu.pl), [Pawel.Glowacki@ILot.edu.pl](mailto:Pawel.Glowacki@ILot.edu.pl), [Ryszard.Chachurski@WAT.edu.pl](mailto:Ryszard.Chachurski@WAT.edu.pl); [Jerzy.Szczecinski@GE.com](mailto:Jerzy.Szczecinski@GE.com)

**Abstract:** The paper presents how the parameters defining the state of the atmosphere: pressure, temperature, humidity, are affecting performance of the aircraft turbine engines and their durability. Also negative impact of dust pollution level is considered as an important source of engine deterioration. Article highlights limitation of the aircraft takeoff weight (TOW) and requirements for length of the runways depending on weather condition changes. These problems stem from the growing "demand" of gas turbine engines for an air. The highest thrust engines have air mass flow more than 1000 kg/s. Engine inlet ice formation is presented as a result of weather conditions and inlet duct design features.

**Key words:** Power Plant, Aircraft Engine, Turbine Engine, Inlet Icing, Standard Atmosphere

### 1. INTRODUCTION

Aviation, like any other form of transport is dependent on the atmosphere conditions (weather). Hence the need to analyze the impact of the environment on the lift force, drag, and a thrust of the aircraft engines. The values of these parameters are proportional to the density of the air.

While in practice, the effect of an altitude on the engine thrust is considered, influence of the temperature and humidity is often overlooked. Higher values of these two parameters are decreasing the lift force and engine thrust. Such conditions are limiting safe takeoff of heavy loaded aircraft (including aerostats). Higher humidity increases the likelihood of inlets icing and can cause engine shutdown during flight.

The phenomenon, which is hard to observe is a gradual loss of thrust due to the erosive effects of dust on the aerodynamic profiles of the blades and vanes, and its deposition in cavities of engine ducts where locally speed is reduced or direction of airflow is changed. The source of dust are mainly contaminated runways, industry, and occasionally volcanic eruptions or dust storms.

Considerations were done for engines performances on take-off ranges. The values of the engine parameters (rotor speed and exhaust gas temperature) are limited by the control system.

### 2. CLIMATE AND THE AIRPORT ALTITUDE INFLUENCE ON THE ENGINE TAKEOFF PERFORMANCES

Assuming that a jet engine has fuel mass flow supplied to the combustor much smaller than the air mass flow, and assuming the full expansion in the exhaust nozzle, thrust of the engine can be described by the relation:

$$K = \dot{m} \cdot (c_5 - V_H) = Q_{pow} \cdot \rho \cdot (c_5 - V_H) \quad (1)$$

where:  $\dot{m}$  – air mass flow,  $c_5$  – exhaust gases velocity,  $V_H$  – air-speed,  $Q_{pow}$  – volumetric airflow,  $\rho$  – air density

Atmospheric air parameters (pressure, temperature and density) are changing with altitude above sea level (ASL), which of course affects the performance of aircraft engines. Lowermost airports are located at altitudes close to sea level, while some of them are in the Andes and the Himalayas at altitudes exceeding 3000 m, and even reaching 4500 m

For engine performances comparison, generally is used model of the International Standard Atmosphere (ISA), in which it is assumed that at sea level ( $H = 0$ ) the air pressure is 101325 Pa, temperature of an air is equal to 288.15 K, and the air density is 1.225 kg/m<sup>3</sup>. This model does not consider humidity changes. Calculation of engine performances assumes that the air is completely "dry". Besides the standard atmosphere, due to the considerable diversity of climatic conditions in the world, additional models of the atmosphere - cold, hot and tropical (Trop) also has been developed, for which the adopted pressure changes are the same as for the standard atmosphere model but different changes in temperature, and hence the change in air density. The described models depending on the airport height above sea-level are shown on Figs. 1, 2 and 3.

The need to take into account temperature changes depending not only on the altitude at which the airport is situated but depends also on latitude. Airports located on similar altitudes for the polar circle have OAT -50°C, while in the airports located in Africa and Asia OAT exceeds +50°C.

In the case of relative humidity we have to consider that in tropical regions often exceeds 90% at the temperatures approx. +30 ... +35°C, while in the same time at the airports located on the same altitude, but in Central Europe conditions may prevail

in where the temperature will correspond to standard conditions and the relative humidity does not exceed 10%.

Calculations carried out for the model of turbofan engine at standard conditions with a thrust approx. 100 kN are showing that when the engine is running and the pressure corresponds to the standard (Fig. 4) it has thrust 12% higher at the temperature less by +35°C than the reference, and 22% lower if the ambient temperature rises by the same amount in relation to the reference temperature.

In case, if that engine will operate from airport situated on altitude close to 4500 m, the thrust will be about 38% less than this can be achieved at the airport, located at sea level.

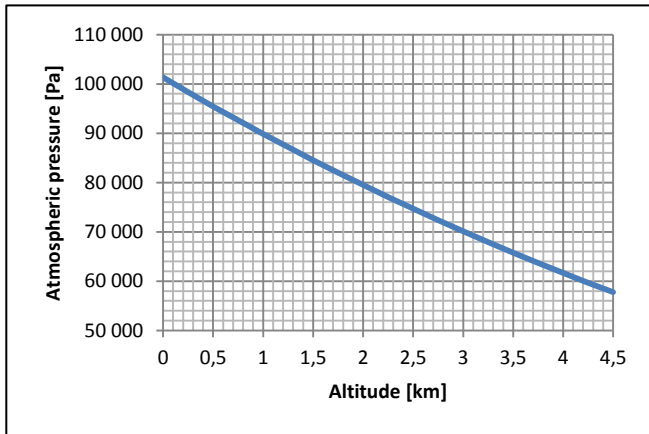


Fig.1. Changes of the atmospheric pressure with the altitude

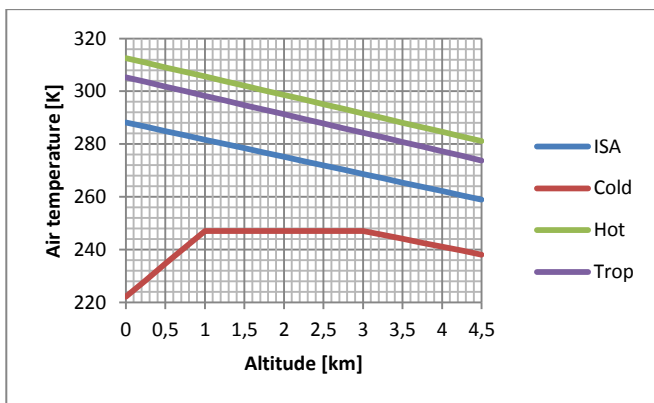


Fig. 2. Changes of the air temperature with the altitude

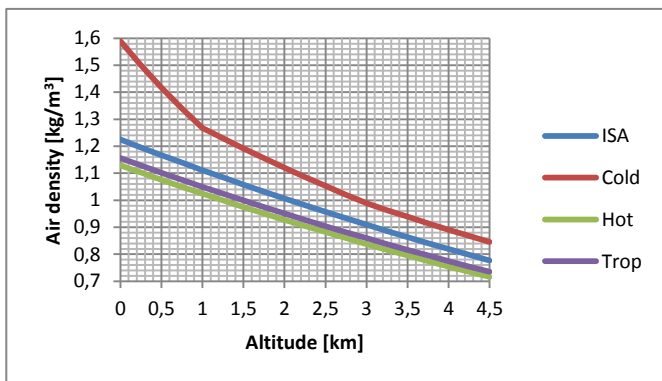


Fig. 3. Changes of the air density with the altitude

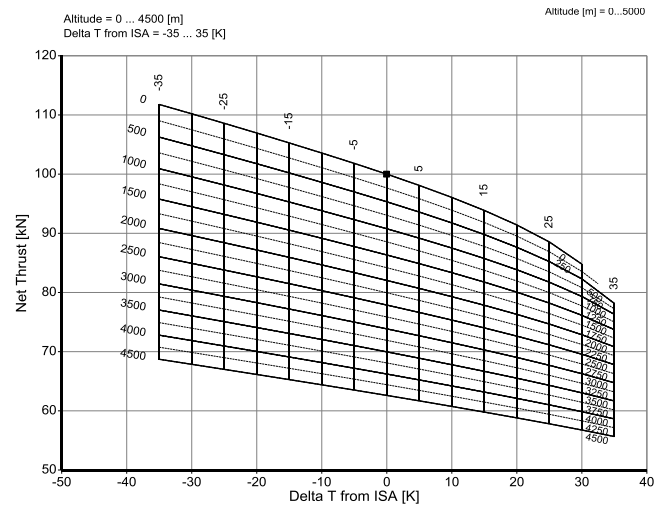


Fig. 4. Changes of the engine thrust with the altitude and the temperatures from -35°C to +35°C (dark dot - the conditions corresponding to ISA, generated by GasTurb 12 program)

### 3. INFLUENCE OF ATMOSPHERIC CONDITIONS ( $T_H$ , $p_H$ ) AND AIRPORT ALTITUDE ON AIRCRAFT PERFORMANCES

Formulas for lift force  $P_z$  and for drag force  $P_x$  of the aircraft are including multiplier – atmospheric air density  $\rho_H$  (2).

$$P_z = \frac{1}{2} \cdot c_z \cdot V_H^2 \cdot S \cdot \rho_H, P_x = \frac{1}{2} \cdot c_x \cdot V_H^2 \cdot S \cdot \rho_H \quad (2)$$

where:  $c_z$  – lift force coefficient,  $c_x$  – drag force coefficient,  $V_H$  – flight speed,  $S$  – wing lifting surface.

This causes that changes of the lift force and the drag force with changes in temperature and altitude of the airport are proportional to changes in the density of the air. Since the lift force coefficient is much greater than the coefficient of drag force the decrease in air density decreases drag force, but much more lift force is reduced. During take-off pilot can increase lift force by flap extension, but this increases the drag force. As a result, the necessary value of the lift force can be achieved by increase of  $V_2$  speed. This causes building of the longer runways, and in addition as already mentioned before, under such conditions the crew has less thrust from the engines. For example, while Chopin Airport runways have length of 2 800 m and 3 620 m runway of Daocheng Airport at an altitude of 4 411 m has a length of 4 200 m and located slightly below Bamda Qamdo Airport has a runway with astonishing length of 5 500 m.

### 4. INFLUENCE OF AIR HUMIDITY ON ENGINE AND AIRCRAFT PERFORMANCES

Changes of the engine thrust as a function of the relative humidity significantly are affected by OAT. In the ISA temperature increase in relative humidity from 0 to 100% causes a slight decrease of thrust (1 .. 2%), but in tropical conditions ISA +30°C in the same humidity changes as above causes decrease of thrust approx. 16% of which 4% solely from the change of relative humidity of the air (Fig. 5).

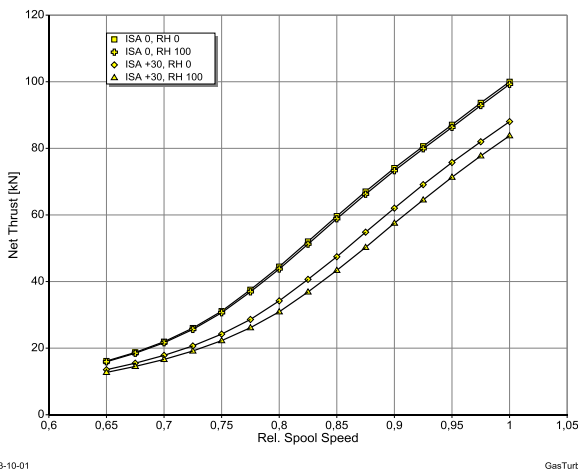


**Fig. 5.** Changes of the engine thrust with the relative speed N2 for a different relative humidity and OAT (generated by GasTurb 12 program)

Steam in the air reduces the mass flow, which leads to a reduction in engine thrust or power. We should also remember that is like anaerobic filling of the air, which in the case of large quantities, e.g. due to evaporation of water along gas path of the compressor or evaporation it in large quantities directly in the combustion chamber, can lead to the flame out, which means uncommanded engine shutdown.

High humidity can also cause icing of the engine, which can occur in temperatures between +10°C ... +15°C and corresponding relative humidity. Icing formations depend on engine design, as well as inlets position on the airframe and their structure. For example, during flight aircraft powered by turbofan engines with high bypass ratio under conditions of super cooled water droplets, may have ice formation on: the inlet leading edge, inlet duct, spinner and on the fan blades as well as on OGV's, low pressure compressor IGV's and first stage blades. Three shaft engines can face in such flight icing conditions on IGV's and IPC's first stage blades.

Ice formation on the inlet duct surface and directly on the compressor inlet, changes the geometry and cross section diameter of the duct and as a consequence reduces airflow and the parameters of airflow before compressor inlet (Chachurski, 2009). These negative changes are decreasing compressor pressure ratio which leads to engine thrust or power reduction, often to compressor instability and as a result high vibration or even engine shutdown. Instability of the compressor is also caused by distortion of duct ribs, vanes and blades airfoils.

Reduced airflow, distortion of the velocity, pressure and temperature circumferential distribution as well as inlet and IGV's airfoils distortion causes also negative circumferential distribution and increase of the temperature before turbine.

Small amount of water injection before compressor inlet increases engine thrust by improving efficiency of its thermodynamic cycle and the growth of mass flow (Water injected before the compressor gradually evaporates, absorbs heat from the air reducing the temperature, increasing its density, which at a constant volumetric flow increases the air mass flow ( $\dot{m} = \rho \cdot Q$ ) due to increase in air density and in addition weight of the injected water. In contrast, steam is only anaerobic filler decreasing amount of the air entering the engine.). Opposite, water in form of liquid or as snow, ice or slush, which gets to the inlet and then passes through the duct leading to serious disruption of engine

performances (Recommended Practices for the Assessment of the Effect of Atmosphere Water Ingestion on the Performance and Operability of Gas Turbine Engines, 1995). In subsequent stages of the compressor the air temperature rises due to the pressure increase. Water sucked into the compressor duct is gradually evaporating. Normally water in liquid form is rejected due to the centrifugal force by the rotor blades on the surface of compressor duct and then flows towards the combustion chamber. This water can get into the bleed valves. If all of the water does not evaporate in the compressor or will not be removed by bleed valves can enter the combustor and may lead to the engine shutdown. Large amount of water vapor worsen preparation and combustion of the air-fuel mixture and moreover, water can rapidly (quasi detonation) vaporize becoming anaerobic filler of the air stream in the combustion chamber causing flame out.

If there is airframe icing, then decreases the lift force, drag force increases, and further increases the weight of the aircraft. For example, if the lifting surfaces of the A380-800 have an ice layer with a thickness of 1 mm, than the aircraft weight would be increased by about 780 kg.

Different anti icing systems are used depends on aircraft type to protect the engine and an airframe. It should be remembered that when anti ice system works causes a decrease in engine thrust, especially when system is heated by the air from the compressor.

## 5. INFLUENCE OF OTHER EXPLOITATION CONDITIONS ON ENGINE PERFORMANCES

Engines are important for flight safety but hail, sand, dust and salt flowing with the air through engine ducts are forming deposits on flow pass surfaces and airfoils or even causing mechanical damages to the engine. Engine performances are deteriorating hence aircraft characteristics are different than calculated.

Engines are damaged most often during taxiing, take-off and landing by objects ejected from the ground by landing gear or thrust reverser. Also inlet-vortex (or ground-vortex) phenomenon causes FOD. In order to prevent engine against FOD a number of organizational and design measures are taken by the industry. Firstly, risk awareness training for ground staff. Secondly, development of a suitable methodologies for takeoff and landing. Design features include installation of particle separators on helicopter inlets or special shapes of the engines inlet ducts. Suction of dust, even particles with a small diameter is leading to wear of engine parts and as a consequence efficiency reduction, which in the turn induces an increase of EGT (Exhaust Gas Temperature) because of higher fuel consumption in order to keep required performance level of the engine.

Takeoff EGT depends on the OAT (Outside Air Temperature) and control system settings. EGT increases with increasing of OAT (Fig. 6a) while the maximum engine thrust is constant. When OAT exceeds certain value EGT is limited by the engine control system, which means further increase of the ambient temperature decreases available engine thrust (Fig. 6b). The maximum temperature value (corner point) below which engine thrust is not decreasing varies between 30°C...35 °C.

For each type of the engine manufacturer specifies the maximum permissible limit of the EGT. For example, for CFM56-3 engines the exhaust gas temperature limit is 1230 K.

EGT during takeoff (but also during lower ranges of engine operation) increases with the engine deterioration. Lower efficiency of the engine main modules (in particular compressor), requires more fuel delivered to the combustor in order to keep the same rotor speed (same engine thrust) to compensate lower compressor pressure ratio.

Higher EGT may indicate erosive wear of the compressor or turbine blades, increased tip clearances or distortion of airfoils by dirty deposit of oil and dust mixture (Dunn et al., 1987; Tabakoff and Hamed, 1984). At the beginning of engine operation after installation on the aircraft EGT is growing rapidly (about 12°C .. 15°C during the first 1000 cycles) compared to the test – cell and then stabilizes at 8°C .. 10°C per 1000 cycles (Fig. 6c). The large EGT increase in the initial period of engine operation in relation to the values measured in the test – cell is due to the fact that there are ideal conditions during manufacturer engine tests.

As a result of engine deterioration, EGT margin becomes smaller (Fig. 6d).

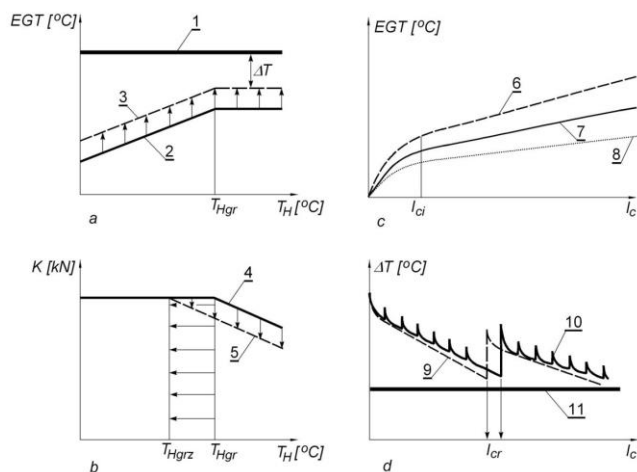


**Fig. 6.** OAT influence on EGT (a) and the thrust K (b); EGT (c) and EGT margin  $\Delta T$  (d) changes depending on the number of cycles: 1 – EGT limit, 2 – New engine takeoff EGT, 3 – Takeoff EGT of the deteriorated engine, 4 – available thrust of a new engine, 5 – available thrust of a deteriorated engine, 6 – EGT of the “dirty” engine, 7 – mean EGT, 8 – EGT of the “clean” engine, 9 –  $\Delta T$  not washed engine, 10 –  $\Delta T$  of the washed engine, 11 –  $\Delta T$  limit,  $T_{HGR}$  – OAT limit for a new engine,  $T_{Hgrz}$  – OAT limit for deteriorated engine,  $l_c$  – the number of engine cycles,  $l_{cl}$  – the number of engine cycles when  $\Delta T$  is decreasing per 1000 cycles,  $l_{cr}$  – the number of engine cycles for repair.

In order to improve the efficiency of the engine by removing dirty deposit accumulated on the blades and vanes operators are performing washing and cleaning of the engine at regular intervals recommended by the engine manufacturer, but operators have the right to adjust these intervals to suit their needs resulting from the specific engine operating conditions (dust, humidity, hot or cold temperatures, short or long flight routes, etc.). These processes are also used in case of an excessive reduction of  $\Delta T$ , and after FOD or bird strikes, etc.

## 6. FINAL COMMENTS

Any unexpected to pilot thrust decrease during takeoff has adverse impact on safety. In extreme cases - the accumulation of factors that reduce thrust: heat, high humidity and low pressure – even threatened disaster. Under the influence of extremely adverse weather conditions the engine may shutdown automatically as a result of the compressor instability. Engine thrust can be unexpectedly reduced (or even the engine can shutdown) by the automatic control system to protect power plant from being damaged due to excessive increase in exhaust gas temperature.

With this in mind the technical staff and flight crew should possess the ability to predict the impact of current or forecasted weather conditions on the aircraft and helicopters and their power plant performances.

## REFERENCES

1. Balicki W., Chachurski R., Głowacki P., Godzimirski J., Kawalec K., Kozakiewicz A., Pałowski Z., Rowiński A., Szczeciński J., Szczeciński S. (2010), *Aviation Turbine Engines. Design – Exploitation – Diagnostic. Part I*, Scientific Publications of the Institute of Aviation, Warsaw (in Polish).
2. Balicki W., Chachurski R., Głowacki P., Godzimirski J., Kawalec K., Kozakiewicz A., Pałowski Z., Rowiński A., Szczeciński J., Szczeciński S. (2012), *Aviation Turbine Engines. Design – Exploitation – Diagnostic. Part II*, Scientific Publications of the Institute of Aviation, Warsaw (in Polish).
3. Balicki W., Chachurski R., Głowacki P., Kozakiewicz A., Kawalec K., Pałowski Z., Szczeciński S. (2009), Inlets – Threat from the inlet vortex and methods of avoid it, *Transactions of the Institute of Aviation*, nr 4/2009 (199), 17-24, (in Polish).
4. Chachurski R. (2009), Inlet icing of turbine engines, *Transactions of the Institute of Aviation*, no 4/2009 (199), 31-49, (in Polish).
5. Dunn M. G., Padova C., Moller J. E., Adams R. M. (1987), Performance Deterioration of a Turbofan and Turbojet Engine Upon Exposure to a Dust Environment, *Journal of Engineering of Gas Turbine and Power*, Vol. 109/341, 336-343.
6. **Global Climatic Data for Developing Military Products** (1997), Department of Defense, USA.
7. **Recommended Practices for the Assessment of the Effect of Atmosphere Water Ingestion on the Performance and Operability of Gas Turbine Engines** (1995) AGARD-AR-332, NATO Science and Technology Organization, (modif. 14 Feb. 2014)
8. Tabakoff W., Hamed A. (1984), *Installed Engine Performance in Dust-Laden Atmosphere*, AIAA Aircraft Design Systems and Operations Meeting, San Diego, California,
9. Taylor C.F. (1992), *The Internal Combustion Engine in Theory and Practice*, The MIT Press, Vol. 1, Second Edition,
10. **The Effect of Humidity on Engine Power at Altitude**, Report no 426, NACA Central, Cranfield, U.K.

## MEASUREMENT UNCERTAINTY ANALYSIS OF THE STRAIN GAUGE BASED STABILOGRAPHIC PLATFORM

Wojciech WALENDZIUK\*

\*Białystok University of Technology, Faculty of Electrical Engineering, ul. Wiejska 45 D, 15-351 Białystok, Poland

[w.walendziuk@pb.edu.pl](mailto:w.walendziuk@pb.edu.pl)

**Abstract:** The present article describes constructing a stabilographic platform which records a standing patient's deflection from their point of balance. The constructed device is composed of a toughened glass slab propped with 4 force sensors. Power transducers are connected to the measurement system based on a 24-bit ADC transducer which acquires slight body movements of a patient. The data is then transferred to the computer in real time and data analysis is conducted. The article explains the principle of operation as well as the algorithm of measurement uncertainty for the COP (Centre of Pressure) surface  $(x, y)$ .

**Key words:** Posturograph, Stabilography Center of Pressure, Measurement Uncertainty

### 1. INTRODUCTION

Posturography is an element of medical diagnostics and it has been used since 1970s. This type of examination supports a physician in diagnosing patient's balance system and enables distinction some factors which influence keeping balance. A basic balance test requires conducting a series of experiments during which a patient tries to keep his/her balance in a loose position with their eyes closed and opened. This type of examination is called Romberg's test (Cornilleau-Pérès et al., 2005; Soochan et al., 2012; Nashner, 1993). A patient standing on the platform tries to keep balance but, because of the balance system damage, he/she may sway in different directions or towards the damaged bony labyrinth. In this type of examination, using special platforms connected to computers becomes common. Data concerning the patient's posture stability is recorded in real time and then calculated as, e.g.: coordination coefficient, trajectory length, speed or deflection radius. Visualization of measurement results with the use of an appropriate program is the following stage of the procedure (Thurner et al., 2000; Dichgans et al., 1976). Interactive techniques are another form of conducting examination or rehabilitation. During such procedure, a patient reacts to certain information presented on a screen with his/her body stability. Such action enables establishing the time of response to a graphic or sound signal (Winter, 1990; Gage et al., 2004; Derlatka, 2012).

It is worth stressing that using computer measurement systems enabled graphic presentation of experiments results in the form of statokinesiogram. The image presented on the screen shows the movement trajectory of Centre of Pressure in the Cartesian system of coordinates. In the commonly used type of classification, the deflection from the  $X$  axis is directed right and left, and the deflection along the  $Y$  axis – forward and backward. Stabilography, which shows COP  $(x, y)$  coefficients in time, is another form of graphic presentation of measurement results (Baratto et al., 2004; Idzkowski, Walendziuk, 2009; Michalak, Jaskowski, 2002). The present article contains a description

of a prototype device which performs those tasks. Additionally, the author conducted the analysis of metrological properties of the device using the measurement uncertainty technique (Joint Committee of Guides in Metrology, 2008). The use of this procedure enabled the assessment of the location accuracy of COP which is described by the  $[x(i), y(i)]$  coefficients recorded during the platform being tested.

### 2. STABILOGRAPHIC PLATFORM

Stabilization of the vertical body position is done by minimizing its swaying in such a way that the vertical section of the body mass shifted beyond anatomical boundaries of the base of support located within the feet adhesion to the ground. Keeping stable vertical body position requires analysis of stimuli from sensor systems. Computerized dynamic posturography (CDP) is a test which helps record and assess postural reactions. This work presents a stabilographic platform which is based on 4 strain gauge sensors connected with a measurement data acquisition system.

#### 2.1. Data Acquisition Device

The measurement system is composed of 3 functional modules. One of them is a measurement block based on strain gauge sensors and an analog-digital transducer (Fig.1). The measurement system is based on Wheatstone's bridges which contain strain gauge transducers measuring sensors deflection. The measurement signal is initially processed by operational amplifiers (MCP6N11) as coordinating systems, and low-pass filters. Then, specific voltages are sent to a 24-bit analogue-digital converter  $\Sigma\Delta$  which communicates with another functional module with the use of Serial Peripheral Interface (SPI) acquiring data.

The data acquisition module on the prototype board equipped with an ARM type processor of the following parameters: 48 MHz

of maximum clock frequency, 128 KB Flash memory, 16 KB SRAM memory. The use of this system enables extending the device with an additional function, which is immediate visualization of measurement results.

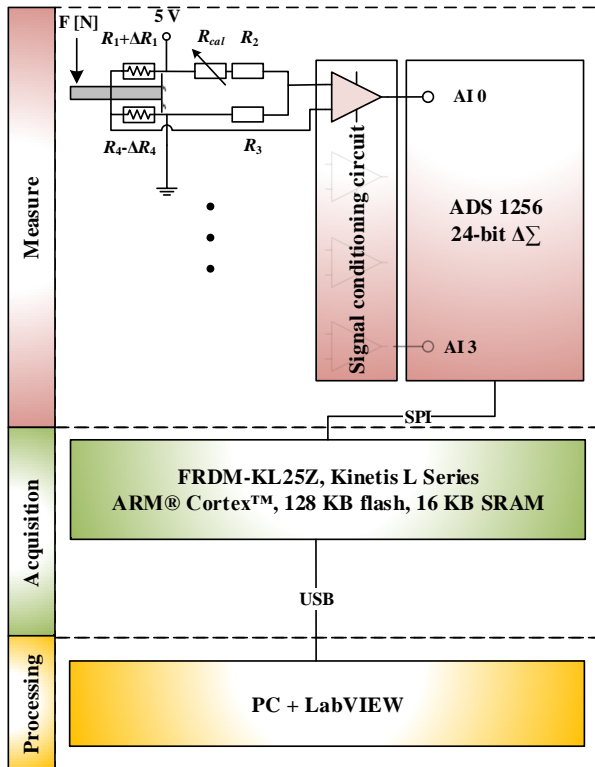


Fig. 1. Functional blocks of the measurement system

Because of the fact that the project in the beginning stage, it has been decided that measurement data is sent to the final functional block represented by a PC equipped with LabVIEW data acquisition and processing system. LabVIEW was used to create an application to visualize the trajectory of patient's centre of pressure (Fig. 2).

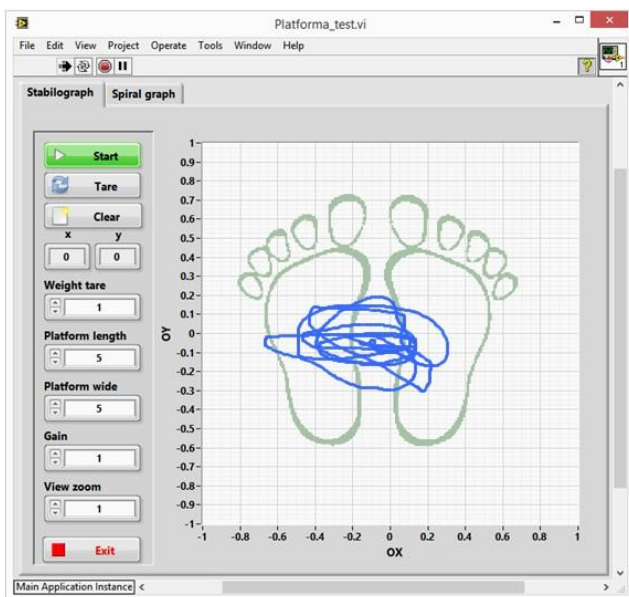


Fig. 2. Front panel view of the virtual instrument created in the LabVIEW system with registered trajectory

It is worth stressing that the device has been configured in a way which enables sending data through a USB interface or wirelessly with the use of devices operating in ZigBee standard.

## 2.2. Platform Construction

Rectangular platform made of safety tempered glass is the basic element of the device. The platform is embedded on 4 weight sensors placed in the corners of the slab. Each sensor is equipped with 2 resistance strain gauges of  $120\Omega$  and  $k = 2.15$  (Fig. 3). Considering forces denotations and the system of coordinates, equations of the centre of pressure point can be formed. The equations contain coefficients describing the force of pressure of individual sensors.

$$x = \frac{L_x}{2} \left[ 1 + \left( 1 + \frac{W_t}{\sum_{x=1}^4 F_x} \right) \cdot \frac{F_3 - F_4 + F_4 - F_1}{\sum_{x=1}^4 F_x} \right] - \frac{L_x}{2} \quad (1)$$

$$y = \frac{L_y}{2} \left[ 1 + \left( 1 + \frac{W_t}{\sum_{x=1}^4 F_x} \right) \cdot \frac{F_3 - F_2 + F_4 + F_1}{\sum_{x=1}^4 F_x} \right] - \frac{L_y}{2} \quad (2)$$

where:  $W_t$  – tare of the platform considering the weight of the platform,  $F_1, F_2, F_3, F_4$  – forces influencing particular strain gauge sensors,  $L_x, L_y$  – platform dimensions.

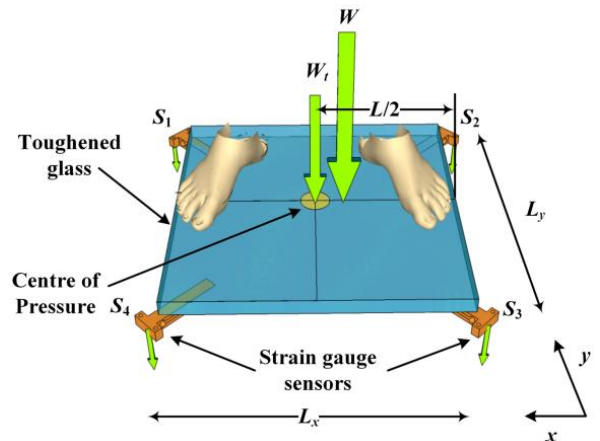


Fig. 3. General view of the platform with forces, sensors  $S_1, S_2, S_3, S_4$  and coordinates assignment

Transducers in the system of the Wheatstone's bridge (Fig. 4) are connected in such a way that one of them is stretched and the other one – compressed. Thanks to this solution it is possible to obtain double amplification of the signal on the diagonal of the bridge.

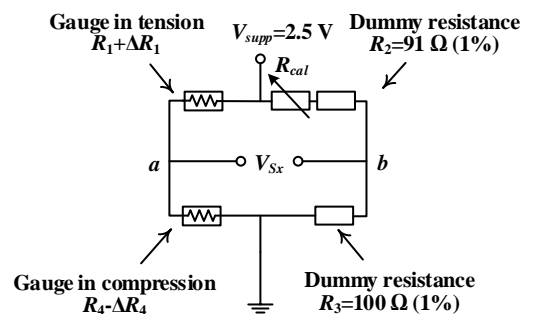


Fig. 4. Wheatstone's bridge circuit applied in the measurement sensor

The equation describing the voltage  $V_{Sx}$  on the diagonal of the bridge can be formed with the use of the method of dividing the bridge system into voltage divisors and calculating the potential difference between the nodes ( $a$  and  $b$ ). The following equation is formed:

$$V_{ab} = V_{Sx} = V_{supp} \cdot \left( \frac{R_1}{R_1 + R_4} - \frac{R_2 + R_{cal}}{R_2 + R_{cal} + R_3} \right) \quad (3)$$

A calibrating resistor was placed in the branch with a resistor of constant value of  $R_2$ . The resistor  $R_{cal}$  can have two aims. One of them is to equilibrate the bridge, which means – to help establish the value of the voltage  $V_{Sx}$  on the 0 level. The other task is enabling to implement offset voltage  $V_{offset}$  in the system of the bridge. This solution enables a one-way system (pressure) to operate also two-way. Thanks to this, it is also possible to measure deflections in the opposite direction than the pressure direction, but with smaller resolution of the analog to digital converter (Fig. 5).

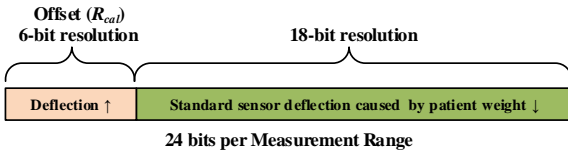


Fig. 5. Effective resolution range of analog to digital converter when calibration resistor is applied

However, the necessity of using a resistor of high precision, which is unfortunately difficult to do, is a disadvantage of the solution. In the presented measurement system a  $20\Omega$  multitransistor resistor of 10% tolerance was used. Eventually, initial calibration of the measurement system was done by  $R_{cal}$  resistor. The obtained  $V_{Sx}$  voltage was close to 0 level. The final version of the measurement equation takes the following form:

$$V_{Sx} = V_{supp} \cdot \left( \frac{R_1 + \Delta R_1}{R_1 + \Delta R_1 + R_4 - \Delta R_4} - \frac{R_2 + R_{cal}}{R_2 + R_{cal} + R_3} \right) \quad (4)$$

Additionally, assuming that strain gauges have similar parameters and that they are placed centrally towards the measurement beam, it can be stated that their increments are equal  $\Delta R_1 = \Delta R_4 = \Delta R$ . the measurement equation can be then simplified to the following form:

$$V_{Sx} = V_{supp} \cdot \left( \frac{R_1 + \Delta R}{R_1 + R_4} - \frac{R_2 + R_{cal}}{R_2 + R_{cal} + R_3} \right) \quad (5)$$

As the platform is equipped with 4 beams ( $S_1, S_2, S_3, S_4$ ), the above equation (5) can be applied to 4 voltages ( $V_{S1}, V_{S2}, V_{S3}, V_{S4}$ ) measured in systems based on Wheatstone's bridges. Measuring individual components enables establishing the centre of pressure of the platform COP according to equations (6) and (7):

$$x = \frac{L_x}{2} \cdot \left[ 1 + \left( 1 + \frac{V_{Wt}}{V_{S1} + V_{S2} + V_{S3} + V_{S4} - V_{Wt}} \cdot \frac{V_{S3} - V_{S4} + V_{S2} - V_{S1}}{V_{S1} + V_{S2} + V_{S3} + V_{S4}} \right) - \frac{L_x}{2} \right] \quad (6)$$

$$y = \frac{L_y}{2} \cdot \left[ 1 + \left( 1 + \frac{V_{Wt}}{V_{S1} + V_{S2} + V_{S3} + V_{S4} - V_{Wt}} \cdot \frac{V_{S3} - V_{S2} + V_{S4} - V_{S1}}{V_{S1} + V_{S2} + V_{S3} + V_{S4}} \right) - \frac{L_y}{2} \right] \quad (7)$$

where:  $V_{Wt}$  – tare of the device and offset voltages of the Wheatstone's bridge system,  $V_{S1}, V_{S2}, V_{S3}, V_{S4}$  – values of voltage from the measurement sensors.

### 3. ANALYSIS OF THE UNCERTAINTY OF MAXIMAL MEASUREMENT RESULTS

The analysis of measurement uncertainty is based on calculating the maximum measurement error of the centre of pressure coefficients. This uncertainty depends on various factors, e.g. the supply voltage of the bridge system, resistance tolerance values, the accuracy of the analog to digital converter. Firstly, the coefficient of the influence of a given standard uncertainty on the total complex standard uncertainty must be evaluated. The law of uncertainty propagation must be applied in order to do it. On this basis, in order to calculate the value of measurement uncertainty, it is necessary to use the differential calculus in relation to the function of the equation describing indirect measurement. In this case partial differential equations for the function of processing the Wheatstone's bridge system should be formed, and then – partial differential equations for the functions of calculating  $x$  and  $y$  coordinates.

#### 3.1. Uncertainty of Strain Gauge Measurement

In the applied ADS1256 analog to digital converter, the manufacturer guarantees the 24-bits no missing codes measurement resolution for all data rates and internal programmable gain amplifier settings. Nevertheless, error factors such as nonlinearity  $\pm 0.0010\%$  or noise, which causes obtaining effective 23-bits noise-free resolution, should be taken into consideration. As the reference voltage equals 2.56 V, maximum error of measurement conducted by a transducer will not exceed 25.60  $\mu V$ .

Tab. 1 Maximum permissible errors values of the elements of the measurement system

Error source	Error measure	Maximum permissible error value	Distribution type	Standard uncertainty of B type
Error of voltage measurement conducted by ADC	$V_{supp} = 2.5 \text{ V}$ $\pm 0.001\%$	25.00 $\mu V$	rectangular	$\frac{25.00 \mu V}{\sqrt{3}}$ $= 14.43 \mu V$
$R_2$ resistance tolerance	$R_2 = 91 \Omega$ $\pm 1\%$	0.91 $\Omega$	rectangular	$\frac{0.91 \Omega}{\sqrt{3}}$ $= 0.53 \Omega$
$R_3$ resistance tolerance	$R_3 = 100 \Omega$ $\pm 1\%$	1.00 $\Omega$	rectangular	$\frac{1.00 \Omega}{\sqrt{3}}$ $= 0.58 \Omega$
$R_{cal}$ resistor tolerance for maximum value of resistance	$R_{cal}(\text{max}) = 20 \Omega$ $\pm 10\%$	2.00 $\Omega$	rectangular	$\frac{2.00 \Omega}{\sqrt{3}}$ $= 1.15 \Omega$
Maximal error of $R_1$ strain gauges	determined during experiment	5.66 m $\Omega$	normal	5.66 m $\Omega$
Maximal error of $R_4$ strain gauges	determined during experiment	4.57 m $\Omega$	normal	4.57 m $\Omega$

Maximum permissible error values of transducers and the other resistances in the system are additional factors. Maximal error of force transducers were established in a measurement experiment. Maximal errors were measured for 4 applied transducers placed on the surface of the beam and underneath it. Their biggest values were selected for the purpose of calculations. Other maximum permissible errors and the values of standard uncertainty are presented in Tab. 1.

Equation (8), concerning standard uncertainty, was formed on the basis of the expression describing voltage on diagonals of the bridge. After determining partial derivatives towards particular variables, equations (9 – 14) were obtained.

$$u^2(V_{Sx}) = \left(\frac{\partial V_{Sx}}{\partial V_{supp}}\right)^2 \cdot u^2(V_{supp}) + \left(\frac{\partial V_{Sx}}{\partial R_1}\right)^2 \cdot u^2(R_1) + \left(\frac{\partial V_{Sx}}{\partial R_2}\right)^2 \cdot u^2(R_2) + \left(\frac{\partial V_{Sx}}{\partial R_3}\right)^2 \cdot u^2(R_3) + \left(\frac{\partial V_{Sx}}{\partial R_4}\right)^2 \cdot u^2(R_4) + \left(\frac{\partial V_{Sx}}{\partial R_{cal}}\right)^2 \cdot u^2(R_{cal}) \quad (8)$$

$$\left(\frac{\partial V_{Sx}}{\partial V_{supp}}\right)^2 = \left(-\frac{(R_2 + R_{cal}) \cdot R_4 - R_1 \cdot R_3}{(R_2 + R_3 + R_{cal}) \cdot (R_4 + R_1)}\right)^2 = 40.086 \cdot 10^{-15} \frac{\Omega^2}{\Omega^2} \quad (9)$$

$$\left(\frac{\partial V_{Sx}}{\partial R_1}\right)^2 = \left(-\frac{V_{supp} \cdot R_4}{(R_4 + R_1)^2}\right)^2 = 8.257 \cdot 10^{-10} \frac{V^2}{\Omega^2} \quad (10)$$

$$\left(\frac{\partial V_{Sx}}{\partial R_2}\right)^2 = \left(-\frac{V_{supp} \cdot R_3}{(R_3 + R_2 + R_{cal})^2}\right)^2 = 0.526 \cdot 10^{-5} \frac{V^2}{\Omega^2} \quad (11)$$

$$\left(\frac{\partial V_{Sx}}{\partial R_3}\right)^2 = \left(-\frac{V_{supp} \cdot (R_2 + R_{cal})}{(R_3 + R_2 + R_{cal})^2}\right)^2 = 1.241 \cdot 10^{-5} \frac{V^2}{\Omega^2} \quad (12)$$

$$\left(\frac{\partial V_{Sx}}{\partial R_4}\right)^2 = \left(-\frac{V_{supp} \cdot R_1}{(R_4 + R_1)^2}\right)^2 = 9.468 \cdot 10^{-10} \frac{V^2}{\Omega^2} \quad (13)$$

$$\left(\frac{\partial V_{Sx}}{\partial R_{cal}}\right)^2 = \left(-\frac{V_{supp} \cdot R_3}{(R_3 + R_2 + R_{cal})^2}\right)^2 = 4.439 \cdot 10^{-5} \frac{V^2}{\Omega^2} \quad (14)$$

Eventually, after substituting the data, standard uncertainty of voltage measurement of the following value was obtained:

$$u(V_{Sx}) = 7.878 \cdot 10^{-3} \text{ V} \quad (15)$$

### 3.2. Uncertainty of Coordinates Calculation

In order to determine standard uncertainty of the centre of pressure  $x$  coordinate, partial differential equations for equation (6) were formed.

$$u^2(x) = \left(\frac{\partial x}{\partial L_x}\right)^2 \cdot u^2(L_x) + \left(\frac{\partial x}{\partial V_{Wt}}\right)^2 \cdot u^2(V_{Wt}) + \left(\frac{\partial x}{\partial V_{S1}}\right)^2 \cdot u^2(V_{S1}) + \left(\frac{\partial x}{\partial V_{S2}}\right)^2 \cdot u^2(V_{S2}) + \left(\frac{\partial x}{\partial V_{S3}}\right)^2 \cdot u^2(V_{S3}) + \left(\frac{\partial x}{\partial V_{S4}}\right)^2 \cdot u^2(V_{S4}) \quad (16)$$

The following data were taken in order to conduct the computations: the width of the platform -  $L_x = 0.251$  m, determined with the use of a Leica DISTO D3a distance meter of the accuracy which equaled  $\pm 1$  mm, the value of numerical tarring (in the program algorithm) the platform with no load  $W_t = 0.000$  V, uncertainty values of voltage measurement in Wheatstone's bridge ( $V_{S1}, V_{S2}, V_{S3}, V_{S4}$ ) =  $7.878 \cdot 10^{-3}$  V. Final values of partial differential equations (17 – 22):

$$\left(\frac{\partial x}{\partial L_x}\right)^2 = \left(\frac{V_{S4} - V_{S3} - V_{S2} + V_{S1}}{2 \cdot (V_{Wt} - V_{S1} - V_{S2} - V_{S3} - V_{S4})}\right)^2 = 0.000 \frac{V^2}{V^2} \quad (17)$$

$$\left(\frac{\partial x}{\partial V_{Wt}}\right)^2 = \left(\frac{-L_x \cdot (V_{S4} - V_{S3} - V_{S2} + V_{S1})}{2 \cdot (V_{Wt} - V_{S1} - V_{S2} - V_{S3} - V_{S4})^2}\right)^2 = 0.000 \frac{m^2}{V^2} \quad (18)$$

$$\left(\frac{\partial x}{\partial V_{S1}}\right)^2 = \left(\frac{L_x \cdot (V_{Wt} - 2 \cdot V_{S2} - 2 \cdot V_{S3})}{2 \cdot (V_{Wt} - V_{S1} - V_{S2} - V_{S3} - V_{S4})^2}\right)^2 = 15.861 \frac{m^2}{V^2} \quad (19)$$

$$\left(\frac{\partial x}{\partial V_{S2}}\right)^2 = \left(\frac{-L_x \cdot (V_{Wt} - 2 \cdot V_{S1} - 2 \cdot V_{S4})}{2 \cdot (V_{Wt} - V_{S1} - V_{S2} - V_{S3} - V_{S4})^2}\right)^2 = 15.861 \frac{m^2}{V^2} \quad (20)$$

$$\left(\frac{\partial x}{\partial V_{S3}}\right)^2 = \left(\frac{-L_x \cdot (V_{Wt} - 2 \cdot V_{S1} - 2 \cdot V_{S4})}{2 \cdot (V_{Wt} - V_{S1} - V_{S2} - V_{S3} - V_{S4})^2}\right)^2 = 15.861 \frac{m^2}{V^2} \quad (21)$$

$$\left(\frac{\partial x}{\partial V_{S4}}\right)^2 = \left(\frac{L_x \cdot (V_{Wt} - 2 \cdot V_{S2} - 2 \cdot V_{S3})}{2 \cdot (V_{Wt} - V_{S1} - V_{S2} - V_{S3} - V_{S4})^2}\right)^2 = 15.861 \frac{m^2}{V^2} \quad (22)$$

On the basis of solution equation (16), uncertainty value of the  $x$  coordinate was obtained:

$$u^2(x) = 0.0627 \text{ m} \quad (23)$$

Calculating the uncertainty of the standard  $y$  coordinate is the following stage of the process. With the use of the differential calculus for equation (7), equation (24) was obtained:

$$u^2(y) = \left(\frac{\partial y}{\partial L_y}\right)^2 \cdot u^2(L_y) + \left(\frac{\partial y}{\partial V_{Wt}}\right)^2 \cdot u^2(V_{Wt}) + \left(\frac{\partial y}{\partial V_{S1}}\right)^2 \cdot u^2(V_{S1}) + \left(\frac{\partial y}{\partial V_{S2}}\right)^2 \cdot u^2(V_{S2}) + \left(\frac{\partial y}{\partial V_{S3}}\right)^2 \cdot u^2(V_{S3}) + \left(\frac{\partial y}{\partial V_{S4}}\right)^2 \cdot u^2(V_{S4}) \quad (24)$$

Next, after substituting data: the length of the platform (measured - as in the previous case - by a laser device for distance measurement)  $L_y = 0.252$  m, the tare value with no load  $V_{Wt} = 0.000$  V, values of voltage measurement uncertainty in Wheatstone's bridges  $(V_{S_1}, V_{S_2}, V_{S_3}, V_{S_4}) = 7.878 \cdot 10^{-3}$  V, in equations (25 - 30), (31) was obtained.

$$\left(\frac{\partial y}{\partial L_y}\right)^2 = \left(\frac{V_{S_1} + V_{S_2} - V_{S_3} - V_{S_4}}{2 \cdot (V_{Wt} - V_{S_1} - V_{S_2} - V_{S_3} - V_{S_4})}\right)^2 = 0.000 \frac{V^2}{V^2} \quad (25)$$

$$\left(\frac{\partial y}{\partial V_{Wt}}\right)^2 = \left(\frac{L_y \cdot (-V_{S_1} - V_{S_2} + V_{S_3} + V_{S_4})}{2 \cdot (V_{Wt} - V_{S_1} - V_{S_2} - V_{S_3} - V_{S_4})^2}\right)^2 = 0.000 \frac{V^2}{V^2} \quad (26)$$

$$\left(\frac{\partial y}{\partial V_{S_1}}\right)^2 = \left(\frac{L_y \cdot (V_{Wt} - 2 \cdot V_{S_3} - 2 \cdot V_{S_4})}{2 \cdot (V_{Wt} - V_{S_1} - V_{S_2} - V_{S_3} - V_{S_4})^2}\right)^2 = 15.988 \frac{m^2}{V^2} \quad (27)$$

$$\left(\frac{\partial y}{\partial V_{S_2}}\right)^2 = \left(\frac{L_y \cdot (V_{Wt} - 2 \cdot V_{S_3} - 2 \cdot V_{S_4})}{2 \cdot (V_{Wt} - V_{S_1} - V_{S_2} - V_{S_3} - V_{S_4})^2}\right)^2 = 15.988 \frac{m^2}{V^2} \quad (28)$$

$$\left(\frac{\partial y}{\partial V_{S_3}}\right)^2 = \left(\frac{-L_y \cdot (V_{Wt} - 2 \cdot V_{S_1} - 2 \cdot V_{S_2})}{2 \cdot (V_{Wt} - V_{S_1} - V_{S_2} - V_{S_3} - V_{S_4})^2}\right)^2 = 15.988 \frac{m^2}{V^2} \quad (29)$$

$$\left(\frac{\partial y}{\partial V_{S_4}}\right)^2 = \left(\frac{-L_y \cdot (V_{Wt} - 2 \cdot V_{S_1} - 2 \cdot V_{S_2})}{2 \cdot (V_{Wt} - V_{S_1} - V_{S_2} - V_{S_3} - V_{S_4})^2}\right)^2 = 15.988 \frac{m^2}{V^2} \quad (30)$$

$$u^2(y) = 0.0630 \text{ m} \quad (31)$$

#### 4. CONCLUSIONS

This work presents the results of the measurement uncertainty computations of a stabilographic platform centre of pressure. Identical maximal errors of strain gauges were assumed in calculations. The errors were determined experimentally, examining each sensor individually. Then, maximum error values (for strain gauges placed on the upper and lower parts of the beam) ob-

tained for  $S_3$  sensor were chosen for computations. It appeared that sensor  $S_3$  was the most precise and it introduced the biggest measurement error into the platform system.

The results of the determined standard uncertainty for  $x$  and  $y$  coordinates are similar and equal about 63 mm, which is a relatively big value. However, this value was determined for maximum error values of particular parts of the measurement system.

Analysis of measurement repetitiveness, as well as examining the centre of pressure alignment of the platform will be the following stage of the research.

#### REFERENCES

1. Baratto M., Cervera Ch., Jacono M. (2004), Analysis of Adequacy of a Force Platform for Stabilometric Clinical Investigations, *Mediterranean Conference on Measurement*, 207-211.
2. Cornilleau-Pérès V., Shabanac N., Droulezd J., Gohe J.C.H., Leef G.S.M., Chew P.T.K. (2005), Measurement of the Visual Contribution to postural steadiness from the COP Movement: Methodology And Reliability, *Gait & Posture*, Vol. 22, 2, 96-106.
3. Derlatka M. (2012), Human Gait Recognition Based on Signals from Two Force Plates, *Lecture Notes in Computer Science*, Vol. 7268: Artificial Intelligence and Soft Computing, Springer-Verlag, 251-258.
4. Dichgans J., Mauritz K.H., Allum J.H.J., Brandt T. (1976), Postural Sway in Normals and Ataxic Patients: Analysis of the Stabilizing and Destabilizing Effects of Vision, *Agressologie*, 17, 15-24.
5. Evaluation of Measurement Data - Guide to the Expression of Uncertainty in Measurement, *JCGM (Joint Committee of Guides in Metrology)* (2008).
6. Gage W.H., Winter D.A., Frank J.S., Adkin A.L. (2004), Kinematic and Kinetic Validity of the Inverted Pendulum Model in Quiet Standing, *Gait Posture* 19, 124-132.
7. Idzkowski A., Walendziuk W., (2009), Evaluation of the Static Posturograph Platform Accuracy, *Journal of Vibroengineering*, Vol. 11, 3, 511-516.
8. Michalak K., Jaskowski P. (2002), Dimensional Complexity of Posturographic Signals: I. Optimization of Frequency Sampling and Recording Time, *Curr Topics in Biophys*, 26(2), 235-244.
9. Nashner L.M. (1993), Computerized Dynamic Posturography in G. P. Jacobsen; C. W. Newman; and J. M. Kartush (eds.), *Handbook of Balance Function Testing*, Mosby-Year Book: Chicago, IL, 309-323.
10. Soochan K., Mijoo K. Nambom K., Sungmin K., Gyuchoel H., (2012), Quantification and Validity of Modified Romberg Tests Using Three-Axis Accelerometers, Green and Smart Technology with Sensor Applications, Communications in Computer and Information Science, Vol. 338, 254-261.
11. Thurner S., Mittermaier C., Hanel R., Ehrenberger K. (2000), Scaling violation phenomena and fractality in the Human Posture Control System, *Physical Review E*, 62(3).
12. Winter D.A. (1990), *Biomechanics and Motor Control of Human Movement*, John Wiley & Sons Inc., Toronto.

The work has been accomplished under the research project No. S/WE/1/2013.

## ANALYSIS OF NON-UNIFORM DISTRIBUTION OF THE EQUIVALENT STRESS BY SELECTED MULTIAXIAL FATIGUE CRITERIA IN BUTT-WELDED JOINT

Przemysław STASIUK\*, Aleksander KAROLCZUK\*, Wiesław KUCZKO\*\*

\*Opole University of Technology, Faculty of Mechanical Engineering,  
Department of Mechanics and Machine Design, ul. Prószkowska 76, 45-758 Opole, Poland

\*\*Poznan University of Technology, Chair of Management and Production Engineering,  
Department of Mechanical Engineering and Management, Pl. M. Skłodowskiej-Curie 5, 60-965 Poznań, Poland

[przemyslaw.stasiuk@wp.pl](mailto:przemyslaw.stasiuk@wp.pl), [a.karolczuk@po.opole.pl](mailto:a.karolczuk@po.opole.pl), [wieslaw.kuczko@doctorate.put.poznan.pl](mailto:wieslaw.kuczko@doctorate.put.poznan.pl)

**Abstract:** Welded joints are areas of increased stresses in construction. The reason for this phenomenon is associated with the nonhomogeneous mechanical, structural and geometrical properties of the weld seams. Generally, in the majority of the calculation it is assumed that the shape of the weld is uniform over the entire length and it is not deviating from the theoretical one. This article shows the distribution of stress in the butt-weld made of S355J2+N steel specimens. The shape of a joint was transferred to the finite element analysis by application of 3D scanning. Selected multiaxial fatigue criteria and probability mass function were used for a description of the results. Theoretical model prepared for comparison to the scanned joints was consistent with recommendations of International Institute of Welding for the effective notch method.

**Key words:** FEM Analysis, Weld, Stress Concentration, 3D Scanning

### 1. INTRODUCTION

Welding is a widely used way to connect elements. This method gives designers the possibility to freely form structures in the manufacturing workshop or on site. Despite the undeniable advantages, this process also has some drawbacks. The welding operation causes residual stress, changes in the structure of the material, forming a structural notch (Blacha et al., 2011a) and also a geometry notch studied in (Blacha et al., 2011b). Obviously, the influence of these defects can be reduced by heat treatment - the heterogeneity of structure and residual stresses, and machining – geometry notch. However, this type of treatment carries a considerable financial outlay. Popularity of welding makes attempts to find methods to better understanding the changes occurring in the material and the effect on the strength of connections is now desirable.

Recent development in 3D laser scanning enables considering almost real weld geometry in fatigue analysis (Alam et al., 2010; Hou, 2007). This field of research requires further investigation which is undertaken in the present article. Specimens were made from S355J2+N steel – a material widely used in the industry. Surface models obtained by the 3D scanning were converted into solid model, additionally prepared and calculated by the finite element method (FEM). The results were compared to those obtained from the model of the weld with the welding toe radius equal to 1 mm, i.e. value recommended by International Institute of Welding (IIW) (Hobbacher 2008) for steel welding joints subjected to cyclic loading. An originality of the present work is building the probability mass function (pmf) (Stewart 2011) of stress for both discrete models of the joints. Selected fatigue criteria were used to calculate the pmf of the equivalent stresses. The aim of the research is to calculate realistic equivalent stress distribution in the butt weld joints and comparison of the result to experimentally obtained fatigue lives.

### 2. PREPARATION OF THE SPECIMENS

The specimens were made from the two 6mm thick metal (S355J2+N) sheets with the dimensions 100x1000mm. Plasma cutting was used to prepare elements. Edges of the plates were milled in order to create correct V butt joint. Welding was conducted by MAG method, with 1.2mm wire, in Ar (92%) and CO<sub>2</sub> (8%) gas shield, without using clamps. The seam was tested by ultrasonic method. The specimens with geometry presented in Fig.1 were obtained from middle part of welded element by saw cutting and milling.

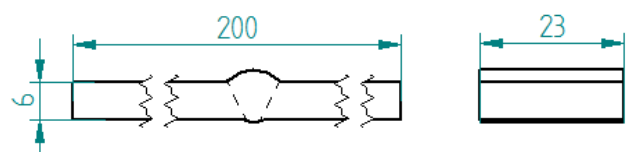


Fig. 1. Geometry of the specimens

#### 2.1. 3D scanning

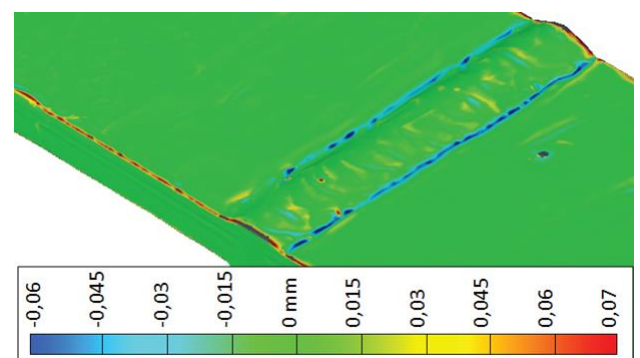


Fig. 2. Mapping accuracy in mm for stereolithography file

3D scanning was used to create numerical models of the specimens. The applied method gives a maximum possibility of mapping accuracy up to 0.02mm. For each side of the specimen 5 scans were performed. Particular scans were combined using markers which were fixed on the specimen surface. A triangle mesh was applied and used as an output. In the next step, files were converted into stereolithography (\*.stl). In Fig.2 difference between scanned data and geometry from stl file for exemplary sample is shown.

## 2.2. Preparing FEM Analysis

In order to speed up the calculations in FEM program, the specimen grips were not modeled. The models were converted into Solid Edge part (\*.par). This type of files could be imported directly into Femap (FEM program). The size of finite elements is not uniform and the density of mesh is considerably increased in the area where stress concentration is expected (Fig.3). Preliminary analysis was conducted to determine the appropriate mesh size. Finally, the maximum length of finite element equal to 0.05mm in the welding toe was chosen (Fig.3).

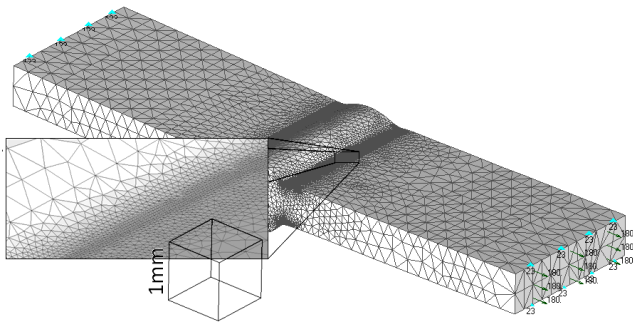


Fig. 3. The geometry of the models with mesh

In the fatigue tests the specimens were subjected to push-pull loading under nominal stress amplitude equal to 180MPa. Thus, the models were calculated under tensile  $\sigma_{nom}=180\text{MPa}$  stress applied to the surface as showed in Fig.3. Loaded surface was constrained in one of his longest edge by blocking translation in  $y$  and  $z$  axes. In the opposite site of the model, the surface is fixed in all directions. The applied constrains imitate fixing in the fatigue testing machine (hydraulic grips).

Besides the scanned specimens the geometry of theoretical model prepared according to International Institute of Welding (Hobbacher 2008) was built for additional FEM analysis. This theoretical model is presented in Fig.4. A welding toe radius equal to 1mm is a value suggested by IIW for the effective notch method. The model was prepared and calculated (mesh and constrains) in the same way as models from scanned specimens.

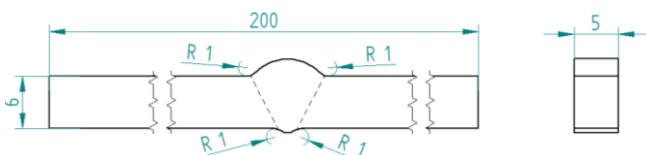


Fig. 4. Geometry of the theoretical model

## 3. RESULTS OF THE FEM ANALYSIS

Static analysis was performed using a linear-elastic model of the body ( $E = 205\text{GPa}$ ,  $\nu = 0.3$ ). Results in the form of principal stresses:  $\sigma_1$ ,  $\sigma_2$ ,  $\sigma_3$  and model geometry were transferred into Matlab software in order to perform subsequent calculations. In the commonly applied (in metallic materials) fatigue criteria (Karolczuk et al., 2005) the multiaxial stress state is reduced to the equivalent one which is used in the fatigue life calculations. The function that reduces multiaxial stress state to the equivalent one depends on hypotheses that were formulated by various researchers. Four well known equivalent stresses were selected to calculate their distribution in butt weld joints. The chosen equivalent stresses have the advantage that they can be presented in the function of principal stresses which simplifies the FEM and subsequent calculations. The first two equivalent stresses came from static hypothesis, i.e. the Huber-Mises-Hencky hypothesis (Eq.1) and the maximum principal stress hypothesis (Eq.2)

$$\sigma_{HMH} = \sqrt{\frac{1}{2}[(\sigma_1 - \sigma_2)^2 + (\sigma_2 - \sigma_3)^2 + (\sigma_3 - \sigma_1)^2]}, \quad (1)$$

$$\sigma_{S1} = \sigma_1. \quad (2)$$

The last two equivalent stresses came from the well-known fatigue criteria, i.e. the Mataka criterion (Eq.3) and the Dang Van criterion (Eq.4). Mataka (1977) assumes that maximum shear stress  $\frac{\sigma_1 - \sigma_3}{2}$  and normal stress  $\frac{\sigma_1 + \sigma_3}{2}$  on the plane of maximum shear stress are critical in respect to fatigue damage

$$\sigma_{MA} = \frac{\sigma_1 - \sigma_3}{2} + k \frac{\sigma_1 + \sigma_3}{2}, k = 2 \frac{\tau_{af}}{\sigma_{af}} - 1, \quad (3)$$

where:  $\tau_{af}$ ,  $\sigma_{af}$  are the fatigue limits for fully reversed torsion and push-pull loadings ( $\tau_{af} = 157\text{MPa}$ ,  $\sigma_{af} = 204\text{MPa}$ ) (Karolczuk 2008). According to Dang Van (1993) the hydrostatic stress  $\frac{\sigma_1 + \sigma_2 + \sigma_3}{3}$  is more important in fatigue analysis than the normal stress

$$\sigma_{DV} = \frac{\sigma_1 - \sigma_3}{2} + a \frac{\sigma_1 + \sigma_2 + \sigma_3}{3}, a = \frac{\tau_{af} - 0.5\sigma_{af}}{\sigma_{af}}. \quad (4)$$

Inhomogeneity of stress distribution in weld joint is clearly presented by probability mass function

$$pmf(\sigma_{HIP}) = \text{Prob}\{\{\sigma = \sigma_{HIP}\}\} = \frac{V(\sigma = \sigma_{HIP})}{V_0}, \quad (5)$$

where  $\sigma_{HIP}$  is a value of stress according to particular hypothesis or criterium ( $HIP = HMH, S1, MA, DV$ ),  $V(\sigma = \sigma_{HIP})$  is a volume of material in weld area and heat affected zone with certain value of the stress  $\sigma_{HIP}$ ,  $V_0$  is a considered volume of material. Probability mass function (Eq.5) is a function that gives the probability of occurrence of a certain equivalent stress value in the weld joint.

In Fig. 5 an exemplary equivalent stress distribution in one of the weld joint is shown.

Figs. 6-9 presents the pmf functions for the specimens and for a theoretical model (showed in red colour). Maximum values of stress for each specimen are shown in Tab. 1. The bold and underlines values in Tab. 1 show the most locally stressed specimen. According to that computation it is expected that the specimen 1 will exhibit the shortest fatigue life.

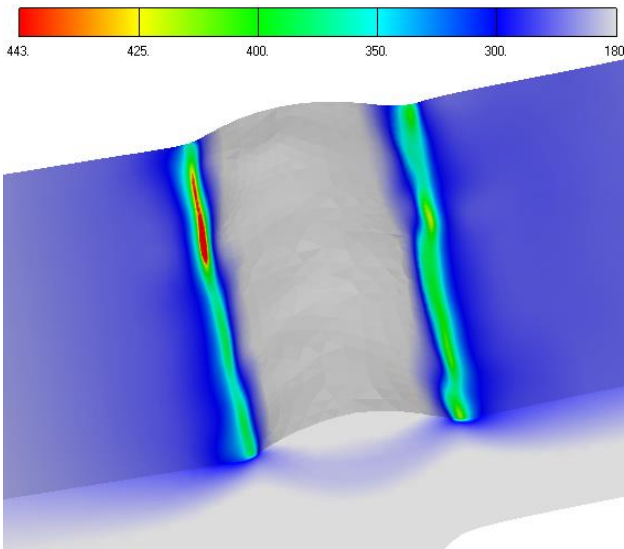


Fig. 5. The Huber-Mises-Hencky stress distribution

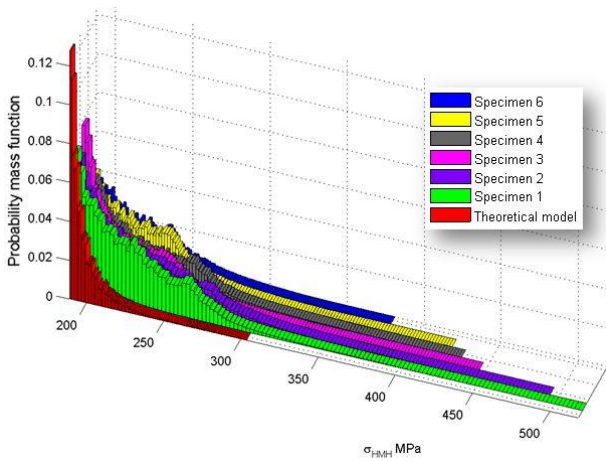


Fig. 6. Probability mass function for the Huber-Mises-Hencky stress

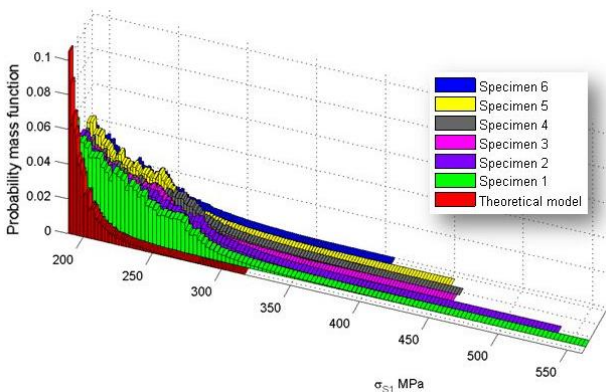


Fig. 7. Probability mass function for the Maximal Principal Stress

Comparing the pmf of equivalent stresses obtained for the scanned specimens and the theoretical model it is concluded that the pmf of theoretical model has only one extreme that corresponds to the nominal stress. The pmf for the Dang Van and Mataka criteria differs from the other criteria because these stresses are equivalent to shear stresses (to the torsion tests) instead of tensile stresses (to the push-pull test). Moreover, the

pmf for scanned specimens shows that higher equivalent stresses occupy larger volume of material than it is for the theoretical model. The maximal values of computed stresses for each hypothesis presented in table 1 vary in proportional way, i.e. the highest stresses for all hypotheses exist in specimen number 1 and the lowest stresses exist in specimen number 6.

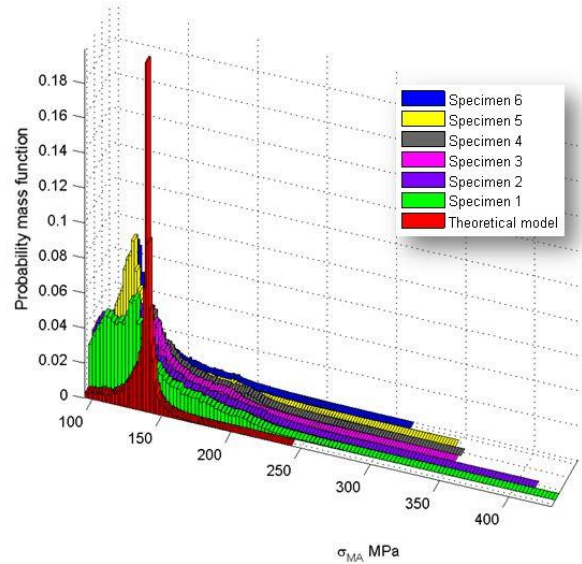


Fig. 8. Probability mass function for the Mataka criterion

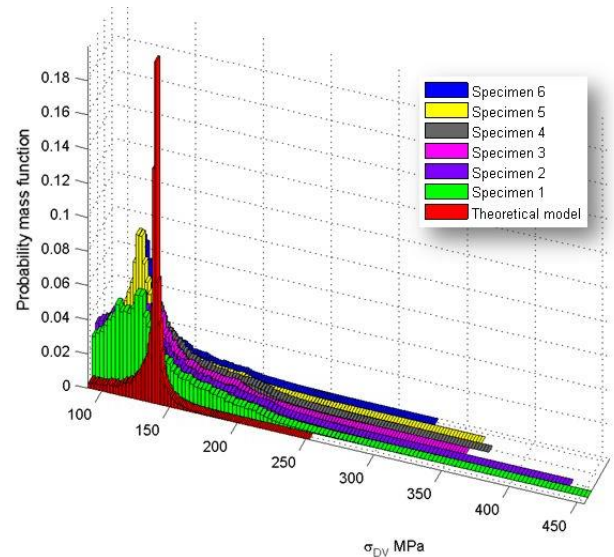


Fig. 9. Probability mass function for the Dang Van criterion

Tab. 1. Values of the maximum equivalent stresses in MPa (nominal stress 180MPa) according to the particular hypothesis

Specimens	Hypothesis			
	HMH	S1	MA	DV
theoretical	303.7	316.9	243.2	252.7
<b>1</b>	<b>518.5</b>	<b>560.9</b>	<b>430.5</b>	<b>455.0</b>
2	494.7	538.1	413.2	438.9
3	446.2	459.6	352.9	359.9
4	432.1	461.5	354.5	374.1
5	423.3	452.6	347.7	366.0
6	380.9	406.7	312.6	328.8

#### 4. EXPERIMENTAL TESTS

The analysed specimens were experimentally tested under cyclic push-pull loading with controlled nominal stress amplitude  $\sigma_{an}$ . The fatigue lives  $N_{exp}$  until complete rupture of the specimens are reported in Tab. 2.

Tab. 2. Results of experimental push-pull tests

Specimens	$\sigma_{an}$ , MPa	$N_{exp}$ , cycles
1	180	146 200
2	180	169 590
3	180	267 350
4	180	85 260
5	180	38 530
6	180	39 400

#### 5. ANALYSIS OF THE RESULTS

Experimental fatigue lives of the tested specimens exhibit large scatter. The ratio between longest fatigue life to shortest is equal to 6.9 ( $\max(N_{exp})/\min(N_{exp})$ ) and the ratios in respect to mean value is 2.1 and 0.31 ( $\max(N_{exp})/\text{mean}(N_{exp})$  and  $\min(N_{exp})/\text{mean}(N_{exp})$ ). It was expected that fatigue lives obtained under the same nominal stress amplitude (180 MPa) could be correlated with maximum value of local stress computed using FEM and real shape of the weld joints. Fig. 10 presents no correlation between experimental fatigue lives  $N_{exp}$  and maximum stresses computed according to analyzed hypothesis. Moreover, in spite of multiaxial stress state due to high stress concentration and different function for equivalent stresses, the relation between computed maximal stresses  $\sigma_{HIP}$  and fatigue lives  $N_{exp}$  for all hypothesis has the same character. The trials to find the correlation between parameters of the pmf functions and experimental fatigue lives were not successful. However, it must be remembered that the pmf shows the probability of occurrence of equivalent stress value in the weld joint volume without consideration of its location in the joint.

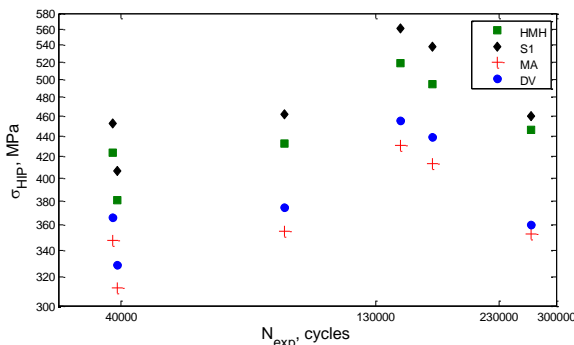


Fig. 10. Relation between number of cycles to failure  $N_{exp}$  and maximum values of equivalent stresses for the analysed hypotheses

#### 6. CONCLUSIONS

The graph of the probability mass function allows analysing the probability of occurrence of equivalent stress values and its inhomogeneous distribution. From the comparison of the results obtained from the real (specimen) and the reference (theoretical)

elements it can be stated that the stresses in the real structure are higher and larger volume of joint is exposed to high (greater than nominal) stresses.

Experimental tests for a given number of specimens showed lack of convergence between the highest equivalent stresses and the lowest fatigue lives. Similar conclusions were obtained by Hou C-Y (2007) but they are in contrary to results obtained by Chapetti M.D. et al (1995). However, it must be noted that Chapetti M.D. et al (1995) did not calculate stresses using real surface topography but they compared experimental fatigue life obtained for specimens with different toe weld period.

Moreover, in spite of different assumptions made in the analysed fatigue criteria the maximal equivalent stresses changes in proportional way between the analysed fatigue criteria (Fig. 10).

It turns out that the changes in geometry of the weld joint surface and stress concentration due this fact is not dominating in fatigue damage process. It is necessary in the calculations to take into account other factors affecting fatigue life such as: (i) initial deformation of specimen caused by weld shrinkage, (ii) stress distribution (not only the highest stress, crack coalescence), (iii) stress gradient effect, (iv) residual stress distribution.

#### REFERENCES

1. Alam M.M., Barsoum Z., Jonsén P., Kaplan A.F.H., Häggblad H.A. (2010), The Influence of Surface Geometry And Topography on the Fatigue Cracking Behaviour of laser Hybrid Welded Eccentric Fillet Joints, *Applied Surface Science*, 256, 1936–1945.
2. Blacha Ł., Karolczuk A., Bański R., Stasiuk P. (2011a), Experimental Study of Fatigue Life of Cruciform Welded Joints with Reference to Scale Effect, *Acta Mechanica et Automatica*, Vol 5, No.3, 16-20 (in Polish).
3. Blacha Ł., Karolczuk A., Łagoda T. (2011b), Modeling of Stress in Welded Joints Under Consideration of Plastic Strains in Fatigue Life Calculations, *Materials Testing*, vol 53, 339-343.
4. Chapetti M.D., Otegui J.L. (1995), Importance of Toe Irregularity for Fatigue Resistance of Automatic Welds, *International Journal of Fatigue*, Vol. 17, 531–538.
5. Dang Van K. (1993), Macro-micro Approach in High-Cycle Multiaxial Fatigue, In *Advances in Multiaxial Fatigue*. (Edited by McDowell, D.L. and Ellis, R.) American Society for Testing and Materials STP 1191. Philadelphia, 120–130.
6. Hobbacher A. (2008), Recommendations for Fatigue Design of Welded Joint and Components, *IIV document IIV-1823-07 ex XIII-2151r4-07/XV-1254r4-07*.
7. Hou C-Y. (2007), Fatigue Analysis of Welded Joints with the aid of Real Three-Dimensional Weld Toe Geometry, *International Journal of Fatigue*, 29, 772-785.
8. Karolczuk A. (2008), Non-local Area Approach to Fatigue Life Evaluation under Combined Reversed Bending and Torsion, *International Journal of Fatigue*, 30, 1985-1996.
9. Karolczuk A., Blacha Ł. (2011), Application of the Weakest Link Concept to Fatigue Analysis of Welded Joints, *Acta Mechanica et Automatica*, Vol.5 No. 3, 51-54 (in Polish).
10. Karolczuk A., Macha E. (2005), Critical Planes in Multiaxial Fatigue, *Materials Science Forum*, Vol. 482, 109-114.
11. Matake T. (1977), An Explanation on Fatigue Limit under Combined Stress. *Bulletin of the The Japan Society of Mechanical Engineers* 20, 257–263.
12. Stewart W.J. (2011), Probability, Markov Chains, Queues, and Simulation. *The Mathematical Basis of Performance Modeling*. Princeton University Press, 105.

The project financed from the funds of the National Centre of Science – decision number 2011/01/B/ST8/06850.

# STRESS DISTRIBUTION IN A COMPOSITE COATING BY LOCAL LOADING OF THE FREE SURFACE

Roman KULCHYTSKY-ZHYHAILO\*, Waldemar KOŁODZIEJCZYK\*

\*Faculty of Mechanical Engineering, Białystok University of Technology  
ul. Wiejska 45C, 15-351 Białystok, Poland

r.kulczycki@pb.edu.pl, w.kolodziejczyk@pb.edu.pl

**Abstract:** A three-dimensional problem of the theory of elasticity for halfspace with multilayered coating with periodical structure is considered. The fundamental layer consists of two layers with different thicknesses and different mechanical properties. The coating is described by the homogenized model with microlocal parameters. The solution is derived by using integral Fourier transform. Calculations were conducted with the assumption of elliptical distribution of normal and tangential tractions applied to the surface of the layered system in a circular area. Analysis of the stresses was restricted to the first principal stress distribution.

**Key words:** Gradient Coating, Three-Dimensional Problem of Elasticity, Normal Loading, Shear Loading

## 1. INTRODUCTION

In the mechanics of contact interaction, much attention is now given to coatings used for the improvement of the tribological characteristics of friction couples. Thus, the coatings formed by periodically deposited elastic layers are now extensively investigated (Farhat et al., 1997; Voevodin et al., 2001) parallel with the uniform coatings (Schwarzer 2000; Bargallini et al., 2003; Kulchytsky-Zhyhailo and Rogowski, 2010) and nonuniform coatings whose mechanical properties are described by continuous functions of the distance from the surface (Guler and Erdogan, 2007; Liu et al., 2008; Kulchytsky-Zhyhailo and Bajkowski, 2010). In the analysis of the stressed state, the researchers, as a rule, focus their attention on the evaluation of the tensile and Huber-Mises stresses described by the second invariant of the deviator of the stress tensor.

Considering contact problems for multilayered coatings in classical approach we need to solve partial differential equations for every sublayer and satisfy continuity conditions on the interfaces.

A coating with periodical structure can be replaced by a homogeneous one by using e.g. homogenized model with microlocal parameters (Matysiak and Woźniak, 1987; Woźniak, 1987).

As it was show in earlier papers (Kołodziejczyk and Kulchytsky-Zhyhailo, 2013; Kulchytsky-Zhyhailo and Kołodziejczyk, 2005; Kulchytsky-Zhyhailo, 2011) the stress distribution in the substitute homogeneous medium is a good approximation of stress distribution in the multilayered medium when the ratio of thickness of a fundamental layer to a specific size of contact area is less than 0.1.

In the present work, we consider a three-dimensional problem of elastic half space with laminated coating of periodic structure loaded by normal and tangential tractions.

The multilayered coating is replaced by a homogeneous one which mechanical properties are described by the homogenized model with microlocal parameters. The objective of this work is to determine relations between applied loading and stresses in the coating and in the substrate as well as analysis of tensile stresses and Huber-Mises stresses in the coating due to loading applied in a circular area on the free surface.

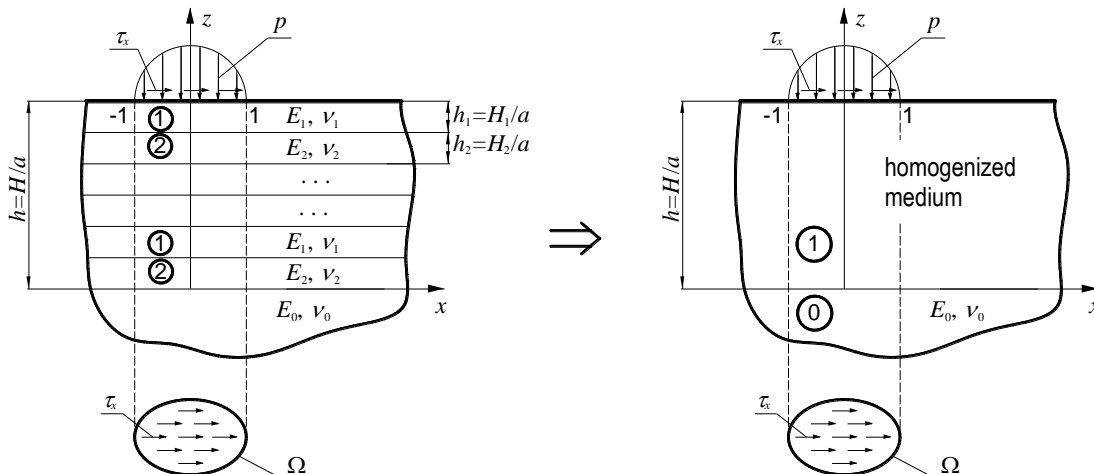


Fig. 1. The scheme of the problem

## 2. FORMULATION OF THE PROBLEM

Let us consider a non-uniform elastic half-space loaded by normal  $p$  and tangential  $\tau_x$  traction in the region  $\Omega$  with the specific size  $a$  on the free surface (Fig. 1). The non-uniform half space is formed by the homogeneous isotropic half space with Young's modulus  $E_0$  and Poisson's ratio  $\nu_0$  and a system of two periodically deposited elastic layers with thicknesses  $H_1$  and  $H_2$  ( $H = H_1 + H_2$  is the thickness of the fundamental layer), Young's moduli  $E_1$  and  $E_2$ , and Poisson's ratios  $\nu_1$  and  $\nu_2$ , respectively. Assume that the conditions of perfect mechanical contact are realized between the layers of the coating and between the coating and the substrate.

Since the nonhomogeneous coating is described by the homogenized model with microlocal parameters (Matysiak and Woźniak, 1987; Woźniak, 1987) the governing equations take the form:

$$A_1 u_{x,xx}^{(1)} + 0.5(A_1 - A_2) u_{x,yy}^{(1)} + A_5 u_{x,zz}^{(1)} + 0.5(A_1 + A_2) u_{y,xy}^{(1)} + (A_3 + A_5) u_{z,xz}^{(1)} = 0, \quad (1a)$$

$$0.5(A_1 - A_2) u_{y,xx}^{(1)} + A_1 u_{y,yy}^{(1)} + A_5 u_{y,zz}^{(1)} + 0.5(A_1 + A_2) u_{x,xy}^{(1)} + (A_3 + A_5) u_{z,yz}^{(1)} = 0, \quad (1b)$$

$$A_5 (u_{z,xx}^{(1)} + u_{z,yy}^{(1)}) + A_4 u_{z,zz}^{(1)} + (A_3 + A_5) (u_{x,xz}^{(1)} + u_{y,yz}^{(1)}) = 0, \quad (1c)$$

where  $\mathbf{u}^{(1)}$  – macro-displacements vector (displacements averaged in a fundamental layer),  $x, y, z$  – dimensionless coordinates (Cartesian coordinates related to a specific size of contact area  $a$ ),  $f_{,k} = \partial f / \partial k$ ,  $k = x, y, z$ ,  $A_i$ ,  $i = 1, 2, \dots, 5$  – coefficients calculated from known relations (Matysiak and Woźniak, 1987; Kaczyński, 1994; Kulchitsky-Zhyhailo, 2011; Kołodziejczyk and Kulchitsky-Zhyhailo, 2013) on the base of mechanical and geometrical properties of alternating layers:

$$A_1 = \tilde{\lambda} + 2\tilde{\mu} - \frac{[\lambda]^2}{\hat{\lambda} + 2\hat{\mu}}, \quad A_2 = \tilde{\lambda} - \frac{[\lambda]^2}{\hat{\lambda} + 2\hat{\mu}},$$

$$A_3 = \tilde{\lambda} - \frac{[\lambda]([\lambda] + 2[\mu])}{\hat{\lambda} + 2\hat{\mu}},$$

$$A_4 = \tilde{\lambda} + 2\tilde{\mu} - \frac{([\lambda] + 2[\mu])^2}{\hat{\lambda} + 2\hat{\mu}}, \quad A_5 = \tilde{\mu} - \frac{[\mu]^2}{\hat{\mu}},$$

$$\tilde{\lambda} = \eta\lambda_1 + (1-\eta)\lambda_2, \quad \tilde{\mu} = \eta\mu_1 + (1-\eta)\mu_2,$$

$$[\lambda] = \eta(\lambda_1 - \lambda_2), \quad [\mu] = \eta(\mu_1 - \mu_2),$$

$$\hat{\lambda} = \eta\lambda_1 + \frac{\eta^2}{1-\eta}\lambda_2, \quad \hat{\mu} = \eta\mu_1 + \frac{\eta^2}{1-\eta}\mu_2, \quad \eta = \frac{H_1}{H},$$

$$\lambda_i = \frac{E_i \nu_i}{(1 + \nu_i)(1 - 2\nu_i)}, \quad \mu_i = \frac{E_i}{2(1 + \nu_i)}.$$

Equations (1) have the same form as equations of theory of elasticity for a transversely isotropic solid. Therefore their solution can be expressed in terms of elastic potentials proper to a transversely isotropic medium (Elliot, 1949):

$$u_x^{(1)} = \Psi_{1,x} + \Psi_{2,x} + \Psi_{3,y}, \quad u_y^{(1)} = \Psi_{1,y} + \Psi_{2,y} - \Psi_{3,y}, \\ u_z^{(1)} = \kappa_1 \Psi_{1,z} + \kappa_2 \Psi_{2,z}, \quad (2a)$$

where elastic potentials satisfy equations:

$$\Psi_{i,xx} + \Psi_{i,yy} + \gamma_i^2 \Psi_{i,zz} = 0, \quad (2b)$$

$\gamma_i^2$ ,  $i = 1, 2$  are roots of the characteristic equation:

$$A_1 A_5 \gamma^4 + (A_5^2 + 2A_3 A_5 - A_1 A_4) \gamma^2 + A_4 A_5 = 0,$$

$$\kappa_i = \frac{\gamma_i^2 A_1 - A_5}{A_3 + A_5}, \quad \gamma_3^2 = \frac{2A_5}{A_1 - A_2}.$$

Considered boundary problem, formulated in dimensionless coordinates related to the specific size  $a$  of the loading area, leads to equations of theory of elasticity (2b) defined in the appropriate homogenized medium and equations

$$(1 - 2\nu_0) \Delta \mathbf{u}^{(0)} + \text{grad div } \mathbf{u}^{(0)} = 0 \quad (3)$$

defined in the substrate, with boundary conditions:

– normal and tangential tractions on the surface,

$$\sigma_{zz}^{(1)}(x, y, z) = -p(x, y), \quad \sigma_{xz}^{(1)}(x, y, h) = \tau_x(x, y), \quad (4a)$$

$$\sigma_{yz}^{(1)}(x, y, h) = 0, \quad (x, y) \in \Omega, \quad (4b)$$

– ideal contact between coating and substrate,

$$u_x^{(0)}(x, y, 0) = u_x^{(1)}(x, y, 0), \quad u_y^{(0)}(x, y, 0) = u_y^{(1)}(x, y, 0), \quad (4c)$$

$$u_z^{(0)}(x, y, 0) = u_z^{(1)}(x, y, 0), \quad (4d)$$

$$\sigma_{zz}^{(0)}(x, y, 0) = \sigma_{zz}^{(1)}(x, y, 0), \quad \sigma_{xz}^{(0)}(x, y, 0) = \sigma_{xz}^{(1)}(x, y, 0), \quad (4e)$$

$$\sigma_{yz}^{(0)}(x, y, 0) = \sigma_{yz}^{(1)}(x, y, 0), \quad (4f)$$

– vanishing displacement components:

$$u_x^{(i)}, u_y^{(i)}, u_z^{(i)} \rightarrow 0, \quad x^2 + y^2 + z^2 \rightarrow -\infty, \quad i=0,1, \quad (4g)$$

where  $\mathbf{u}^{(0)}$  is the displacement vector in the substrate.

The characteristic feature of the homogenized model is that it gives different expressions for calculation of the stress tensor components, which experience a jump on the interfaces between layers.

$$\sigma_{xx}^{(1,k)} = K_k u_{x,x}^{(1)} + L_k u_{y,y}^{(1)} + M_k u_{z,z}^{(1)}, \quad k=1,2, \quad (5a)$$

$$\sigma_{yy}^{(1,k)} = L_k u_{x,x}^{(1)} + K_k u_{y,y}^{(1)} + M_k u_{z,z}^{(1)}, \quad k=1,2, \quad (5b)$$

$$\sigma_{xy}^{(1,k)} = \mu_k (u_{x,y}^{(1)} + u_{y,x}^{(1)}), \quad k=1,2, \quad (5c)$$

where  $\sigma^{(1,k)}$  is the stress tensor in  $k$  – th layer of the fundamental layer ( $k = 1, 2$ ),  $K_k$ ,  $L_k$ ,  $M_k$  – coefficients calculated from known expressions (Kaczyński, 1994):

$$K_k = \lambda_k + 2\mu_k - h_k \lambda_k \frac{[\lambda]}{\hat{\lambda} + 2\hat{\mu}}, \quad L_k = \lambda_k - h_k \lambda_k \frac{[\lambda]}{\hat{\lambda} + 2\hat{\mu}},$$

$$M_k = \lambda_k - h_k \lambda_k \frac{[\lambda] + 2[\mu]}{\hat{\lambda} + 2\hat{\mu}}, \quad h_1 = 1, \quad h_2 = -\frac{\eta}{1-\eta}.$$

It is essential to note that discussed stresses differ significantly in the individual sublayers composing a fundamental layer (Kulchitsky-Zhyhailo, 2011; Kulchitsky-Zhyhailo and Kołodziej-

czyk, 2005; Kołodziejczyk and Kulchytzky-Zhyhailo, 2013).

The remaining stress tensor components can be obtained using the following relations:

$$\sigma_{zz}^{(1)} = \sigma_{zz}^{(1,k)} = A_3(u_{x,x}^{(1)} + u_{y,y}^{(1)}) + A_4 u_{z,z}^{(1)}, \quad k = 1, 2, \quad (5d)$$

$$\sigma_{xz}^{(1)} = \sigma_{xz}^{(1,k)} = A_5(u_{x,z}^{(1)} + u_{z,x}^{(1)}), \quad k = 1, 2, \quad (5e)$$

$$\sigma_{yz}^{(1)} = \sigma_{yz}^{(1,k)} = A_5(u_{y,z}^{(1)} + u_{z,y}^{(1)}), \quad k = 1, 2. \quad (5f)$$

### 3. SOLUTION OF THE PROBLEM

General solution of differential equations defined in the coating and in the substrate we obtain using two-dimensional Fourier transform:

$$\tilde{f}(\xi, \eta, z) = \frac{1}{2\pi} \int_{-\infty}^{+\infty} \int f(x, y, z) \exp(-ix\xi - iy\eta) dx dy.$$

The Fourier transforms of the elastic potentials have the following form:

$$\tilde{\Psi}_i = s^{-2} a_{2i-1}(\xi, \eta) \sinh(\gamma_i^{-1} s(h-z)) + s^{-2} a_{2i}(\xi, \eta) \cosh(\gamma_i^{-1} s(h-z)), \quad i = 1, 2, 3. \quad (6)$$

The solution in the substrate can be expressed as:

$$s^2 \tilde{u}_x^{(0)}(\xi, \eta, z) = -i\xi \tilde{\theta}_1^{(0)}(\xi, \eta, z) - i\eta \tilde{\chi}^{(0)}(\xi, \eta, z), \quad (7a)$$

$$s^2 \tilde{u}_y^{(0)}(\xi, \eta, z) = -i\eta \tilde{\theta}_1^{(0)}(\xi, \eta, z) + i\xi \tilde{\chi}^{(0)}(\xi, \eta, z), \quad (7b)$$

$$2\tilde{u}_z^{(0)}(\xi, \eta, z) = (d_0 z a_{-1}(\xi, \eta) + 2a_0(\xi, \eta)) \exp(sz), \quad (7c)$$

where

$$2\tilde{\theta}_1^{(0)}(\xi, \eta, z) = -[(2 + d_0) a_{-1}(\xi, \eta) + d_0 s z a_{-1}(\xi, \eta) + 2a_0(\xi, \eta) s] \exp(sz), \quad (7d)$$

$$\tilde{\chi}^{(0)}(\xi, \eta, z) = a_7(\xi, \eta) \exp(sz). \quad (7e)$$

Formulas (6) and (7) contain 9 unknown functions of the transform parameter. Satisfying boundary conditions we obtain two systems of algebraic equations to determine unknown functions. They contain 6 and 3 equations respectively:

$$(A_3 - A_4 \kappa_1 \gamma_1^{-2}) a_2(\xi, \eta) + (A_3 - A_4 \kappa_2 \gamma_2^{-2}) a_4(\xi, \eta) = \tilde{p}(\xi, \eta), \quad (8a)$$

$$(\kappa_1 + 1) \gamma_1^{-1} a_1(\xi, \eta) + (\kappa_2 + 1) \gamma_2^{-1} a_3(\xi, \eta) = \frac{i\xi}{A_5 s} \tilde{\tau}_x(\xi, \eta), \quad (8b)$$

$$\sum_{i=1}^2 \kappa_i \gamma_i^{-1} (a_{2i-1}(\xi, \eta) c_i + a_{2i}(\xi, \eta) s_i) + a_0 s = 0, \quad (8c)$$

$$2 \sum_{i=1}^2 (a_{2i-1}(\xi, \eta) s_i + a_{2i}(\xi, \eta) c_i) - (2 + d_0) a_{-1}(\xi, \eta) - 2a_0(\xi, \eta) s = 0, \quad (8d)$$

$$\sum_{i=1}^2 (A_4 \kappa_i \gamma_i^{-2} - A_3) (a_{2i-1}(\xi, \eta) s_i + a_{2i}(\xi, \eta) c_i) - \mu_0 (a_{-1}(\xi, \eta) + 2a_0(\xi, \eta) s) = 0, \quad (8e)$$

$$A_5 \sum_{i=1}^2 (\kappa_i + 1) \gamma_i^{-1} (a_{2i-1}(\xi, \eta) c_i + a_{2i}(\xi, \eta) s_i) + \mu_0 ((1 + d_0) a_{-1}(\xi, \eta) + 2a_0(\xi, \eta) s) = 0, \quad (8f)$$

$$\gamma_3^{-1} a_5(\xi, \eta) = \frac{i\eta}{A_5 s} \tilde{\tau}_x(\xi, \eta), \quad (9a)$$

$$a_5(\xi, \eta) s_3 + a_6(\xi, \eta) c_3 + b_0(\xi, \eta) = 0, \quad (9b)$$

$$A_5 \gamma_3^{-1} (a_5(\xi, \eta) c_3 + a_6(\xi, \eta) s_3) - \mu_0 a_7(\xi, \eta) = 0. \quad (9c)$$

where:  $c_i = \cosh(\gamma_i^{-1} s h)$ ,  $s_i = \sinh(\gamma_i^{-1} s h)$ ,  $i = 1, 2, 3$ .

Solution of these two systems of equations can be normalized as follows:

$$a_j(\xi, \eta) = \frac{\tilde{p}(\xi, \eta)}{A_5} a_j^{(p)}(s) - \frac{i\xi \tilde{\tau}_x(\xi, \eta)}{s A_5} a_j^{(\tau)}(s), \quad i = -1, 0, \dots, 4, \quad (10a)$$

$$a_j(\xi, \eta) = -\frac{i\eta \tilde{\tau}_x(\xi, \eta)}{s A_5} a_j^{(\tau)}(s), \quad i = 5, 6, 7. \quad (10b)$$

Solving obtained linear equations and taking into account relationship between displacements and stresses and elastic potentials we obtain solution of the problem in Fourier transform domain.

$$\tilde{\sigma}_{xx}^{(p)} = \left( S_{xy1}^{(p)}(s, z) - \frac{\eta^2}{s^2} S_{xy2}^{(p)}(s, z) \right) \tilde{p}(\xi, \eta), \quad (11a)$$

$$\tilde{\sigma}_{yy}^{(p)} = \left( S_{xy1}^{(p)}(s, z) - \frac{\xi^2}{s^2} S_{xy2}^{(p)}(s, z) \right) \tilde{p}(\xi, \eta), \quad (11b)$$

$$\tilde{\sigma}_{zz}^{(p)} = -S_{z1}^{(p)}(s, z) \tilde{p}(\xi, \eta), \quad (11c)$$

$$\tilde{\sigma}_{xy}^{(p)} = \frac{\xi \eta}{s^2} S_{xy2}^{(p)}(s, z) \tilde{p}(\xi, \eta), \quad (11d)$$

$$\tilde{\sigma}_{xz}^{(p)} = \frac{i\xi}{s} S_{z2}^{(p)}(s, z) \tilde{p}(\xi, \eta), \quad (11e)$$

$$\tilde{\sigma}_{yz}^{(p)} = \frac{i\eta}{s} S_{z2}^{(p)}(s, z) \tilde{p}(\xi, \eta), \quad (11f)$$

$$\tilde{\sigma}_{xx}^{(\tau)} = -\frac{i\xi}{s} \left( S_{xy1}^{(\tau)}(s, z) - \frac{\eta^2}{s^2} (S_{xy2}^{(\tau)}(s, z) - 2S_{xy3}^{(\tau)}(s, z)) \right) \tilde{\tau}_x(\xi, \eta), \quad (12a)$$

$$\tilde{\sigma}_{yy}^{(\tau)} = -\frac{i\xi}{s} \left[ (S_{xy1}^{(\tau)}(s, z) - S_{xy2}^{(\tau)}(s, z)) + \eta^2 s^{-2} (S_{xy2}^{(\tau)}(s, z) - 2S_{xy3}^{(\tau)}(s, z)) \right] \tilde{\tau}_x(\xi, \eta), \quad (12b)$$

$$\tilde{\sigma}_{zz}^{(\tau)} = \frac{i\xi}{s} S_{z1}^{(\tau)}(s, z) \tilde{\tau}_x(\xi, \eta), \quad (12c)$$

$$\tilde{\sigma}_{xy}^{(\tau)} = -\frac{i\eta}{s} \left( S_{xy3}^{(\tau)}(s, z) + \frac{\xi^2}{s^2} (S_{xy2}^{(\tau)}(s, z) - 2S_{xy3}^{(\tau)}(s, z)) \right) \tilde{\tau}_x(\xi, \eta), \quad (12d)$$

$$\tilde{\sigma}_{xz}^{(\tau)} = \left( \frac{\xi^2}{s^2} S_{z_2}^{(\tau)}(s, z) + \frac{\eta^2}{s^2} S_{z_3}^{(\tau)}(s, z) \right) \tilde{\tau}_x(\xi, \eta), \quad (12e)$$

$$\tilde{\sigma}_{yz}^{(\tau)} = \frac{\xi\eta}{s^2} \left( S_{z_2}^{(\tau)}(s, z) - S_{z_3}^{(\tau)}(s, z) \right) \tilde{\tau}_x(\xi, \eta), \quad (12f)$$

where the form of introduced functions  $S$  depends on the location of the investigated point. Moreover functions with subscripts  $xy$  defined in the coating depend on the number of a sublayer in a fundamental layer and are given by:

$$S_{xy1}^{(j,k)} = \sum_{i=1}^2 A_5^{-1} (M_k \kappa_i \gamma_i^{-2} - K_k) (a_{2i-1}^{(j)} S_i + a_{2i}^{(j)} C_i), \quad j = p, \tau, k = 1, 2$$

$$S_{xy2}^{(j,k)} = -2A_5^{-1} \mu_k \sum_{i=1}^2 (a_{2i-1}^{(j)} S_i + a_{2i}^{(j)} C_i), \quad j = p, \tau, k = 1, 2,$$

$$S_{xy3}^{(\tau,k)} = -A_5^{-1} \mu_k (a_5^{(\tau)} S_3 + a_6^{(\tau)} C_3), \quad k = 1, 2,$$

$$S_{z1}^{(j)} = \sum_{i=1}^2 A_5^{-1} (A_3 - A_4 \kappa_i \gamma_i^{-2}) (a_{2i-1}^{(j)} S_i + a_{2i}^{(j)} C_i), \quad j = p, \tau,$$

$$S_{z2}^{(j)} = -\sum_{i=1}^2 (\kappa_i + 1) \gamma_i^{-1} (a_{2i-1}^{(j)} C_i + a_{2i}^{(j)} S_i), \quad j = p, \tau,$$

$$S_{z3}^{(\tau)} = -\gamma_3^{-1} (a_5^{(\tau)} C_3 + a_6^{(\tau)} S_3),$$

where:

$$S_i = \sinh(\gamma_i^{-1} s(h-z)), \quad C_i = \cosh(\gamma_i^{-1} s(h-z)), \quad i = 1, 2, 3.$$

The corresponding functions in the substrate are as follows:

$$\mu_0^{-1} A_5 S_{xy1}^{(j)} = -((2d_0 + 1)a_{-1}^{(j)} + d_0 s z a_{-1}^{(j)} + 2a_0^{(j)} s) \exp(s z),$$

$$\mu_0^{-1} A_5 S_{xy2}^{(j)} = -((d_0 + 2)a_{-1}^{(j)} + d_0 s z a_{-1}^{(j)} + 2a_0^{(j)} s) \exp(s z),$$

$$\mu_0^{-1} A_5 S_{z1}^{(j)} = -(a_{-1}^{(j)} + d_0 s z a_{-1}^{(j)} + 2a_0^{(j)} s) \exp(s z),$$

$$\mu_0^{-1} A_5 S_{z2}^{(j)} = ((d_0 + 1)a_{-1}^{(j)} + d_0 s z a_{-1}^{(j)} + 2a_0^{(j)} s) \exp(s z), \quad j = p, \tau,$$

$$\mu_0^{-1} A_5 S_{xy3}^{(\tau)} = -\mu_0^{-1} A_5 S_{z3}^{(\tau)} = a_7^{(\tau)} \exp(s z).$$

Taking the inverse Fourier integral transforms, we obtain relations (in terms of double integrals) between displacement vector components and stress tensor components in the coating and in the substrate and functions describing loading distributions.

#### 4. RESULTS AND DISCUSSIONS

Calculations were made under assumptions:

- the tangential tractions are related to the normal tractions by the Amontons-Coulomb law of friction:  $\tau_x = f p$  where  $f$  is the friction coefficient
- the axisymmetrical pressure in the form  $\left(\frac{p}{p_0}\right)^2 = 1 - r^2$  ( $r^2 = x^2 + y^2$ ) is applied over a circular area of radius  $a$ .
- mechanical properties of the substrate and the coating as well as the thickness ratio of sublayers forming fundamental layer were taken from the literature (Voevodin et al., 2001). Details are given in Tab. 1.

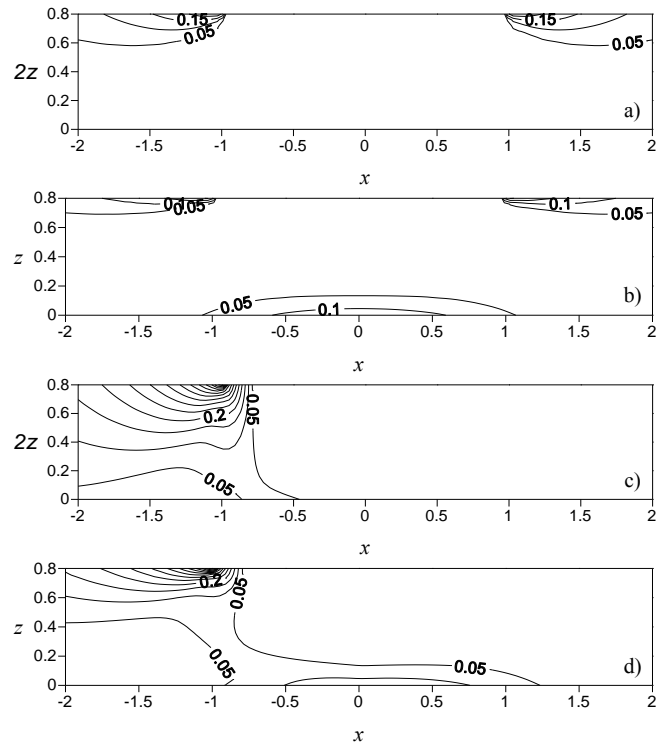
**Tab. 1.** Mechanical and geometrical properties elements of the discussed non-uniform half space

Material	$E$ (GPa)	$\nu$	$H_1/H_2$
substrate	Steel	220	0.25
coating	TiN	440	0.18
	Ti	120	0.32

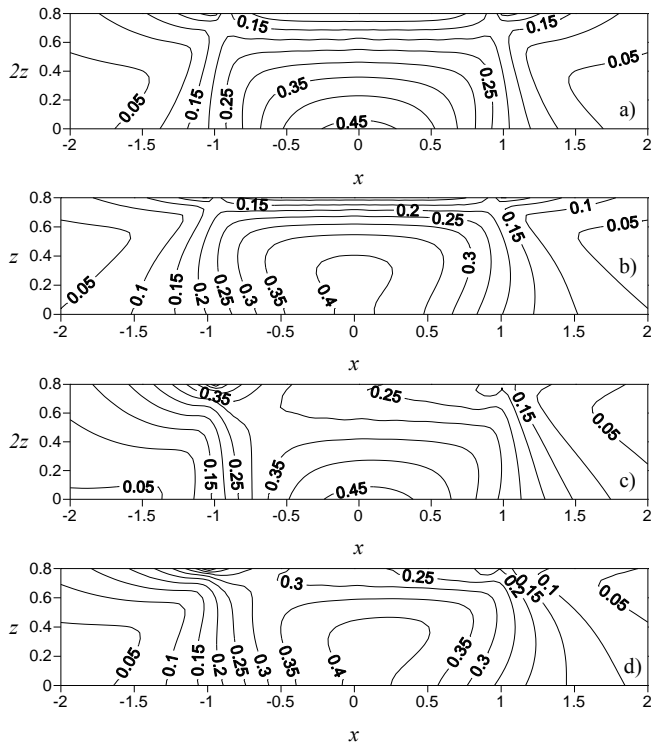
The integrals at internal points of the nonuniform half space ( $z < h$ ) are taken with the help of the Gaussian quadrature. On the surface  $z = h$ , we take into account the asymptotic behavior of the solution of the system of equations obtained as the parameter of the integral transformation tends to infinity. The integrals in which the integrands are replaced by their asymptotics are taken analytically. To find the remaining integrals, we apply the Gaussian quadrature.

Fig. 2 illustrates distributions of the first principal stress  $\sigma_1$  in sublayers of the coating with greater Young modulus in the plane  $y = 0$ . Figs. (2a) and (2b) show an interaction in case of normal traction. Contours of  $\sigma_1$  distribution caused by tangential tractions are shown in Figs. (2c) and (2d). It can be seen that tensile stresses arise on the unloaded part of the surface of the half-space. The maximum value of  $\sigma_1$  appears close to the point  $x = -1$ ,  $y = 0$ ,  $z = h$  and increases with increasing value of the friction coefficient. For specific thickness of the coating tensile stresses additionally appear in the vicinity of the coating-substrate interface.

Fig. 3 show distributions of the second invariant of deviatoric stress tensor  $J_2$  ( $\sigma_{HM} = \sqrt{3}J_2$ ) in sublayers with greater Young modulus. It can be distinguished two local maxima of  $J_2$ : (1) at the point  $x \approx -1$ ,  $y = 0$ ,  $z = h$  (2) on the coating-substrate interface or in its vicinity.



**Fig. 2.** Distribution of the first principal stress  $\sigma_1$  in sublayers with greater Young modulus in regions in which  $\sigma_1 > 0.05$ :  
 a)  $h = 0.4$ ,  $f = 0$ ; b)  $h = 0.8$ ,  $f = 0$ ; c)  $h = 0.4$ ,  $f = 0.25$ ; d)  $h = 0.8$ ,  $f = 0.25$ .



**Fig. 3.** Distributions of the second invariant of deviatoric stress tensor  $J_2$  in sublayers with greater Young modulus: a)  $h = 0.4, f = 0$ ; b)  $h = 0.8, f = 0$ ; c)  $h = 0.4, f = 0.25$ ; d)  $h = 0.8, f = 0.25$

## 5. CONCLUSIONS

Calculations show that:

- Distribution of the first principal stress  $\sigma_1$  in layers with greater Young modulus is similar to that in a homogeneous coating when  $E_{coating} > E_{substrate}$  (Kulchytsky-Zhyhailo and Rogowski, 2007, 2010; Schwarzer, 2000). Values of tensile stresses (if exist) on the coating-substrate interface are lower than in a homogeneous coating with the same Young modulus.
- Distributions of the stress tensor components which experience a jump on the interfaces are different in layers with greater Young modulus from distributions in layers with smaller Young modulus.

## REFERENCES

1. **Bragallini G.M., Cavatorta M.P., Sainsot P.** (2003), Coated Contacts: a Strain Approach, *Tribology International*, Vol. 36, 935-941.
2. **Elliot D.A.** (1949), Three-Dimensional Stress Distributions in Aeolotropic Hexagonal Crystals, *Cambridge Phil. Society*, Vol. 44, 522-533.
3. **Guler M.A., Erdogan F.** (2007), The frictional Sliding Contact Problems of rigid parabolic and cylindrical stamps on Graded Coatings, *Int. J. Mech. Sci.*, Vol. 49, 161-182.
4. **Kaczyński A.** (1994), Three-Dimensional Thermoelastic Problems of Interface Crack in Periodic Two-Layered Composites, *Engineering Fracture Mechanics*, Vol. 48, 783-800.
5. **Kołodziejczyk W., Kulchytsky-Zhyhailo R.** (2013), Stress Distribution in Two-Layered Half-Space with Periodical Structure Caused by Hertz Pressure, *J. Theor. Appl. Mech.*, Vol. 51, 741-750.
6. **Kulchytsky-Zhyhailo R.** (2011), Two-Layered Periodic Coated Elastic Half-Space under Hertz's Pressure, *Materials Science*, Vol. 47, No. 4, 527-534.
7. **Kulchytsky-Zhyhailo R., Bajkowski A.** (2011), Elastic Half Space with Inhomogeneous Coating under the Action of Tangential Forces, *Materials Science*, Vol. 46, 735-746.
8. **Kulchytsky-Zhyhailo R., Kołodziejczyk V.** (2005), Stress Field Caused by Hertz's Pressure in non-uniform half-plane with Periodic Structure, *J. Friction and Wear*, Vol. 26, No. 4, 358-366.
9. **Kulchytsky-Zhyhailo R., Rogowski G.** (2007), Stresses of Hard Coating under Sliding Contact, *J. Theor. Appl. Mech.*, Vol. 45, 753-771.
10. **Kulchytsky-Zhyhailo R., Rogowski G.** (2010), Stresses in hard coating due to a rigid spherical indenter on a Layered Elastic Half-Space, *Tribology Int.*, Vol. 43, No. 9, 1592-1601.
11. **Liu T.J., Wang Y.S., Zhang C.** (2008), Axisymmetric Frictionless Contact of Functionally Graded Materials, *Archive of Appl. Mech.*, Vol. 78, 267-282.
12. **Matysiak S.J., Woźniak Cz.** (1987), Micromorphic Effects in Modelling of Periodic Multilayered Elastic Composites, *Int. J. Engng. Sci.*, Vol. 25, 549-559.
13. **Schwarzer N.** (2000), Coating Design Due to Analytical Modelling of Mechanical Contact Problems of Multilayer Systems, *Surf. Coat. Technol.*, Vol. 133-134, 397-402.
14. **Voevodin A.A., larve E.V., Ragland W., Zabinski J.S., Donaldson S.** (2001), Stress analyses and In-Situ Fracture Observation of Wear Protective Multilayer Coatings in Contact Loading, *Surf. Coat. Technol.*, Vol. 148, 38-45.
15. **Woźniak Cz.** (1987), A nonstandard method of Modelling Thermoelastic Composites, *Int. J. Engng. Sci.*, Vol. 25, 483-499.

The investigations described in this paper are a part of the research projects S/WM/1/2013 and S/WM/1/2012 realized at Białystok University of Technology.

## KALMAN FILTER REALIZATION FOR ORIENTATION AND POSITION ESTIMATION ON DEDICATED PROCESSOR

Slawomir ROMANIUK\*, Zdzislaw GOSIEWSKI\*

\*Department of Automatic Control and Robotics, Faculty of Mechanical Engineering, Bialystok University of Technology, ul. Wiejska 45C, 15-351 Bialystok, Poland

[s.romaniuk@doktoranci.pb.edu.pl](mailto:s.romaniuk@doktoranci.pb.edu.pl), [z.gosiewski@pb.edu.pl](mailto:z.gosiewski@pb.edu.pl)

**Abstract:** This paper presents Kalman filter design which has been programmed and evaluated in dedicated STM32 platform. The main aim of the work performed was to achieve proper estimation of attitude and position signals which could be further used in unmanned aerial vehicle autopilots. Inertial measurement unit and GPS receiver have been used as measurement devices in order to achieve needed raw sensor data. Results of Kalman filter estimation were recorded for signals measurements and compared with raw data. Position actualization frequency was increased from 1 Hz which is characteristic to GPS receivers, to values close to 50 Hz. Furthermore it is shown how Kalman filter deals with GPS accuracy decreases and magnetometer measurement noise.

**Key words:** INS, GPS, Kalman Filter

### 1. INTRODUCTION

Cheap measurement devices such as accelerometers, gyroscopes, or magnetometers are widely used in various navigations systems of ground and aerial vehicles in order to minimize the costs of measurement systems (Ahn and Won, 2009; Grewal and Andrews, 2008). In addition, they constitute one of the most important parts of unmanned aerial vehicles autopilots, as their reliability is crucial to control systems performance (Ali and Ullag Baig Mirza, 2010). With better knowledge about current position and orientation of unmanned aerial vehicle it is possible to perform more complicated, more precise and faster maneuvers (Chen and Xu, 2010). Therefore, the improvement of the quality of measurement systems is at almost all times desirable (Wagner and Kasties, 2004). Application of higher grade measurement devices can be far too expensive (Shojaei and Mohammad Shari, 2011), while using the dose computation power does not increase the costs of the whole system (Haid and Breitenbach, 2004). Kalman filter is a practical computational algorithm which may be used as a tool for estimating unknown state vectors basing on noisy measurements (Simon, 2001).

Inertial measurement unit (IMU) senses three accelerations and three angular rates for different vehicles degrees of freedom (Titterton and Weston, 1997). Along with adequate computational algorithm IMU creates inertial navigation system (INS), which, however, gives biased and noisy position data, while assuring relatively high short term accuracy (Wendel et al., 2001; Sun et al., 2013). On the other hand, GPS receiver provides relatively less accurate position data, but it is not affected by the time drift. Hence, both of the aforementioned devices are mutually complementing one another (Hongwei et al., 2006). It is possible to integrate both sources of data in order to gain advantages and reduce or even eliminate disadvantages of separated measurements by means of Kalman filter (Mohamed and Schwarz, 1999). Apart from position, orientation is also determined by the use of three

different data sources which are accelerometer, magnetometer characterized by long term accuracy and gyroscope characterized by short term accuracy. In this case, orientation may be estimated using Kalman filtering as well.

The STM32 platform has been used in order to minimize delay connected with computational effort required to compute matrices (Franca Junior and Morgado, 2010). Furthermore, it provided enough outputs and inputs to connect it with Inertial Measurement Unit, GPS receiver and computer.

### 2. KALMAN FILTER

Standard Kalman filter is a linear estimator, that has the ability to minimize error variance. Its equations are characterized by recursive type of computation, which may be relatively easily realized on a microprocessor. Kalman filter current output depends on current state and current inputs (Brookner, 1998). The filter is basing on linear systems equations:

$$x_{k+1} = Ax_k + Bu_k + w_k \quad (1)$$

$$y_k = Hx_k + z_k \quad (2)$$

where  $A$ ,  $B$ , and  $H$  are state, input and measurement matrices respectively,  $x$  is state of the system,  $u$  is known input to the system,  $y$  is the measured output,  $w$  is a process noise and  $z$  is a measurement noise. Vector  $x$  contains present state of the system, which can be estimated from given measurements in vector  $y$  and given input to the system determined in vector  $u$ . However, we cannot entirely rely on information from  $y$  to obtain  $x$  vector, because  $y$  is noised (Bar-Shalom et al., 2001). Depending on the system, all of these quantities can be vectors (elements including more than one element).

Kalman filter assumes that process noise and measurement noise are not correlated with each other, whereas their average values are zero. In order to fulfill the aforementioned assumptions,

covariance matrices for process noise ( $Q$ ), and measurement noise ( $R$ ) are given by formulas (3) and (4).

$$Q = E(w_k w_k^T) \quad (3)$$

$$R = E(z_k z_k^T) \quad (4)$$

Kalman filter algorithm can be split up to two different stages called respectively time update and measurement update. During the first stage, values of vector  $x$  (5) are being predicted and covariance matrix  $P_k^-$  (6) is being computed.

$$x_k^- = Ax_{k-1} + Bu_{k-1} \quad (5)$$

$$P_k^- = AP_{k-1}A^T + Q \quad (6)$$

where  $x_k^-$  is the predicted state estimation at actual time step,  $P_k^-$  is the predicted estimated covariance matrix,  $P_{k-1}$  is the updated estimated covariance at previous time step and  $x_{k-1}$  is updated state estimation from previous time step.

Final (updated) values are determined during the second stage of Kalman filter. The Kalman gains matrix is computed from the equation given as (7). The Riccati and Kalman filter equations are given by:

$$K_k = P_k^- H^T (HP_k^- H^T + R)^{-1} \quad (7)$$

$$x_k = x_k^- + K_k(y_k - Hx_k^-) \quad (8)$$

$$P_k = (I - K_k H)P_k^- \quad (9)$$

where  $K_k$  is the Kalman gain at actual time step,  $x_k$  is the updated state estimation vector at actual time step,  $y_k$  is the measurement vector at actual time step,  $P_k$  is the updated estimated covariance matrix at actual time step, and  $I$  is the identity matrix (Simon, 2001).

## 2.1. Orientation

In order to make Kalman filter applicable to parameters estimation of specific processes, knowledge of dynamic system description is needed. In the case of orientation evaluation, which dynamic system is given by equations (10) and (11) if we denote  $\alpha$  as angle,  $\omega$  as angular rate,  $q_b$  as gyroscope bias and  $T$  as sample period.

$$\alpha_k = \alpha_{k-1} + (\omega_k - q_{bk-1})T \quad (10)$$

$$q_{bk} = q_{bk-1} \quad (11)$$

Gyroscope information can be distorted by bias error, which hence should be, and is estimated in state vector and included in aforementioned dynamic system equation, giving the algorithm the possibility of correcting angular velocity value.

Taking (12) as the state vector, matrices A, B, and H are given respectively by (13), (14) and (15).

$$x = \begin{bmatrix} \alpha \\ q_b \end{bmatrix} \quad (12)$$

$$A = \begin{bmatrix} 1 & -T \\ 0 & 1 \end{bmatrix} \quad (13)$$

$$B = \begin{bmatrix} T \\ 0 \end{bmatrix} \quad (14)$$

$$H = \begin{bmatrix} 1 & 0 \end{bmatrix} \quad (15)$$

Input and measurements vectors are defined in (16) and (17) equations respectively. Input to the filter is the angular rate while the measurement is the angle.

$$u = [\omega] \quad (16)$$

$$y = [\alpha] \quad (17)$$

Matrix Q representing system noise covariance and R which is the measurement noise covariance matrix are as follows:

$$Q = \begin{bmatrix} T^2 \sigma_\alpha^2 & 0 \\ 0 & \sigma_\alpha^2 \end{bmatrix} \quad (18)$$

$$R = [\sigma_\omega^2] \quad (19)$$

where  $\sigma_\alpha$  represents orientation measurement noise and  $\sigma_\omega$  represents angular rate measurement noise (Simon, 2001).

The use of three consecutive Kalman filter implementations for pitch, roll and yaw accordingly is adopted in order to reduce matrices size and therefore decrease computational requirements.

## 2.2. Position

In the case of position filtration, available information corresponds to current position and its second derivative – acceleration. Taking S as travelled distance, v as velocity, a as acceleration,  $a_b$  as accelerometer bias and T as sample period, dynamic system used in the algorithm of Kalman filter, is described by three equations. The first equation (20) describes the way in which the position is being calculated. It uses values of previous position, previous velocity, current acceleration and previous accelerometer bias. The last mentioned value may, depending on the algorithm estimation accuracy, virtually precisely reduce related measurement error. The second equation (21) is used to compute velocity, having its previous value, an acceleration as well as an acceleration bias. The last equation (22) assigns value of accelerometer bias from previous time step to the current one.

$$S_k = S_{k-1} + v_{k-1}T + \frac{(a_k - a_{bk-1})T^2}{2} \quad (20)$$

$$v_k = v_{k-1} + (a_k - a_{bk-1})T \quad (21)$$

$$a_{bk} = a_{bk-1} \quad (22)$$

The equations listed above may be represented in state space form, where three state variables are included in the state vector (23).

$$x = \begin{bmatrix} S \\ v \\ a_b \end{bmatrix} \quad (23)$$

Input and measurements vectors are defined in (24) and (25) equations respectively. Input to the filter is the acceleration while the measurement is the position.

$$u = [a] \quad (24)$$

$$y = [S] \quad (25)$$

Matrices A, B and H describing the dynamic system are given in the following form:

$$A = \begin{bmatrix} 1 & dt & -\frac{T^2}{2} \\ 0 & 1 & -T \\ 0 & 0 & 1 \end{bmatrix} \quad (26)$$

$$B = \begin{bmatrix} \frac{T^2}{2} \\ T \\ 0 \end{bmatrix} \quad (27)$$

$$H = [1 \ 0 \ 0] \quad (28)$$

Representations of system noise covariance and measurement noise covariance are adopted by Q (29) and R (30) matrices respectively.

$$Q = \begin{bmatrix} \frac{T^4}{4}\sigma_p^2 & \frac{T^3}{2}\sigma_p^2 & 0 \\ \frac{T^3}{2}\sigma_p^2 & T^2\sigma_p^2 & 0 \\ 0 & 0 & 0 \end{bmatrix} \quad (29)$$

$$R = [\sigma_a] \quad (30)$$

where  $\sigma_p$  denotes position measurement noise and  $\sigma_a$  denotes acceleration measurement noise (Simon, 2001).

### 3. COMPLEMENTARY EQUATIONS

#### 3.1. Rotation Matrix

Rotation matrix is used in order to transform values of measurements given in one frame to those expressed in a different one. Aforementioned matrix from the body frame to the navigation frame is given by:

$$C_b^n = R_z(\psi)R_y(\psi)R_x(\phi) \quad (31)$$

where:

$$R_x(\psi) = \begin{pmatrix} \cos\psi & -\sin\psi & 0 \\ \sin\psi & \cos\psi & 0 \\ 0 & 0 & 1 \end{pmatrix} \quad (32)$$

$$R_y(\theta) = \begin{pmatrix} \cos\theta & 0 & \sin\theta \\ 0 & 1 & 0 \\ -\sin\theta & 0 & \cos\theta \end{pmatrix} \quad (33)$$

$$R_z(\phi) = \begin{pmatrix} 1 & 0 & 0 \\ 0 & \cos\phi & -\sin\phi \\ 0 & \sin\phi & \cos\phi \end{pmatrix} \quad (34)$$

By substituting (32), (33) and (34) to (31):

$$C_b^n = \begin{bmatrix} c\theta c\psi & -c\phi s\psi + s\phi s\theta c\psi & s\phi s\psi + c\phi s\theta c\psi \\ c\theta s\psi & c\phi c\psi + s\phi s\theta s\psi & -s\phi c\psi + c\phi s\theta s\psi \\ -s\theta & s\phi c\theta & c\phi c\theta \end{bmatrix} \quad (35)$$

where  $c$  represents cosine,  $s$  represents sine,  $\theta$  is a pitch angle,  $\phi$  is a roll angle and  $\psi$  is a yaw angle (Titterton and Weston, 1997).

### 3.2. Pitch and Roll Angles Derivation

By utilizing accelerometer data it is possible to compute coarse values of pitch (37) and roll (36) angles, which may further be used in filtration algorithm.

$$\xi = -\tan^{-1}\left(\frac{a_y^b}{a_z^b}\right) \quad (36)$$

$$\eta = \tan^{-1}\left(\frac{a_x^b}{a_z^b}\right) \quad (37)$$

where  $\xi$  is the derived roll angle,  $\eta$  is the derived pitch angle,  $a_x^b$  is the raw measured acceleration value in  $x$  axis of the body frame,  $a_y^b$  is the raw measured acceleration value in  $y$  axis of the body frame,  $a_z^b$  is the raw measured acceleration value in  $z$  axis of the body frame.

### 4. GPS ERRORS

Using GPS measurements may give rise to several error sources, such as: ionospheric error, tropospheric error, orbital error, satellite clock error, receiver clock error, multipath etc. Ionospheric and tropospheric errors are caused by slower signal propagation in comparison with vacuum speed of light. Satellite clock error and receiver clock error are strictly connected to inaccuracies of onboard clock, causing the offset of the satellite clock and the receiver clock accordingly with respect to the GPS-time. Orbital error is the error between true and estimated satellite positions. Multipath occurs when the signal is being reflected on the way from satellite to receiver instead of going straightforward (Romaniuk, 2013). Possible influence of those types of errors on the GPS measurement is presented in Tab. 1.

Tab. 1. Error influence (Romaniuk, 2013)

Error type	Error value
Ionospheric error	2-20m
Tropospheric error	0.5-5m
Orbital error	0-3m
Satellite clock error	0-3m
Receiver clock error	0-10m
Multipath	0-5m
Noise (others)	0.25-0.5m

### 5. EXPERIMENTAL SETUP

Mobile research platform has been designed on the base of STM32F103 microcontroller. Chosen element is characterized by relatively low cost, numerous communication peripheries and adequate running frequency. Moreover, it can be programmed in C/C++ programming language and it runs at 72 MHz frequency (<http://www.kamami.pl/>). Measurements have been taken by means of Razor 9 DOF inertial measurement unit (IMU) and GPS receiver with MTK MT3339 chipset.

Single axis gyroscope (LY530ALH), two axis gyroscope (LPR530AL), triple axis accelerometer (ADXL335), triple axis magnetometer (HMC5843) are the components of the used IMU. Linear accelerations and angular rates measured in aforemen-

tioned inertial system are transmitted by means of UART interface. Razor 9 DOF runs at 50Hz sampling rate. Sensors specifications of gyroscopes (Tab. 2.), accelerometer (Tab. 3.) and magnetometer (Tab. 4.) are relatively low. Since there are two devices used to measure angular rate, two columns for each of them are included in Tab. 1. In the case of accelerometer device, it was needed to split X, Y and Z axis in order to fully describe the aforementioned sensor.

GPS receiver is using UART interface in order to transmit NMEA packets to STM32F103 microcontroller. Those packets include different types of information regarding not solely position, but satellites status, time and different parameters as well (<http://www.gpsinformation.org/dale/nmea.htm>). In the presented application, configuration of GPS receiver defined actualization frequency of position measurement at 1 Hz (one time per second).

**Tab. 2.** Gyroscopes specifications (<https://www.sparkfun.com/>)

Parameter	LY530ALH	LPR530AL
Measurement range [°/s]	300	300
Sensitivity [mV/°/s]	3.33	3.33
Nonlinearity [% FS]	±1	±1
Bandwidth [Hz]	140	140
Rate noise density [°/s/√Hz]	0.035	0.035

**Tab. 3.** Accelerometer specifications (<https://www.sparkfun.com/>)

Parameter	ADXL335
Measurement range X, Y, Z [g]	±3.6
Sensitivity X, Y, Z [mV/g]	300
Nonlinearity X, Y, Z [%]	±0.3
Bandwidth X, Y [Hz]	1600
Bandwidth Z [Hz]	550
Noise Density X, Y [μg/√Hz]	150
Noise Density Z [μg/√Hz]	300

**Tab. 4.** Magnetometer specifications (<https://www.sparkfun.com/>)

Parameter	HMC5843
Field range [gauss]	±4
Linearity [±% FS]	<0.1
Bandwidth [kHz]	10
Resolution [milli – gauss]	7
Signal-to noise ratio [dB]	>70

Employed GPS receiver has different configurable values of actualization frequency, however the lowest one rated at 1Hz has been used in order to have better comparison of position interpolation. Constraints of maximum altitude, velocity and acceleration values are defined for ordinary GPS receivers which may be utilized in civil area, in order to prevent military applications such as cruise missile systems (Pace, 1996; Rush, 2000; <http://www.armscontrol.org/documents/mtrc>). Characteristics of used GPS receiver are presented in Tab. 5., which includes most significant ones such as position accuracy, velocity accuracy, actualization frequency and aforementioned civilian GPS receivers limitations.

**Tab. 5.** GPS receiver specifications (<http://www.aliexpress.com/>)

Parameter	MTK MT3339
Receiver	L1 frequency, C/A code, 66 channels
GPS position accuracy	<3.0 m 50% CEP
GPS velocity accuracy [m/s]	0.1
Actualization frequency [Hz]	1-10
Sensitivity [dBm]	-165
Maximum altitude [m]	18 000
Maximum velocity [m/s]	515
Maximum acceleration [g]	4

The first step needed to estimate values of orientation angles is to prepare data acquired from accelerometer, gyroscope and magnetometer. The aforesaid data preparation involves digitalization, transformation and range adjustment. Subsequently, acquired data is evaluated in Kalman filter, where estimated values of pitch, roll and yaw angles come from. The process mentioned above can be seen in Fig. 1. Measured values from gyroscope are used during the time update stage of Kalman filter algorithm and are entered in the u vector. Moreover, the evaluated angles, basing on the data from accelerometer and magnetometer are used in the measurement update stage, and are inputted to the algorithm in the y vector. The angles derived from accelerometer and magnetometer data are used to verify the data from the time update stage, and to make sufficient corrections if necessary.

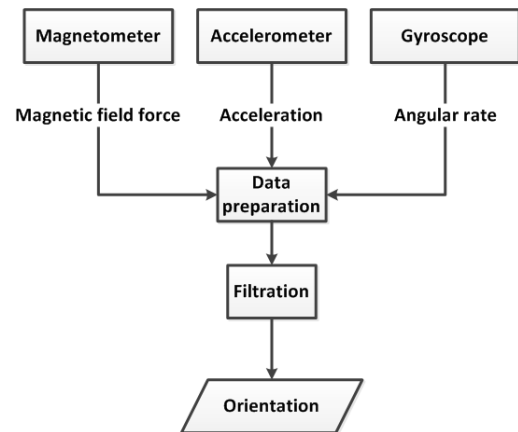


**Fig. 1.** Information flow for orientation estimation (Romaniuk, 2013)

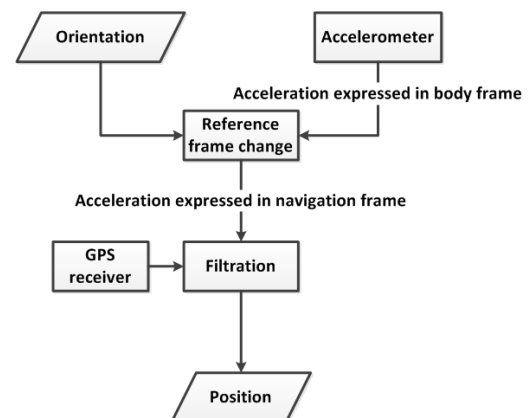


**Fig. 2.** Information flow for position estimation (Romaniuk, 2013)

Position estimation scheme (Fig. 2), on the other hand, is somewhat different. While acceleration and GPS position are given in various units, it is necessary to transform one into another or vice versa. Furthermore, values from inertial measurement unit and GPS receiver are given in different reference frames, which has to be adjusted by means of adequate rotation matrix (35). Obviously, it is needed to have attitude information before doing such transformations. Hence, estimation of pitch, roll and yaw values is done first, before computing position values. Subsequently calculated information of acceleration in navigation frame and GPS data is used to estimate position by Kalman filter. Information that comes from inertial measurement unit is used during the time update and is entered as  $u$  vector, while the data from GPS, inputted in  $y$  vector are used during the measurement update of Kalman filter algorithm. GPS data are used for comparison with the values achieved during the time update and optionally to correct them.

All the data processing related to the Kalman filtration algorithm has been performed on STM32 microcontroller. Calculations were performed on matrixes, hence it was needed to implement functions for matrix operations such as addition, subtraction, multiplication, and inversion. Kalman filter algorithm has been running on 50 Hz rate, which was the same as the actualization frequency of inertial measurement unit. Utilizing USB HID communication availability, calculated output has been saved on the laptop, where results were processed.

Research has been performed on the open terrain, characterized by relatively small amount of physical obstacles, thus providing good GPS satellites visibility. Starting point of the test route is covering the ending one. Data have been recorded during the movement along the specified test route, however because of the time needed to get GPS position fix, it has been recorded for longer term than alone run lasted.

## 6. RESULTS

When performing many tests on the same route, it was observed that GPS information had many drawbacks. There were unexpected satellite signal losses causing high accuracy deterioration, which was not necessarily induced by physical obstacles. Furthermore, used GPS receiver seemed to have needed relatively long time in order to start and get the first position fix.

Some signal losses immunity is achieved by using Kalman filter which integrates data from GPS device and the inertial measurement unit. In the case where the rapid position change occurs on the GPS receiver outage, the corresponding change on the output of Kalman filter will not be similarly fast if the inertial measurement unit data do not coincide with GPS change. On the other hand, this behavior depends on the reliability of IMU. Poor quality of inertial measurement unit devices greatly reduces capabilities of position estimation when shortage of GPS signal occurs.

While conducting the orientation algorithm performance evaluation, comparison between the unfiltered and filtered data has been made, where the former represents angles derived from raw magnetometer data and the latter one is the output of the Kalman filter. On the other hand, in the case of position estimation algorithm, first data set refers to raw, unaided, unfiltered GPS data, while the other one shows performance of the Kalman filter algorithm.

As illustrated in Fig. 3, usage of Kalman filter gave relatively high noise reduction in comparison with raw IMU data, what

is shown by unstable measurement trend. Furthermore, what is also important, relatively high output dynamics are preserved. This is evidenced in high dynamic movements shown at 10-13 s, 14-18 s and 19-27 s for pitch, roll and yaw angles respectively.

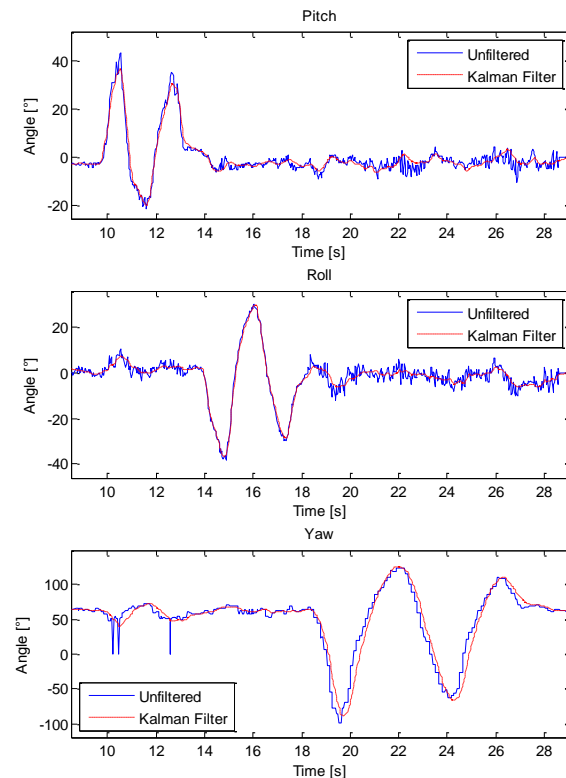


Fig. 3. Kalman filter performance for orientation estimation (Romaniuk, 2013)

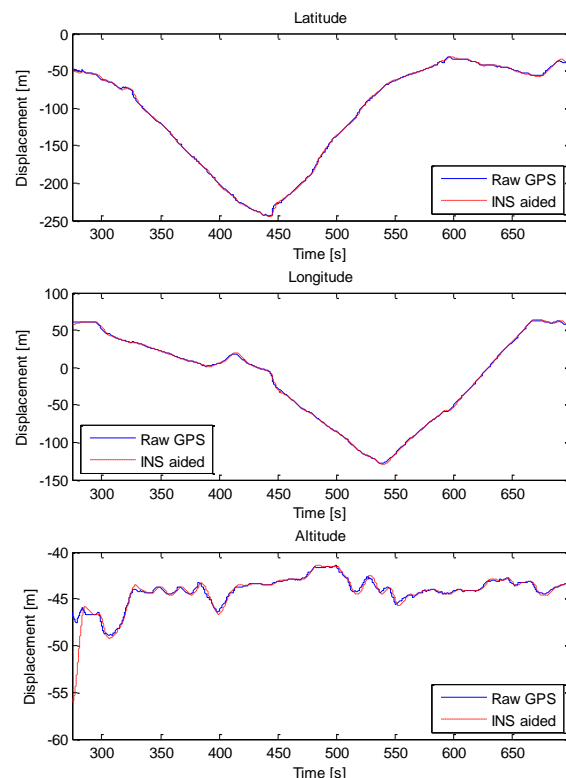


Fig. 4. Results of GPS/INS systems integration (Romaniuk, 2013)

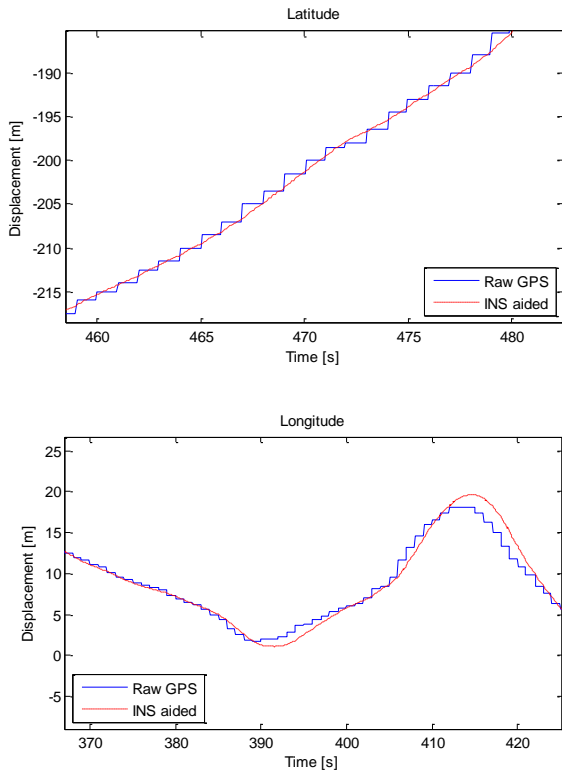


Fig. 5. Actualization frequency improvement (Romaniuk, 2013)

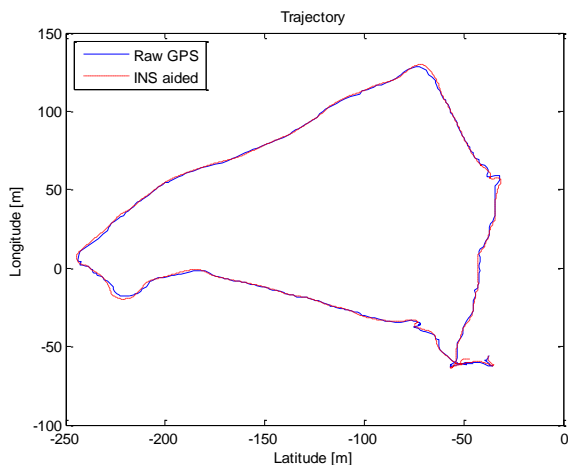


Fig. 6. Testing route noted by GPS receiver and estimated with GPS/INS system (Romaniuk, 2013)

According to results from Fig. 4, raw GPS and INS aided information are virtually fully covering each other. This is caused by relatively low quality of IMU devices measurements, and thus giving more confidence by Kalman filter to GPS values. However Fig. 5 shows that proposed solution provides higher position actualization frequency, and information interpolation between two specified data at different time steps.

Moreover, at the trajectory plot (Fig. 6), smoother position transition at curves is achieved by Kalman filter in comparison with GPS measurements. This behavior is convenient when measurement system is operating together with control system.

## 7. CONCLUSIONS

A solution of INS/GPS systems integration in real time has been presented in the following paper. Orientation filtering algorithm is characterized by rewarding measurement noise reduction and resolution increase, which can be seen on pitch, roll and yaw graphs. On the other hand in the case of the position integration algorithm, the main advantage is about achieving higher update frequency rated at about 50Hz, which in comparison with 1Hz, characteristic to used GPS receiver, is great enhancement. Unfortunately, the results show rather poor Kalman filter altitude estimation. This is principally caused by low GPS accuracy in this area, and should be further improved by using better source for measuring height. Further increasing the frequency, Kalman filter algorithm is running at, would decrease the time step length (Lee and Salcic, 1997).

It is possible to improve quality of measurement system by introducing model which would estimate a larger number of sensor errors (Han and Wang, 2012). Knowledge of specified sensor errors helps in accurate position estimation in case of loss of GPS signal. It is caused by the fact that, through the application of precise corrections, relatively accurate determination of measurement signals is becoming possible. As the instance of the system that introduces such model, deeply integrated INS/GPS system may be given (Luo et al., 2012).

Further improvement is possible by adopting higher grade of inertial measurement unit and/or GPS receiver. Sensors characterized by reliable specifications are more expensive, and, as a result, not always possible to use in low cost systems. Introducing more measurement devices for measuring the same quantity of measurement parameter is another way of navigation system quality enhancement (Caron et al. 2006). Proposed solution may be further studied in order to improve overall performance of the measurement system (Gosiewski and Ortyl, 1999; Gibbs, 2011; Ning and Fang, 2007).

## REFERENCES

1. **Ahn H.-S., Won C.-H.** (2009), DGPS/IMU Integration-Based Geolocation System: Airborne Experimental Test Results, *Aerospace Science and Technology*, 13, 316-324.
2. **Ali J., Ullah Baig Mirza M. R.** (2010), Performance Comparison among Some Nonlinear Filters for a Low Cost SINS/GPS Integrated Solution, *Nonlinear Dynamics*, 61, 491-502.
3. **Bar-Shalom Y., Rong Li X., Kirubarajan T.** (2001), *Estimation with Applications to Tracking and Navigation*, John Wiley & Sons.
4. **Brookner E.** (1998), *Tracking and Kalman Filtering Made Easy*, John Wiley & Sons.
5. **Caron F., Duflos E., Pomorski D., Vanheegho P.** (2006), GPS/IMU Data Fusion using Multisensor Kalman Filtering: Introduction of Contextual Aspects, *Information Fusion*, 7, 221-230.
6. **Chen T., Xu S.** (2010), Double Line-of-sight Measuring Relative Navigation for Spacecraft Autonomous Rendezvous, *Acta Astronautica*, 67, 122-134.
7. **Franca Junior J. A., Morgado J. A.** (2010), Real Time Implementation of a Low-Cost INS/GPS System using xPC Target, *Journal of Aerospace Engineering, Sciences and Applications*, Vol. 2, No. 3
8. **Gibbs B. P.** (2011), *Advanced Kalman Filtering, Least-Squares and Modelling*, John Wiley & Sons.
9. **Gosiewski Z., Ortyl A.** (1999), *Algorithms of Inertial Guidance System and the Position of the Object of Spatial Motion* (in Polish), Scientific Publishers Division of the Institute of Aviation system.

10. **Grewal M. S., Andrews A. P.** (2008), *Kalman Filtering: Theory and Practice Using MATLAB*, John Wiley & Sons.
11. **Haid M., Breitenbach J.** (2004), Low Cost Inertial Orientation Tracking with Kalman Filter, *Applied Mathematics and Computation*, 153, 567-575.
12. **Han S., Wang J.** (2012), Integrated GPS/INS Navigation System with Dual-Rate Kalman Filter, *GPS Solutions*, 16, 389-404.
13. **Hongwei B., Zhihua J., Tian Wei F.** (2006), IAE-adaptive Kalman Filter for INS/GPS Integrated Navigation System, *Journal of Systems Engineering and Electronics*, Vol. 17, No. 3, 502-508.
14. **Lee C. R., Salcic Z.** (1997), High-performance FPGA-Based Implementation of Kalman Filter, *Microprocessors and Microsystems*, 21, 257-265.
15. **Luo Y., Wu W., He X.** (2012), Double-filter Model with Modified Kalman Filter for Baseband Signal Pre-processing with Application to Ultra Tight GPS/INS Integration, *GPS Solutions*, 16, 463-476.
16. **Mohamed A. H., Schwarz K. P.** (1999), Adaptive Kalman Filtering for INS/GPS, *Journal of Geodesy*, 73, 193-203.
17. **Ning X., Fang J.** (2007), An Autonomous Celestial Navigation Method for LEO Satellite Based on Unscented Kalman filter and Information Fusion, *Aerospace Science and Technology*, 11, 222-228.
18. **Pace S.** (1996), The Global Positioning System: Policy Issues for an Information Technology, *Space Policy*, 12, 265-275.
19. **Romaniuk S.** (2013), *Autopilot Measurement Systems Research*, Master Thesis, Bialystok University of Technology.
20. **Rush J.** (2000), Current Issues in the Use of the Global Positioning System Aboard Satellites, *Acta Astronautica*, 47, 377-387.
21. **Shojaei K., Mohammad Shahri A.** (2011), Experimental Study of Iterated Kalman Filters for Simultaneous Localization and Mapping of Autonomous Mobile Robots, *Journal of Intelligent and Robotic Systems*, 63, 575-594.
22. **Simon D.** (2001), Kalman Filtering, *Embedded Systems Programming*, June 2001, 72-79.
23. **Sun W., Wang D., Xu L., Xu L.** (2013), MEMS-Based Rotary Strapdown Inertial Navigation System, *Measurement*, 46, 2585-2596
24. **Titterton D. H., Weston J. L.** (1997), Strapdown Inertial Navigation Technology, *Institution of Electrical Engineers*.
25. **Wagner J. F., Kasties G.** (2004), Applying the Principle of Integrated Navigation Systems to Estimating the Motion of Large Vehicles, *Aerospace Science and Technology*, 8, 155-166.
26. **Wendel J., Schlaile C., Trommer G. F.** (2001), Direct Kalman Filtering of GPS/INS for Aerospace Applications, *International Symposium on Kinematic Systems in Geodesy, Geomatics and Navigation (KIS2001)*, Canada.
27. <http://www.aliexpress.com/>
28. <http://www.armscontrol.org/documents/mtr>
29. <http://www.gpsinformation.org/dale/nmea.htm>
30. <http://www.kamami.pl/>
31. <https://www.sparkfun.com/>

# THE INFLUENCE OF CHANGES IN THE GEOMETRY OF THE TOOTH SURFACE OF THE PINION BEVEL GEAR ON THE KINEMATIC ACCURACY OF PAIR MESH

Mieczysław PŁOCICA\*, Jadwiga PISULA\*

\*Department of Mechanical Design, Rzeszow University of Technology, Al. Powstańców Warszawy 12, 35-959 Rzeszów, Poland

[mplocica@prz.edu.pl](mailto:mplocica@prz.edu.pl), [jpisula@prz.edu.pl](mailto:jpisula@prz.edu.pl)

**Abstract:** The paper describes the possibilities of bevel gears kinematics design on the basis of the motion graph and improving modifications to cut the pinion teeth flanks. The result is the ability to increase the accuracy of the kinematic transmission. The issue of changing the geometry of the pinion gear is considered in respect of a gear intended for the use in aviation, which requires the cooperation of high quality meshing. The basic geometric features that have been modified include the profile angle, the angle of tooth line, crowning transverse and longitudinal and lateral surface twist angle of the tooth. The modification of each of the selected geometrical parameters has had a different effect on the chart of transmission. It has been shown that the effect of the intended changes in the geometry of the pinion may reduce the deviation of motion delays gear and an improve the gear transmission chart.

**Key words:** Bevel Gears, Gleason, Kinematic Accuracy

## 1. INTRODUCTION

A proper design of each toothed gear is practically verified by its operation. In the case of bevel gears the most important quality indicators of meshing are the total contact pattern of mating and the motion graph. They are evaluated and corrected in the virtual model while determining the conditions of gear members design by making suitable modifications to the teeth flank surface of the pinion (Simon, 2008; Shih and Fong, 2008; Zhang and Wang, 2012). The selection of the geometry of the surface to the cut surface of the flank of a tooth gear can affect the shape and course of mating and the course of contact of teeth pair construction. The operational effect of the correct design and properly cut mating surfaces of teeth is the meeting of the expectations of the constructor in the capacity and nature of the work gear (De Vaujany et al., 2008). The course of the contact path and the area of the contact pattern of mating define the ability of the gear to carry loads, its low noise and sensitivity to assembly errors. A motion graph directly indicates the kinematic accuracy of the designed meshing.

## 2. MODEL OF BEVEL GEAR PAIR

The model of constructional bevel gear to mesh analysis is described in Marciniec (2003). It is a set of coordinate systems shown in Fig. 1. The system  $S_f$  is rigidly connected to the body of the gear unit, so that its axis  $Z_f$  coincides with the axis of rotation of the pinion  $Z_1$ . The axis  $X_f$  should intersect the axis of rotation of the gear  $Z_2$  at the point  $O_2$ , which – together with the point  $O_f$  – designates a section equal to the shortest distance between the axes ( $E$ ), where  $E$  stands for the bevel gear assembly error, whose axes theoretically intersect at an angle  $\Sigma$ . The starting position for the systems  $S_1$  and  $S_2$ , which are rigidly connected respectively with the pinion and the gear is a position in which the

axes  $X_1$  and  $X_2$  have opposite directions and are aligned with the axis  $X_f$ . The system  $S_d$  is an auxiliary system facilitates the determination of the position of the system  $S_2$ .

When meshing, the current position of the pinion and gear angles are defined by the angles of their rotations, that is  $\varphi_1$  and  $\varphi_2$ . The values  $\varphi_1^{(0)}$  and  $\varphi_2^{(0)}$  of these angles designate a position which ensures contact of the tooth surfaces  $\Sigma_1$  and  $\Sigma_2$  at the center point  $M$ , in which the position  $u_{12}$  reaches the nominal value calculated with the following formula:

$$u_{21} = \frac{\omega_2}{\omega_1} = \frac{z_1}{z_2} \quad (1)$$

where:  $\omega_1, \omega_2$  – angular velocity of pinion and gear respectively,  $z_1, z_2$  – the number of teeth of pinion and gear.

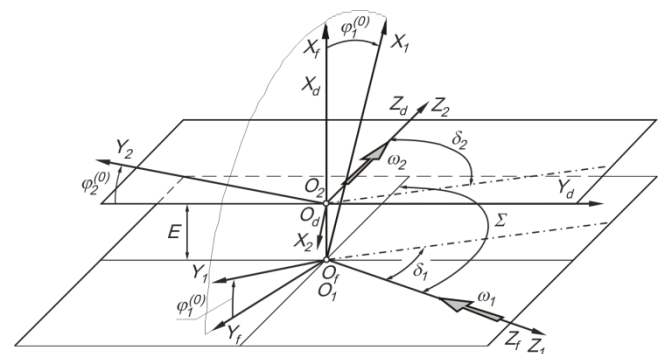


Fig. 1. Coordinate systems of bevel gear model

## 3. ISSUES ON MOTION GRAPH

The motion graph shows the relation between gear motion and the driving pinion moving at constant angular velocity (Litvin and Fuentes, 2004). The relation between the angle of gear rotation  $\varphi_2$  and the pinion rotation angle  $\varphi_1$  is shown in Fig. 2. In the theoretical transmission, where the surfaces of the mating teeth

are coupled linearly and envelope each other as a result of a roll with a constant ratio, the graph will be a straight line. In addition to the theoretical case, it is necessary to assume the ideal rigidity of teeth and the right design and assembly of the gears. Such a transmission transmits the motion at a uniform rate and keeps the constant ratio (Alves et al., 2013). Therefore, the function of the motion transmission in an ideal, theoretical gear is a linear function:

$$\varphi_2 = u_{21} \cdot \varphi_1 \quad (2)$$

Points  $P_p$  and  $P_k$  (Fig. 2) determine the beginning and the end of the teeth pairs contact and  $\gamma_1$  is the angle pitch of the pinion toothing.

$$\gamma_1 = \frac{2\pi}{z_1} \quad (3)$$

Point  $P_p$  is the point of contact of the tooth root of the pinion with the tooth tip of the gear, and  $P_k$  is the point of contact of the pinion tooth tip with the gear tooth root. Knowing the angle  $\gamma_p$  through which the pinion will rotate during the contact tooth it is possible to determine the contact ratio which expresses the average number of teeth in contact.

$$\varepsilon = \frac{\gamma_p}{\gamma_1} \quad (4)$$

$$\Delta\varphi_2 = \varphi_2(\varphi_1) - u_{21}\varphi_1 \quad (5)$$

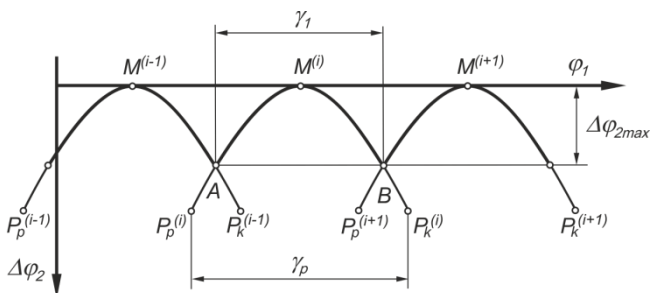


Fig. 2. Motion graph of the bevel gears pair (2)

In practice, neither gear members nor other parts of the machine unit can be made perfectly. Due to the permitted by tolerance changes of their dimensions and geometry in relation to the theoretical form, a modification of the active surface of the pinion teeth is introduced. Its aim is to reduce the sensitivity of the transmission for the errors in the position of the pinion and the gear in the pair. A negative effect of this action is that the gear motion is not uniform and it is only at the point  $M$  that it reaches the assumed value  $u_{21}$ , while in the remaining range it is variable and dependent on the angle of rotation  $u_{21}(\varphi_1)$ . The gear moves with a delay with variable speed of  $\omega_2 = f(\varphi_1)$  (Marciniec, 2003). Deviations of the gear angle rotation in relation to the angle resulting from the assumed constant ratio, calculated with the formula (Pisula and Płocica, 2013), are depicted by the parabola on the motion graph. This graph should have a mild course with no abrupt changes in value, and the value of the maximum deviation in the point of motion transmission should not exceed 10 seconds of arc (Litvin and Fuentes, 2004). Such a shape of the motion graph ensures a fairly uniform gear course with no sudden accelerations and decelerations.

Mating of the gear and pinion of a theoretically perfect geometry, assembled with some deviations in a construction pair,

will be characterized by contact edge, and the graph becomes a so-called “sawtooth wave” (shown in Fig. 3). This situation is unacceptable because it results in a shocking character of the loading transmission and an increased toothing noisiness.

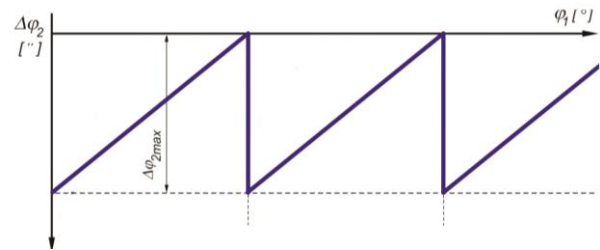


Fig. 3. “Sawtooth wave” motion graph as a result of shocking mesh

In the gear in which the motion has been modified with appropriate parameters, such phenomena do not occur even in the presence of assembly errors. The set modification of the movement of transmission is realized by providing appropriate setting values of the processing machine at the stage of the pinion processing to ensure the desired modification of the active surface of the tooth (Alves et al, 2013; Marciniec, 2003; Wang and Fong, 2005). This requires a change in the geometry of the pinion at the stage of the data preparation for the calculation process.

#### 4. ANALYSIS AND MODIFICATION OF MOTION GRAPH

The issue on modeling of kinematic accuracy of the bevel gear was presented with the example of the pair 17/35 whose geometry is specified in Tab. 1.

Tab. 1. Basic geometrical data of the gear 17/35

Quantity	Designation	Pinion	Gear
Number of teeth	$z$	17	35
Hand of spiral		Left	Right
External transverse module	$m_t$	1.860 mm	
Pressure angle	$\alpha_0$	20°	
Shaft angle	$\Sigma$	90°	
Spiral angle	$\beta$	33°15'	
Mean cone distance	$R$	30.186 mm	
Face width	$b$	12.00 mm	
External whole depth	$H$	3.191mm	3.191mm
Clearance	$c$	0.350 mm	0.350 mm
External height of tooth head	$h_a$	1.837mm	1.004 mm
External height of tooth root	$h_f$	1.354 mm	2.187mm
Pitch angle	$\delta$	25°54'23"	64°5'37"
Dedendum angle	$\theta_f$	0°30'58"	0°50'2"
Addendum angle	$\theta_a$	0°50'2"	0°30'58"

The reference for making changes in the geometry of the flank surface of the pinion is the gear tooth surface, obtained by virtual cutting from the basic machine settings. The motion graph of the basic design pair is shown in Fig. 4. Further modifications to improve the kinematic accuracy are carried out in relation to the basic surface of the pinion (i.e. not to the theoretical surface). The geometry of the tooth flank surface is determined by the following

parameters: deviation of pressure angle  $\alpha$ , deviation of spiral angle  $\beta_1$ , tooth flank surface deviation angle T, profile curvature factor  $B_w$  and lengthwise curvature factor K. The changes of values of each parameter of the tooth flank surface are included in Tab. 2 - 6.

The modification of the parameters of the tooth flank surface is only possible through the modification of the parameters of its processing. Thus, once a modification of a given parameter was introduced, a program generating the technological settings for the case in question was launched. The new flank tooth surface served as the basis for the calculation of the parameters  $\alpha$ ,  $\beta_1$ , T,  $B_w$ , K.

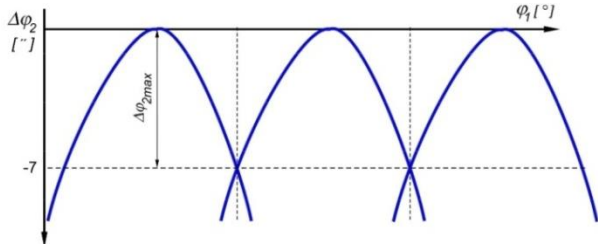


Fig. 4. Motion graph of basic construction pair

Tab. 2. Case I – change of pressure angle

	Designation	Change value
Introduced change	$\alpha$	7'4''
Result changes	$\beta_1$	-1'10''
	K	11.5 $\mu\text{m}$
	$B_w$	1.8 $\mu\text{m}$
	T	-1'28''

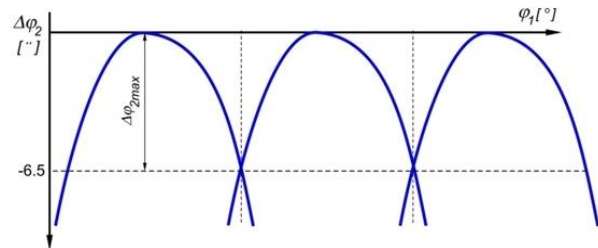


Fig. 5. Motion graph after pressure angle change

Tab. 3. Case II – change of spiral angle

	Designation	Change value
Introduced change	$\beta_1$	0'37''
Result changes	$\alpha$	3'42''
	K	11.4 $\mu\text{m}$
	$B_w$	1.7 $\mu\text{m}$
	T	-2'13''

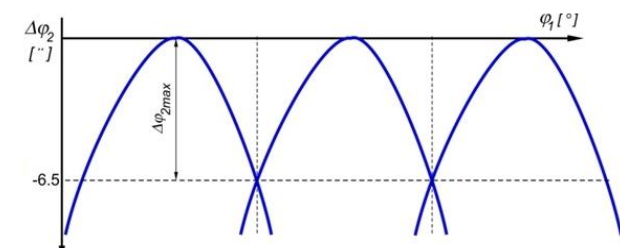


Fig. 6. Motion graph after spiral angle change

Tab. 4. Case III – change of lengthwise curvature factor

	Designation	Change value
Introduced change	K	5,4 $\mu\text{m}$
Result changes	$\alpha$	4'21''
	$\beta_1$	-1'1''
	$B_w$	1.6 $\mu\text{m}$
	T	-2'3''

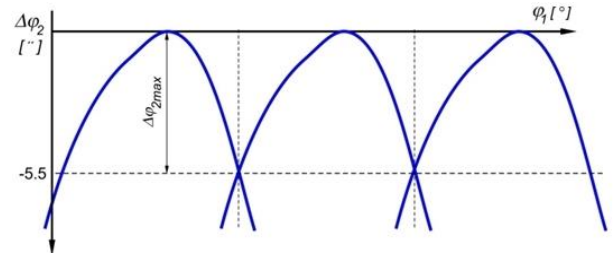


Fig. 7. Motion graph after lengthwise curvature factor change

Tab. 5. Case IV – change of profile curvature

	Designation	Change value
Introduced change	$B_w$	6.2 $\mu\text{m}$
Result changes	$\alpha$	2'50''
	$\beta_1$	-1'9''
	K	11.2 $\mu\text{m}$
	T	1'32''

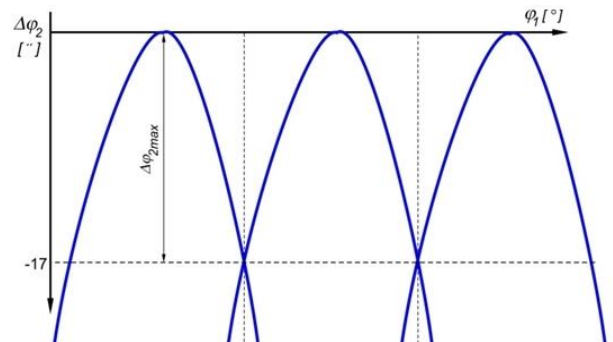


Fig. 8. Motion graph after profile factor change

Tab. 6. Case V – change of tooth flank surface deviation angle

	Designation	Change value
Introduced change	T	2'40''
Result changes	$\alpha$	3'38''
	$\beta_1$	-1'4''
	K	10.9 $\mu\text{m}$
	$B_w$	1.3 $\mu\text{m}$

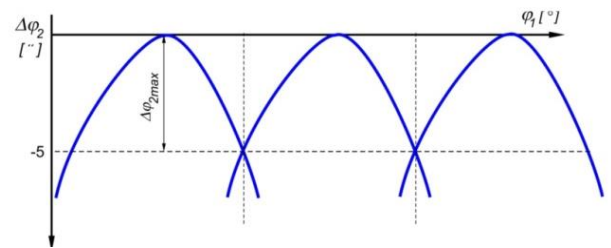


Fig. 9. Motion graph after surface deviation change

## 5. CONCLUSIONS

The knowledge of the nature and change values in the motion graph connected with the changes of parameters in the flank tooth surface allows for a quick and conscious correction of the kinematic accuracy of the bevel gear. Regarding the analyzed gear 17/35 one can draw the following conclusions:

- the increase in the deflection of the profile angle of the tooth (case I), and the change of the angle of the tooth line (case II) have little effect on motion graph. Correcting the surface in this way can slightly reduce the maximum deviation of the motion, without prejudice to its liquidity;
- lengthwise curvature change of the width of the pinion (case III) results in a significant reduction of the maximum deviation of motion, but interferes with mild motion graph, thus losing the desired uniformity of motion;
- kinematics of gear pair is very sensitive to profile factor change (case IV). Small adjustments of the profile factor cause a significant increase in motion deviations. While introducing the changes to profile factor relative to its basic value no improvement in the motion graph has been observed;
- correction of the tooth flank twist can reduce the deviation of the motion without negative changes in the shape of the graph. In comparison with the other changes that were introduced, adjusted twist has given the best kinematic accuracy of the meshing pair.

In order to reach general conclusions, further tests of the gear pairs, with different parameters of its members and different gear ratios, should be performed. Note: all changes in the geometry of the surface of the pinion cause the changes in the contact pattern (Pisula and Płocica, 2012, 2013). Therefore, the potential benefit of improving the accuracy of the kinematic should be considered in relation to the contact pattern and the transmission capacity to carry loads associated with this.

## REFERENCES

1. **Alves J. T., Guignand M., de Vaujany J-P.** (2013), Designing and Manufacturing Spiral Bevel Gears Using 5-axis Computer Numerical Control (CNC) Milling Machines. *ASME Journal of Mechanical Design*, February 2013, Vol. 135, 024502.
2. **De Vaujany J-P., Guignand M., Remond D., Icard Y.** (2007), Numerical and Experimental Study of the Loaded Transmission Error of a Spiral Bevel Gear, *ASME Journal of Mechanical Design*, Vol. 129, 195-200.
3. **Litvin F., Fuentes A.** (2004), *Gear Geometry And Applied Theory*, Cambridge University Press.
4. **Marciniak A.** (2003), *Synthesis and analysis of meshing for Spiral Bevel Gears*, Publishing House of Rzeszow University of Technology, Rzeszow (in Polish).
5. **Pisula J., Płocica M.** (2012), Analysis of Meshing of Bevel Gears on the Basis of a mathematical model of machining processes and Direct Simulation of Cutting in Inventor, *Mechanik*, 1/2012, 78-79 (in Polish).
6. **Pisula J., Płocica M.** (2013), Evaluation of the Quality of Meshing for Designed Pair of Bevel Gears with Independent Design System, *Mechanik*, 2/2013, 138 (in Polish).
7. **Shih Y. P., Fong Z. H.** (2008), Flank Correction for Spiral Bevel and Hypoid Gears on a Six-Axis CNC Hypoid Generator, *Journal of Mechanical Design*, Transactions of the ASME, Vol. 130, 062604.
8. **Simon, V.,**(2008), Machine-Tool Settings to Reduce the Sensitivity of Spiral Bevel Gears to Tooth Errors and Misalignments, *ASME Journal of Mechanical Design*, Vol. 130, 082603.
9. **Wang P. Y., Fong Z. H.** (2005), Adjustability Improvement of Face-Milling Spiral Bevel Gears by Modified Radial Motion (MRM) Method, *Mechanism and Machine Theory*, Vol. 40, 69-89.
10. **Zhang R., Wang T.** (2012), The Influences of Installation Errors on Double Circular Arc Tooth Spiral Bevel Gear Using TCA Method, *Journal of Convergence Information Technology (JCIT)*, Vol. 7, No.1, 1-10.

Research carried out in the framework of the Project "Modern material technologies applied in the aerospace industry", No. POIG.01.01.02-00-015/08-00 in the Operational Programme of Innovative Economy (OPIE). Project co-financed by the European Union through the European Regional Development Fund.

# SOME DIFFERENTIAL EQUATIONS OF ELASTICITY AND THEIR LIE POINT SYMMETRY GENERATORS

Jozef BOCKO\*, Iveta GLODOVÁ\*, Pavol LENGVARSKÝ\*

\*Faculty of Mechanical Engineering, Department of Applied Mechanics and Mechatronics,  
Technical University of Košice, Letná 9, 042 00 Košice, Slovakia

jozef.bocko@tuke.sk, iveta.glodova@tuke.sk, pavol.lengvarsky@tuke.sk

**Abstract:** The formal models of physical systems are typically written in terms of differential equations. A transformation of the variables in a differential equation forms a symmetry group if it leaves the differential equation invariant. Symmetries of differential equations are very important for understanding of their properties. It can be said that the theory of Lie group symmetries of differential equations is general systematic method for finding solutions of differential equations. Despite of this fact, the Lie group theory is relatively unknown in engineering community. The paper is devoted to some important questions concerning this theory and for several equations resulting from the theory of elasticity their Lie group infinitesimal generators are given.

**Key words:** Lie Groups, Symmetry, Differential Equations, Elasticity, Group Generator

## 1. INTRODUCTION

The group theory was discovered by Évariste Galois, who applied it to study of polynomial equations. The so-called finite groups were used as permutation groups and later the symmetry groups were applied in geometry. The idea of continuous groups was first used by Norwegian mathematician Sophus Lie for description of properties of differential equations. The application of continuous groups started systematically in his works and the terms Lie group and Lie algebra are used in honor of this great mathematician. The theory of Lie groups is applied in many different areas of mathematics, physics and engineering (Azad et al., 2010; Drew and Kloster, 1989; Olver, 1986; Sansour and Bednarczyk, 1995; Schwarz, 1982, 1984, 1988; Simo and Fox, 1989). In the field of physics work of German mathematician Emmy Noether, who found connection between symmetries of differential equations and the conservation laws, is very known. The paper describes Lie theory of symmetries of differential equations and for some equations resulting from the elasticity theory infinitesimal generators of their Lie groups are given. The generators have been found by program for symbolic manipulation. More details concerning Lie symmetries of differential equations can be found in Drew and Kloster (1989); Euler and Steeb (1992), Head (1993, 1996), Sansour and Bufler (1992).

## 2. DIFFERENTIAL EQUATIONS AND LIE POINT GROUPS

Starting point is the description of the system of partial differential equations:

$$W_\nu(x_i, u^a, u_i^a, u_{ij}^a, \dots, u_{i_1, \dots, i_k}^a) = 0 \quad (1)$$

$\nu = 1, \dots, N$ , where  $\mathbf{u} = (u^1, \dots, u^m)$  are the functions depending on independent variables  $\mathbf{x} = (x_1, \dots, x_n)$  and:

$$u_{i_1, \dots, i_n}^\alpha = \frac{\partial^{i_1 + \dots + i_n} u^\alpha}{\partial x_1^{i_1} \dots \partial x_n^{i_n}} \quad (2)$$

are the partial derivatives.

Shortly, a Lie group is a group and a manifold at the same time. For any two points a and b in the manifold, there exists multiplication operation giving ab and this group operation has a continuous structure of the manifold.

Change of independent and dependent variables can be represented by the finite transformations:

$$\begin{aligned} \bar{x}_i &= \phi_i(\mathbf{x}, \mathbf{u}, \varepsilon) \\ \bar{u}^\alpha &= \psi^\alpha(\mathbf{x}, \mathbf{u}, \varepsilon) \end{aligned} \quad (3)$$

where  $\varepsilon \in \mathbb{R}$  is a parameter of a group. Expanding (3) by Taylor series at  $\varepsilon = 0$  gives relations:

$$\begin{aligned} \bar{x}_i &= x_i + \varepsilon \xi_i(\mathbf{x}, \mathbf{u}) + o(\varepsilon^2) \\ \bar{u}^\alpha &= u^\alpha + \varepsilon \eta^\alpha(\mathbf{x}, \mathbf{u}) + o(\varepsilon^2) \end{aligned} \quad (4)$$

with the substitutions:

$$\begin{aligned} \xi_i &= \left. \frac{\partial \phi_i(\mathbf{x}, \mathbf{u}, \varepsilon)}{\partial \varepsilon} \right|_{\varepsilon=0} \\ \eta^\alpha &= \left. \frac{\partial \psi^\alpha(\mathbf{x}, \mathbf{u}, \varepsilon)}{\partial \varepsilon} \right|_{\varepsilon=0} \end{aligned} \quad (5)$$

The value  $\varepsilon = 0$  is the identity element of the group. Equations (5) allow us to write infinitesimal generator, or Lie point symmetry vector field by relation:

$$\mathbf{U} = \xi_i \frac{\partial}{\partial x_i} + \eta^\alpha \frac{\partial}{\partial u^\alpha} \quad (6)$$

The transformation of partial derivatives influences the so-called k-th prolongation of a vector field U:

$$\mathbf{U}^{(k)} = \mathbf{U} + \zeta_i^\alpha \frac{\partial}{\partial u_i^\alpha} + \dots + \zeta_{i_1, \dots, i_k}^\alpha \frac{\partial}{\partial u_{i_1, \dots, i_k}^\alpha} \quad (7)$$

where the functions  $\xi_{i_1 \dots i_k}^\alpha$  describe the transformations of partial derivatives of order  $k$ . The functions  $\xi_{i_1 \dots i_k}^\alpha$  are determined according to relations:

$$\zeta_i^\alpha = D_i(\eta^\alpha) - u_s^\alpha D_i(\zeta_s) \quad (8)$$

and:

$$\zeta_{i_1 \dots i_k}^\alpha = D_{i_k}(\zeta_{i_1 \dots i_{k-1}}^\alpha) - u_{i_1 \dots i_{k-1}, s}^\alpha D_{i_k}(\zeta_s) \quad (9)$$

where:

$$D_i = \frac{\partial}{\partial x_i} + u_i^\alpha \frac{\partial}{\partial u^\alpha} + u_{ki}^\alpha \frac{\partial}{\partial u_k^\alpha} + u_{kli}^\alpha \frac{\partial}{\partial u_{ki}^\alpha} \dots \quad (10)$$

is the operator of total differentiation with respect to the independent variable  $x_i$ . The group is symmetry of equation system (2) if and only if the invariant surface condition (symmetry condition):

$$\mathbf{U}^{(k)} \Omega_v = 0 \quad (11)$$

is satisfied, where all  $\Omega_v = 0$ ,  $v = 1, \dots, N$ . The components  $\xi_i$  and  $\eta^\alpha$  of the infinitesimal generator  $\mathbf{U}$  are determined from equations (11).

The infinitesimal generator and Lie group are connected by relation:

$$(\bar{\mathbf{x}}, \bar{\mathbf{u}}) = g_\varepsilon \cdot (\mathbf{x}, \mathbf{u}) = (\phi_\varepsilon(\mathbf{x}, \mathbf{u}), \psi_\varepsilon(\mathbf{x}, \mathbf{u})) = e^{\varepsilon \mathbf{U}}(\mathbf{x}, \mathbf{u}) \quad (12)$$

Here, the Greek letter  $\varepsilon$  is reserved for the parameter of the group and accordingly it does not represent partial differentiation. The function  $\mathbf{f}$  undergoes the transformation by the group element  $g_\varepsilon$  in accordance with relation:

$$\bar{\mathbf{u}} = \bar{\mathbf{f}}_\varepsilon(\bar{\mathbf{x}}) = (g_\varepsilon \mathbf{f})(\bar{\mathbf{x}}) = [\psi_\varepsilon \circ (\mathbf{1} \times \mathbf{f})] \circ [\phi_\varepsilon \circ (\mathbf{1} \times \mathbf{f})]^{-1}(\bar{\mathbf{x}}) \quad (13)$$

where  $\mathbf{1}$  represents the identity function  $\mathbf{1}(\mathbf{x}) = \mathbf{x}$ .

Calculation of the Lie vector fields from equations (11) is tedious work. It involves a large amount of symbolic calculations that is better done by computer. Fortunately, different packages in computer algebra systems exist implementing Lie symmetry computations (Champagne et al., 1991; Lie, 1891, 1896; Vu et al., 2012).

### 3. THICK-WALLED PIPE

Thick-walled pressure vessels and pipes have many applications in engineering practice. Differential equation describing radial stress in a pipe is:

$$\frac{d^2 \sigma(r)}{dr^2} + \frac{3}{r} \frac{d\sigma(r)}{dr} = 0 \quad (14)$$

where  $\sigma(r)$  is the radial stress and  $r$  is the independent variable representing radius. As was mentioned above, there are number programs for solving determining equations of the vector fields resulting from equation (11). They work under different systems for symbolic manipulations, e.g. Reduce, Mathematica, Maple, and so on (Champagne et al., 1991; Lie, 1891, 1896; Vu et al., 2012). In our case we have used DESOLVII [19] working under

system Maple. For equation (14) the program DESOLVII gives us the following Lie symmetry vector fields:

$$\begin{aligned} \mathbf{U}_1 &= -2\sigma^2 \frac{\partial}{\partial \sigma} + \sigma r \frac{\partial}{\partial r} \\ \mathbf{U}_2 &= \frac{1}{r^2} \frac{\partial}{\partial \sigma} \\ \mathbf{U}_3 &= r \frac{\partial}{\partial r} \\ \mathbf{U}_4 &= r^3 \frac{\partial}{\partial r} \\ \mathbf{U}_5 &= -\frac{2\sigma}{r^2} \frac{\partial}{\partial \sigma} + \frac{1}{r} \frac{\partial}{\partial r} \\ \mathbf{U}_6 &= \sigma \frac{\partial}{\partial \sigma} \\ \mathbf{U}_7 &= \sigma r^3 \frac{\partial}{\partial r} \\ \mathbf{U}_8 &= \frac{\partial}{\partial \sigma} \end{aligned} \quad (15)$$

These vector fields are infinitesimal generators of Lie groups of symmetries of differential equation describing radial stress in thick-walled pipe. The corresponding Lie groups can be established from vector fields according to equation (12).

### 4. AXISYMMETRIC PLATE

Differential equation for deformation of axisymmetric plate loaded by uniformly distributed load can be written as:

$$\frac{d^3 w(r)}{dr^3} + \frac{1}{r} \frac{d^2 w(r)}{dr^2} - \frac{1}{r^2} \frac{dw(r)}{dr} = Q \quad (16)$$

where  $w(r)$  is the deflection of the plate at the radius  $r$ , the constant  $Q = \frac{T}{D}$  depends on the constant uniformly distributed load  $T$  and the constant plate stiffness  $D$ . The plate stiffness is

$$D = \frac{E h^3}{12(1-\nu^2)} \quad (17)$$

where  $E$  and  $\nu$  is Young modulus and Poisson ratio of plate material, respectively;  $h$  is the plate thickness.

Here again the program DESOLVII has been used for solution of determining equations that correspond to the equation (16). Resulting infinitesimal generators are:

$$\begin{aligned} \mathbf{U}_1 &= Q r^3 \frac{\partial}{\partial w} + 3 r \frac{\partial}{\partial r} \\ \mathbf{U}_2 &= r^2 \frac{\partial}{\partial w} \\ \mathbf{U}_3 &= (Q r^3 - 9w) \frac{\partial}{\partial w} \\ \mathbf{U}_4 &= \ln(r) \frac{\partial}{\partial w} \\ \mathbf{U}_5 &= \frac{\partial}{\partial w} \end{aligned} \quad (18)$$

### 5. VIBRATING BEAM WITH DAMPING

Differential equation for vibration of a beam with damping is:

$$\frac{\partial^4 u(x,t)}{\partial x^4} + \frac{k^4}{\alpha^2} \frac{\partial^2 u(x,t)}{\partial t^2} + \mu \frac{\partial^5 u(x,t)}{\partial x^4 \partial t} = 0 \quad (19)$$

where  $u(x,t)$  is the deflection of beam at the position  $x$  and the time instant  $t$ . Constant  $\frac{k^4}{\alpha^2} = \frac{\rho A}{EJ}$  depends on the material density  $\rho$ , Young modulus  $E$ , the cross-section area  $A$  and moment of inertia of the beam's cross-section  $J$ .  $\mu$  is the coefficient of internal damping of material.

Determining equations (11) for differential equation (19) have been solved by program DESOLVII. Resulting infinitesimal generators are:

$$\begin{aligned} U_1 &= u \frac{\partial}{\partial u} \\ U_2 &= \frac{\partial}{\partial t} \\ U_3 &= \frac{\partial}{\partial x} \\ U_4 &= f(x,t) \frac{\partial}{\partial u} \end{aligned} \quad (20)$$

Here, function  $F(x,t)$  is any solution of equation (19). The vector field  $U_2$  represents simple shifting in time, the vector  $U_3$  shifting in the direction  $x$ .

### 6. MEMBRANE

Differential equation of a stretched membrane in the plane  $x,y$  which is loaded by the constant pressure  $p$  can be written in the form:

$$\frac{\partial^2 w}{\partial x^2} + \frac{\partial^2 w}{\partial y^2} = -\frac{p}{S} \quad (21)$$

where  $w(x,y)$  is the deflection of a membrane perpendicular to the membrane plane and  $S$  is the tension force per unit length of the membrane. Here, the infinitesimal generators of equation (21) are:

$$\begin{aligned} U_1 &= w \frac{\partial}{\partial w} \\ U_2 &= g_1(x,y) \frac{\partial}{\partial x} \\ U_3 &= g_2(x,y) \frac{\partial}{\partial y} \\ U_4 &= g_3(x,y) \frac{\partial}{\partial w} \end{aligned} \quad (22)$$

The functions  $g_1(x,y)$ ,  $g_2(x,y)$ ,  $g_3(x,y)$  represent any solution of differential equation (21).

### 7. PLATE ON ELASTIC FUSS-WINKLER FOUNDATION

Differential equation describing deformation of a plate on elastic Fuss-Winkler foundation is:

$$D \left( \frac{\partial^4 w}{\partial x^4} + 2 \frac{\partial^4 w}{\partial x^2 \partial y^2} - \frac{\partial^4 w}{\partial y^4} \right) + K w(x,y) = p(x,y) \quad (23)$$

where  $w(x,y)$  is the deflection of the plate at the point with the coordinates  $x,y$ , constant  $D$  is the plate stiffness given by equation (17),  $K$  is the coefficient of subgrade reaction and  $p(x,y)$  is the pressure acting on the plate. The Lie group generators of given differential equation are:

$$\begin{aligned} U_1 &= \frac{\partial}{\partial x} \\ U_2 &= \frac{\partial}{\partial y} \\ U_3 &= x \frac{\partial}{\partial y} - y \frac{\partial}{\partial x} \\ U_4 &= w \frac{\partial}{\partial w} \\ U_5 &= h(x,y) \frac{\partial}{\partial w} \end{aligned} \quad (24)$$

Here,  $h(x,y)$  is any solution of differential equation (23). The vector fields  $U_1$ ,  $U_2$  represent simple shifting along the coordinate  $x$  and  $y$  respectively.

Let us now compute less trivial example of transformation that belong to the Lie vector:

$$U_3 = x \frac{\partial}{\partial y} - y \frac{\partial}{\partial x} \quad (25)$$

For the transformation of the independent variable  $x$  we have:

$$\begin{aligned} U_3(x) &= -y \\ U_3^2(x) &= -U_3(y) = -x \\ U_3^3(x) &= -U_3(x) = y \\ U_3^4(x) &= U_3(y) = x \\ &\vdots \end{aligned} \quad (26)$$

$$\begin{aligned} \bar{x} &= x + \varepsilon(-y) + \frac{\varepsilon^2}{2!}(-x) + \frac{\varepsilon^3}{3!}(y) + \frac{\varepsilon^4}{4!}(x) + \dots = \\ &= x \cos \varepsilon - y \sin \varepsilon \end{aligned}$$

For the independent variable  $y$  we have similar relation:

$$\begin{aligned} U_3(y) &= x \\ U_3^2(y) &= -y \\ U_3^3(y) &= -x \\ U_3^4(y) &= y \\ &\vdots \end{aligned} \quad (27)$$

$$\begin{aligned} \bar{y} &= y + \varepsilon(x) + \frac{\varepsilon^2}{2!}(-y) + \frac{\varepsilon^3}{3!}(-x) + \frac{\varepsilon^4}{4!}(y) + \dots = \\ &= y \cos \varepsilon + x \sin \varepsilon \end{aligned}$$

We see that vector  $U_3$  is connected with the rotation of variables in the plain  $xy$ .

All transformation groups that belong to vectors (24) are:

$$\begin{aligned} G_1 : (x, y, w) &\mapsto (x + \varepsilon, y, w) \\ G_2 : (x, y, w) &\mapsto (x, y + \varepsilon, w) \\ G_3 : (x, y, w) &\mapsto (x \cos \varepsilon - y \sin \varepsilon, x \sin \varepsilon + y \cos \varepsilon, w) \\ G_4 : (x, y, w) &\mapsto (x, y, e^\varepsilon w) \\ G_5 : (x, y, w) &\mapsto (x, y, w + \varepsilon h(x, y)) \end{aligned} \quad (28)$$

The groups (28) represent transformations that convert solutions of differential equation (23) into new solutions of the same equation.

## 8. CONCLUSIONS

The notion of Lie group is very important in the current mathematics and physics. The paper analyzes differential equations resulting from different branches of elasticity theory from the point of view of their symmetries. Lie vectors of corresponding Lie groups symmetries of differential equations have been computed by computer program DESOLVII. Infinitesimal generators of Lie group symmetries give us additional information that is not visible during classical solutions of differential equations.

## REFERENCES

1. **Azad H., Mustafa M. T., Arif A. F. M.** (2010), Analytic Solutions of Initial-Boundary-Value Problems of Transient Conduction Using Symmetries, *Applied Mathematics and Computation*, Vol. 215, 4132-4140.
2. **Bluman G. W., Cole J. D.** (1974), *Similarity Methods for Differential Equations*, Springer-Verlag, New York, 1974.
3. **Champagne B., Hereman W., Winternitz P.** (1991), The Computer Calculation of Lie Point Symmetries of Large Systems of Differential Equations, *Computer Physics Communications*, Vol. 66, 319-340.
4. **Drew M. S., Kloster S.** (1989), Lie Group Analysis and Similarity Solutions for the Equation  $\frac{\partial^2 u}{\partial x^2} + \frac{\partial^2 u}{\partial y^2} + \frac{\partial^2 (e^{2u})}{\partial z^2} = 0$ , *Nonlinear Analysis, Theory Methods Applications*, Vol. 13, No. 5, 1989, 489-505.
5. **Euler N., Steeb W.-H.** (1992), *Continuous Symmetries, Lie Algebras and Differential Equations*, Brockhaus AG, Mannheim.
6. **Head A. K.** (1993), LIE a PC Program for Lie Analysis of Differential Equations, *Computer Physics Communications*, Vol. 71, 241-248.
7. **Head A. K.** (1996), *Instructions for Program LIE ver. 4.5*, CSIRO, Australia.
8. **Lie S.** (1891), *Vorlesungen über Differentialgleichungen mit bekannten infinitesimalen Transformationen*, Teubner, Leipzig.
9. **Lie S.** (1896), *Geometrie der Berührungstransformationen*, Teubner, Leipzig.
10. **Olver P. J.** (1986), *Applications of Lie Groups to Differential Equations*, Springer-Verlag, New York.
11. **Sansour C., Bednarczyk H.** (1991), Shells at Finite Rotations with Drilling Degrees of Freedom, Theory and Finite Element Formulation, In: Glowinski R., Ed., *Computing Methods in Applied Sciences and Engineering*, Nova Sci. Publish., New York, 163-173.
12. **Sansour C., Bednarczyk H.** (1995), The Cosserat Surface as a Shell Model, Theory and Finite-Element Formulation, *Computer Methods in Applied Mechanical Engineering*, Vol. 120, 1-32.
13. **Sansour C., Bufler H.** (1992), An Exact Finite Rotation Shell Theory, its Mixed Variational Formulation, and its Finite Element Implementation, *International Journal for Numerical Methods in Engineering*, Vol. 34, 73-115.
14. **Schwarz F.** (1982), Symmetries of the Two-Dimensional Korteweg-de Vries Equation, *Journal of the Physical Society of Japan*, Vol. 51, No. 8, 2387-2388.
15. **Schwarz F.** (1984), Lie Symmetries of the von Kármán Equations, *Computer Physics Communications*, Vol. 31, 113-114.
16. **Schwarz F.** (1988), Symmetries of Differential Equations from Sophus Lie to Computer Algebra. *SIAM Review*, Vol. 30, No. 3, 450-481.
17. **Sherring J., Head A. K., Prince G. E.** (1997), DIMSYM and LIE: Symmetry Determination Packages. Algorithms and Software for Symbolic Analysis of Nonlinear Systems, *Mathematical and Computer Modelling*, Vol. 25, No. 8-9, 153-164.
18. **Simo J. C., Fox D. D.** (1989), On a Stress Resultant Geometrically Exact Shell Model, Part I.: Formulation and Optimal Parametrization, *Computer Methods in Applied Mechanics and Engineering*, Vol. 72, 267-304.
19. **Vu K. T., Jefferson G. F., Carminati J.** (2012), Finding Higher Symmetries of Differential Equations Using the MAPLE Package DESOLVII, *Computer Physics Communications*, Vol. 183, No. 4, 1044-1054.

The work has been accomplished under the research project of Slovak grant agency VEGA 1/1205/12 - Numerical modeling of mechatronic systems.

## STRESS CONCENTRATION RESULTING FROM IRREGULAR SHAPE OF EXPLOSIVELY CLADDED MATERIALS CONNECTIONS – FEM SIMULATION

Andrzej KUREK\*, Adam NIESŁONY\*, Marta KUREK\*

\*Faculty of Mechanical Engineering, Department of Mechanics and Machines Design, Opole University of Technology,  
ul. Mikołajczyka 5, 45-271 Opole, Poland

[a.kurek@po.opole.pl](mailto:a.kurek@po.opole.pl), [a.nieslony@po.opole.pl](mailto:a.nieslony@po.opole.pl), [ma.kurek@po.opole.pl](mailto:ma.kurek@po.opole.pl)

**Abstract:** The paper contains a numerical analysis of interface zone steel-titanium bimetal obtained by explosive cladding method. Due to the waviness of the zone, and various properties of the constituent material of the materials type contain structural notch. Therefore it is important inter alia in terms of presentation of the results of fatigue are the maximum stresses that occur just in the area of the zone. In the paper the stress concentration factor and the proposed method of modelling the joint zone of a sinusoidal profile, characterized by the same coefficient of stress concentration at the actual profile.

**Keywords:** FEM, Explosive Cladding, Interference Zone

### 1. INTRODUCTION

Energy of explosion has been applied for peaceful aims for a long time. Explosive materials can be applied for mineral crushing, demolition of buildings, fire suppression (blowing the flame away), stretching the belts and filling the airbags, shooting rackets or rescue cartridges, treatment of metallic and non-metallic materials (pressure welding, hardening, pressing, forming, generation of phase changes). Intense energy released in a short time while explosion gives a possibility of realization of technological processes which could not be realized in typical conditions. The mentioned technologies using the explosion force have one common feature – suitable application of extreme values of velocity and pressure accompanying the explosion.

Explosive cladding allows joining materials with completely different properties which are difficult to obtain by means of other methods of joining (Nieslony et al., 2010). Clad obtained with this method are materials of strongly gradient properties and they have complex joining zones (Čížek et al., 2010, Karolczuk et al., 2013, Wronka, 2010, 2011). Materials obtained by this method can also be affected by mean stresses, which can influence the results of fatigue tests, more about this problem can be found in Lindemann and Wagner (1997).

The clad materials are often applied in processing apparatus (chemical and power industries). Wide application of titanium and its alloys in power engineering (condensers, steam condensers, heat exchangers and steam turbines in power plants and thermal-electric power stations) causes that the problem of fatigue life of bimetallic clads, for example, those of steel-titanium type, becomes more and more important (Jiang et al., 2014). As for many applications, fatigue life of clads is the most important parameter. Taking the specificity of the problem into account, the tests are performed according to suitable standards, but the tests not included into the standards are also realized (Sun, 2013; Zareie Rajani HR, 2013). The strength tests presented in this paper concern the metallic composite, so-called clad, obtained during so-called explosive cladding (Findik, 2011; Szulc et al., 2007). This paper is a continuation of the previous papers concerning strength

of clad materials (Kurek and Nieslony, 2012), and special attention is paid to fatigue life of such materials. To address this problem, a numerical analysis of the interference zone of this bimetal, using FEM was performed. A similar approach, but for welded joints, was presented by Dong (2001).

An example of explosively cladded interference zone is shown in Fig. 1.



Fig. 1. Example of interference zone of explosively cladded steel-titanium

### 2. SIMULATION

When modeling the interface zone COMSOL Multiphysics 3.5 environment was used for finite element method calculations. Due to the lack of exfoliation and high resistance to static tearing the interface was modeled as an integral and inseparable. Because of possible melting areas, in which on the basis of metallographic studies intermetallics and non-metallic inclusions were noted (Król et al., 2007), were not considered the calculation assumes two homogeneous metal zones: titanium ( $E = 105$  GPa,  $\nu = 0.33$ ) and steel ( $E = 203$  GPa,  $\nu = 0.33$ ).

The profile of the bimetal interface was modeled in three ways:

1. as a straight line,
2. aligning it using sine function, and
3. the representation of the shape of the actual connections based on microscopic images of the selected portion of the bimetal.

In mode 1) and 3) the transition between metallic zones of titanium and steel was defined in a geometric manner with the line. In mode 2) a change in the material properties while FEM calculations was defined by the logical function that allowed rapid change of amplitude and period of the sine function defining the transition lines represented by formula (1).

$$E = \begin{cases} E_1 & \text{dla } y_1 > \left(y - y_2 \cdot \sin\left(\frac{x-x_1}{x_1}\right)\right) \\ E_2 & \text{dla } y_1 \leq \left(y - y_2 \cdot \sin\left(\frac{x-x_1}{x_1}\right)\right) \end{cases} \quad (1)$$

where:  $E_1, E_2$  – Young's modules of particular materials,  $x, y$  – coordinates of the FEM model,  $x_1$  – wavelength ratio,  $y_1$  – coordinates of the modeled sample middle,  $y_2$  – wave height.

In this case also and adaptive generation of FEM mesh was used, which is based on the following grid congestions around the big changes (gradient method).

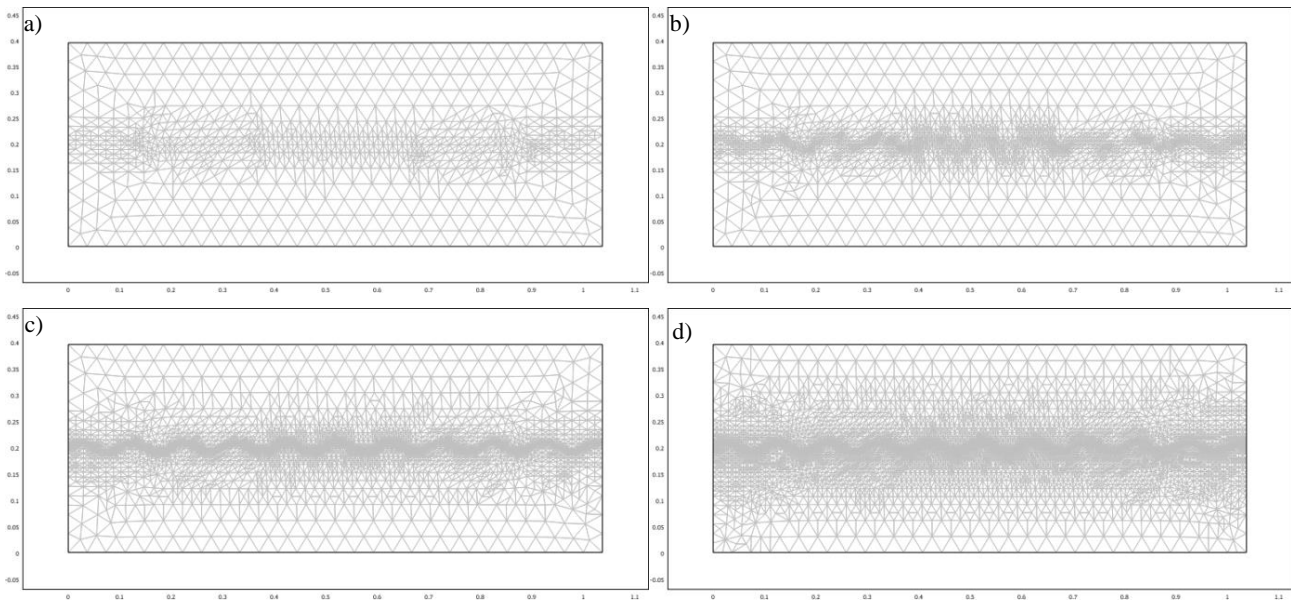


Fig. 2. Steps of FEM mesh compaction by an adaptive method

A model of the interface real shape was obtained by performing a micrograph of the sample used for fatigue test as shown in Fig. 3.



Fig. 3. Real interference zone for titanium-steel bimetal used for simulations

Due to the lack of information on possible changes in the shape of the interference zone in the direction perpendicular to the microsection spatial joint modeling was abandoned. This limitation allowed for the execution of the plane model. Element was stretched along the interference line by causing maximum displacement on the right edge of the model equal to the length of the sample times 0.001.

In this way, values of stresses induced in material corresponds with the 0.001 of the Young's modulus for constituent materials in areas without affecting the structural notch.

Fig. 4 shows the results of a calculation model with interference profile obtained on the basis of the actual shape of the wave. Fig. 4a. shows the areas of the stress values equal to 220 MPa and 110 MPa for steel and titanium respectively. Fig. 5 shows courses of reduced stresses according to Huber-Mises hypothesis (a) and shear stress  $\tau_{xy}$  (b) for the six cross-sections

taken at the FEM model correspond to the locations marked with numbers from 1 to 6 in Fig. 4.

The next stage of the study was to find a replacement shape for real interference formed as a result of explosive welding (cladding), easy to use but and at the same time able to preserves the characteristics of the real shape. Natural candidate seemed trigonometric sine function.

So an attempt to simulate was taken, shape was obtained by assigning, with the help of the sine function, various Young's modules values to two different materials material – titanium and steel, see eq. (1). Parts above of the waveform of sine function placed in the middle height of the specimen was assigned SB265G1 properties of titanium, while below the properties of the steel S355J2. FEM mesh modeling was performed in COMSOL environment by using adaptive mesh thickening function, which thickens grid mainly in the area of large stress gradients.

The parameters are chosen in such a way that the size of the components is comparable with the earlier model with interference actual shape and size (Fig. 3). Sine function modeled in such a way that the height and length of the wave correspond to the actual dimensions of the images obtained from the microsection shown in Fig. 3. Fig. 7 shows courses of Huber-Mises stress and shear stress for sinusoidal shape steel-titanium connection corresponding to the locations indicated in Fig. 1-6, figs. 6a and 6b.

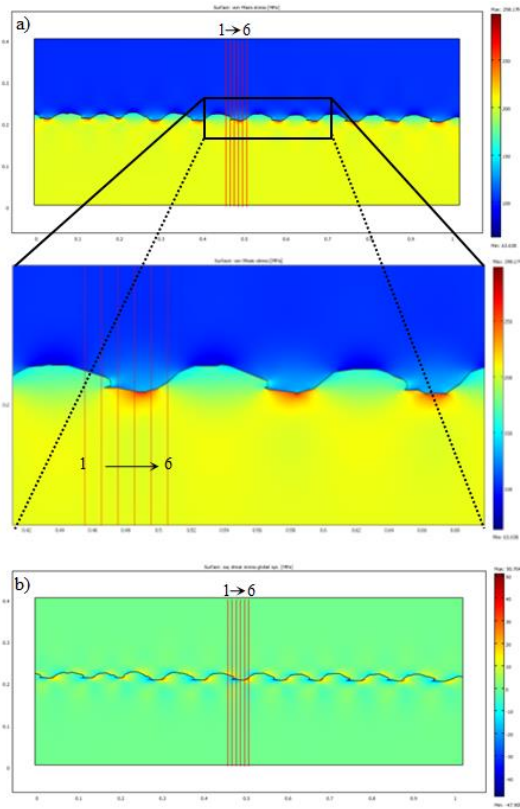


Fig. 4. FEM stress analysis of actual titanium-steel interference in tension, respectively: a) Huber-Mises stresses, b) shear stress

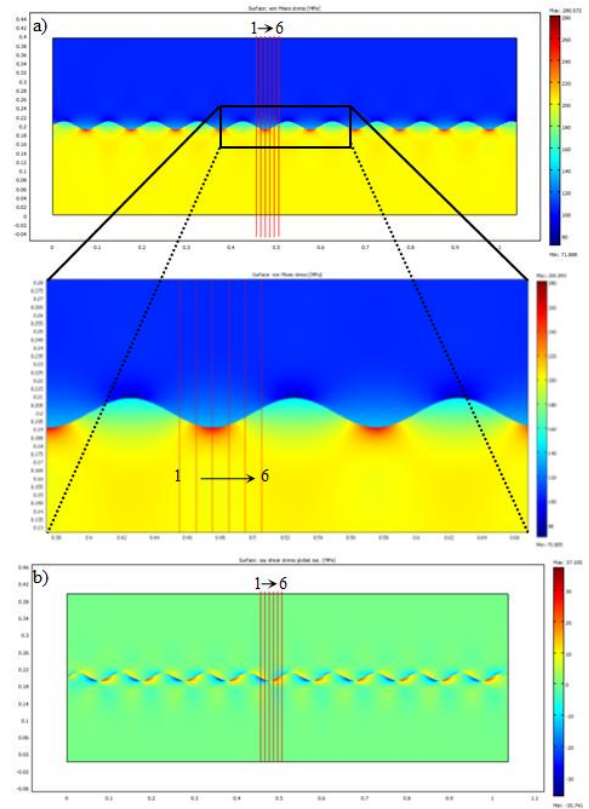


Fig. 6. FEM stress analysis of titanium-steel interference simulated by the sin function, respectively: a) Huber-Mises stresses, b) shear stress

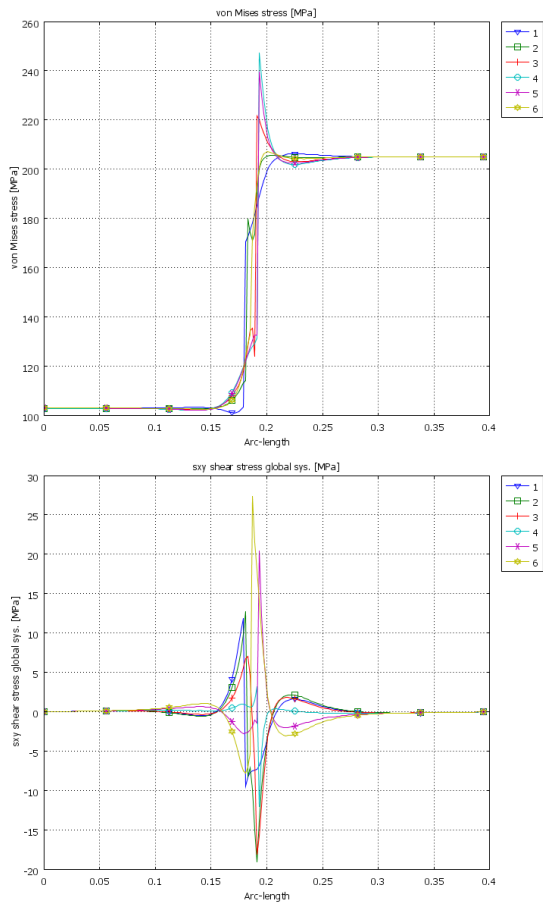


Fig. 5. Courses of stresses for actual steel-titanium interference in six sections marked on Fig. 4, respectively: a) Huber-Mises stresses, b) shear stress

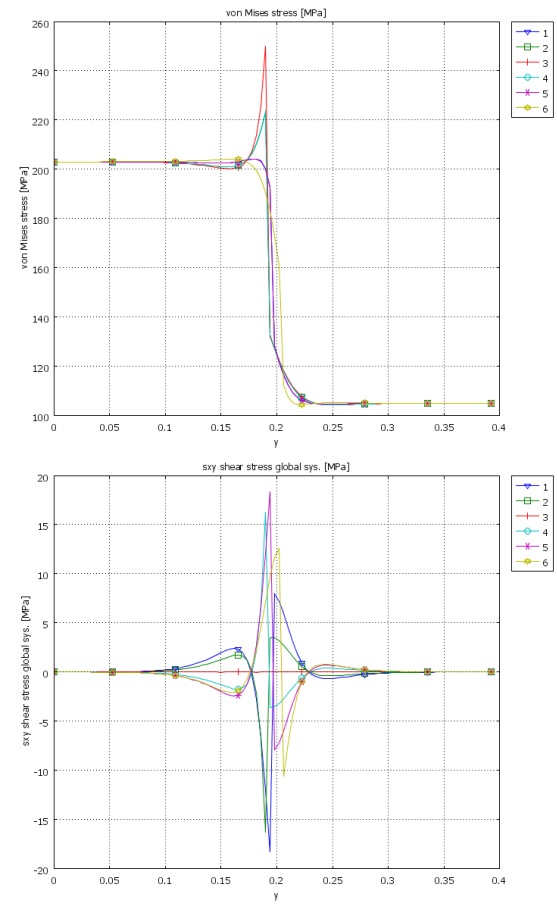


Fig. 7. Courses of stresses for steel-titanium interference simulated by sin function in six sections marked on Fig. 6, respectively: a) Huber-Mises stresses, b) shear stress

### 3. CONCLUSIONS AND OBSERVATIONS

After the simulation calculations we noticed that the replacement of the actual waveform of explosively cladded material connection with sine function with corresponding wavelength and waveheight leads to a close results of reduced stress Huber-Mises in the bottom of the wave. Comparison of Figs. 5a and 7a conclusions can be drawn that the stress distribution around the connectors are similar and there is no need for additional scaling of the sine function. A difference in the maximum stress occurring in the models was also noted, however, this state of affairs can be explained by the difficulty in accurate mapping of the actual waveform, and arising out of the grounds in places with very sharp changes in shape that cause stress concentrations, which are in fact more benign. Stresses in the same area index merger wave in both models, however, are very similar and are up to about 250 MPa for the test case. While in the case of shear stress for connection modeled by the sine function a decrease in the values was noted for both the maximum stress shown on Figure 4b and 6b as on 5b and 7b corresponding to the courses of stress in transverse sections. Such a situation can also be explained by a more regular sinusoidal waveform. The difference in the values of these stresses is not large and is about 9 MPa in the case of stress in transverse sections for Figs. 5b and 7b.

#### REFERENCES

1. Čížek L., Ostroushko D., Szulc Z. (2010), Properties of Sandwich Metals Joined by Explosive Cladding Method, *Archives of Materials Science and Engineering*, Vol. 43, 21–29.
2. Dong P. (2001), A structural stress definition and Numerical Implementation for Fatigue Analysis of Welded Joints, *International Journal of Fatigue*, 23, 865–876.
3. Findik F., (2011), Recent Developments in Explosive Welding, *Materials & Design*, 32, 1081–1093.
4. Jiang H., Yan X., Liu J., Duan X. (2014), Effect of Heat Treatment on Microstructure and Mechanical Property of Ti–Steel Explosive-Rolling Clad Plate, *Transactions of Nonferrous Metals Society of China*, 24, 697–704.
5. Karolczuk A., Kowalski M., Bański R., Żok F. (2013), Fatigue Phenomena in Explosively Welded Steel–Titanium Clad Components Subjected to Push–Pull Loading, *International Journal of Fatigue* 48, 101–108.
6. Król S., Bański R., Szulc Z., Gałka A. (2007), Practical Aspects of Structural Tests of Titanium–Steel Bonds Made by Explosive Cladding and Exposed to Thermal Process Loads, *Advances in Material Science*, vol. 7, nr 4(14), 50–56.
7. Kurek A., Nieslony A. (2012), Fatigue Life Tests of Explosively Cladded Steel–Titanium Bimetal, *Materials Science Forum*, Vol. 726, 106–109.
8. Lindemann J., Wagner L. (1997), Mean stress sensitivity in Fatigue Of  $\alpha$ , ( $\alpha\beta$ ) and  $\beta$  Titanium Alloys, *Materials Science and Engineering*, 234–236, 1118–1121.
9. Nieslony A., Kurek A., Bański R., Čížek L. (2010), *Static and fatigue tests of explosively cladded materials – titanium-steel*, Scientific Papers Opole University of Technology, Series Mechanics, 97, 337/2010 (in Polish).
10. Sun T., Liang J., Guo X., Li L. (2013), Tensile Anisotropy of Cu/Al Clad Metals After Prestrain Using Digital Image Correlation, *Journal of Materials Engineering and Performance*, 22, 3825–3833.
11. Szulc Z., Gałka A., Bański R., Pociła A. (2007), Explosive Cladding With Titanium - the development of technologies and Areas of Industrial Applications, *XII Scientific and Technical Welding Conference "Progress, innovation and Quality Requirements of Welding Processes"*, 13–14 (in Polish).
12. Wronka B. (2010), Testing of Explosive Welding and Welded Joints: Joint Mechanism and Properties of Explosive Welded Joints, *J Mater Sci*, 45, 4078–4083.
13. Wronka B. (2011), Testing of Explosive Welding and Welded Joints. Wavy Character of the Process and Joint Quality, *International Journal of Impact Engineering*, 38, 309–313. 3
14. Zareie Rajani HR., Akbari Mousavi SAA., Madani Sani F. (2013), Comparison of Corrosion Behavior between Fusion Cladded and Explosive Cladded Inconel 625/Plain Carbon Steel Bimetal Plates, *Materials & Design*, 43, 467–474.

The Project was financed from a Grant by National Science Centre (Decision No. DEC-2012/05/B/S T8/02520).

## FRICTION EFFECT IN A PLANE PROBLEM OF PUNCH ACTING ON A HALF-SPACE WEAKENED BY CRACKS

Adam TOMCZYK\*

\*Białystok University of Technology, Faculty of Mechanical Engineering, ul. Wiejska 45C, 15-351 Białystok, Poland

[a.tomczyk@pb.edu.pl](mailto:a.tomczyk@pb.edu.pl)

**Abstract:** This work makes use of singular integral equations method to solve plane contact problem for a half-space containing cracks. This method is based on complex variables. Relationships are presented which help find the contact pressure under the punch and the value of stress intensity factors at the crack tips. A detailed solution is presented for the problem of a punch pressed to the surface of a half-space weakened by a single straight crack. It includes both a situation where the punch has a flat and parabolic base. The influence of friction and the position of the crack on the distribution of the values of stress intensity factors  $K_I$  i  $K_{II}$  in the functions of crack length and distance from the contact zone was analyzed in detail.

**Key words:** Contact Problem, Elastic Half-Space, Crack, Stress Intensity Factor, Friction

### 1. INTRODUCTION

In the mechanical engineering or in the technology of abrasive machining, we often meet the problem connected with friction between cooperating elements. Many classic examples of such problems can be found in various friction brakes, gear units, in grinding processes, or in the problems concerning wheels rolling and braking on rails. In the analysis of such cases it is usually assumed that both elements have no defects, such as edge or internal cracks. It is obvious that the appearance of such defects leads to a redistribution and most of all strong concentration of stresses connected with the effect of a crack.

This work concentrates on the analysis of effects connected with the "sliding" of a punch pressed against an elastic half-space weakened by edge or internal cracks. The analysis makes use of the singular integral equations method including Muskhelishvili's complex potentials (Muskhelishvili, 1962). It covers a plane problem assuming that the punch is perfectly rigid and neglecting the problems of heat generation. In many papers, such problems are modeled by applying load in the form of an appropriate contact pressure on the surface of a half-space in the place where the punch is applied (Hills et al., 1993; Hills and Nowell, 1994). It can be also found for example in the series of works by Goshima and co-authors, which concentrate the problem of rolling (including sliding) of a rigid cylindrical punch on a damaged elastic half-space. This analysis included both fatigue and temperature effects. The analyzed defects included a single edge crack extending to the surface of the elastic half-space (Goshima and Keer, 1990), two edge cracks of varying orientation (Goshima and Kamishima, 1996), a set of periodic cracks (Goshima and Kamishima, 1994; Goshima, 2003). We can also find the solution of a plane problem with a defect in the form of a single internal crack (Goshima and Soda, 1997) and problems with a three-dimensional edge crack (Goshima, 2003; Goshima et al., 1990). Bryant et al. (1984) examined the interaction effects between cylindrical indenter and single-cracked half-space but only for the case when surface-braking crack was presented in contact zone. Other paper by Bryant (Keer and Bryant, 1983) presents a fatigue

problem where cylindrical damaged indenter were considered or problem where a half-space is weakened by two cracks: vertical edge crack and horizontal subsurface crack (Keer et al., 1982). Similar subjects are covered in works by Hasebe et al., (Hasebe, 1981; Hasebe et al., 1989; Okumura et al., 1990; Hasebe and Qian, 1995, 1997, 1998; Qian and Hasebe, 1997), where for example a punch is applied with one rounded and one sharp end (Hasebe and Qian, 1998). The problem of contact between the punch and a half-space weakened by cracks was also analyzed by Panasyuk and co-authors (Panasyuk et al., 1995 2000; Datsyshyn et al., 2001), where trajectories are found for edge cracks in the context of fatigue (Datsyshyn et al., 2001). A detailed analysis has also been provided for the problem of a flat-based punch on the surface of a half-space weakened by a internal (subsurface) crack, where the faces of the crack are in contact (Panasyuk et al., 1995). For last years a problem of interaction between crack and punch has been applied to FGM materials. It was analyzed parabolic or cylindrical stamp acting on graded coatings (Guler and Erdogan, 2007) or the case when the base of the punch was assumed to be flat (Dag and Erdogan, 2002).

### 2. FORMULATION OF THE PROBLEM

Let us assume that into the  $y = 0$  surface of an elastic half-space  $-\infty < x < \infty$ ,  $y \leq 0$  with internal cracks a punch of any shape (Fig. 1) is pressed with normal force  $P$  and slide under the influence of tangential force  $\rho P$ ,  $\rho$  - friction coefficient. Let us also assume that under the influence of such loading the punch is in a limit equilibrium condition. Size of the contact zone between punch and surface of half-space is  $2a$ . It should be noted that moment affects the punch preventing it from turning.

The boundary conditions on the  $y = 0$  plane can be noted as:

$$\begin{aligned} \sigma_{xy} + \rho \sigma_y &= 0, \quad v = f(x) + C \\ x \in L_0 &= \{x: -a < x < a\} \end{aligned} \quad (1)$$

$$\sigma_y - i\sigma_{xy} = p_0(x) = 0, \quad x \notin L_0 \quad (2)$$

where  $\sigma_y$ ,  $\sigma_{xy}$  are the normal and tangent component of the stress tensor,  $v$  is a component of the displacement vector in the  $y$  direction,  $f(x)$  – a function describing the shape of the punch base, and  $C$  – constant (vertical displacement of the punch).

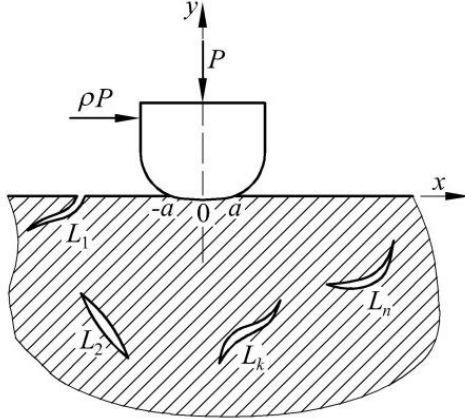


Fig. 1. Scheme of considered problem

The edges of the crack are assumed to be under a self-balanced load in the following form:

$$N^\pm(t) + iT^\pm(t) = p(t), \quad t \in L = \bigcup_{k=1}^n L_k \quad (3)$$

where  $N$  and  $T$  are a normal and tangential component of the surface stress vector on the faces of the crack,  $L_k (k = \overline{1, n})$  – the contour of  $k$ -th crack, “+” and “-” denote left and right edges of the  $L_k$  contour respectively.

General complex stress potentials for a system of curved cracks in a half-space affected by external load, are as follows (Muskhelishvili, 1962; Savruk, 1981):

$$\Phi_1(z) = \Phi_0(z) + \Phi(z), \quad \Psi_1(z) = \Psi_0(z) + \Psi(z), \quad (4)$$

$$\Phi_0(z) = -\frac{1}{2\pi i} \int_{L_0} \frac{p_0(t) dt}{t-z} \quad (5)$$

$$\Psi_0(z) = -\frac{1}{2\pi i} \int_{L_0} \left[ \frac{p_0(t)}{t-z} - \frac{tp_0(t)}{(t-z)^2} \right] dt$$

$$\Phi(z) = \frac{1}{2\pi} \int_L \left[ \left( \frac{1}{t-z} - \frac{1}{\bar{t}-z} \right) g'(t) dt + \frac{t-\bar{t}}{(\bar{t}-z)^2} \overline{g'(t)} d\bar{t} \right]$$

$$\Psi(z) = \frac{1}{2\pi} \int_L \left[ \left( \frac{1}{t-z} - \frac{1}{\bar{t}-z} - \frac{(t-\bar{t})(\bar{t}+z)}{(\bar{t}-z)^3} \right) \overline{g'(t)} d\bar{t} - \left( \frac{\bar{t}}{(t-z)^2} - \frac{\bar{t}}{(\bar{t}-z)^2} \right) g'(t) dt \right]$$

where  $p_0$  denotes loading of the edge of the half-space and  $g'(t)$  is an unknown function on the contours of the cracks.

The derivative of vertical displacement of the edge of the half-space can be given as follows (Gallin, 1980):

$$2G \frac{\partial v(x,0)}{\partial x} = -\frac{\kappa-1}{2} \tau(x) + \frac{\kappa+1}{2\pi} \int_{L_0} \frac{\sigma(t)}{t-z} dt + \text{Im} \left[ \kappa \Phi(x) - \overline{\Phi(x)} - x \overline{\Phi'(x)} - \overline{\Psi(x)} \right] \quad (6)$$

where  $G$  is shear modulus,  $\nu$  – Poisson's ratio,  $\kappa = 3 - 4\nu$ ,  $\sigma$ ,  $\tau$  – respectively: the normal and tangential component of the load on the surface of the half-space.

Satisfying the boundary conditions (1) with the Eq. (6) leads to the following integral equation:

$$\varepsilon \rho \sigma(x) + \frac{1}{\pi} \int_{L_0} \frac{\sigma(t) dt}{t-x} + 2(\kappa+1)^{-1} \text{Im} \left[ \kappa \Phi(x) - \overline{\Phi(x)} - x \overline{\Phi'(x)} - \overline{\Psi(x)} \right] = 4G(\kappa+1)^{-1} f'(x), \quad x \in L_0 \quad (7)$$

where  $\varepsilon = \frac{\kappa-1}{\kappa+1}$ .

To Eq. (7) we have to add a punch equilibrium condition:

$$\int_{L_0} \sigma(t) dt = -P \quad (8)$$

which guarantees uniqueness solution of the Eq. (7)

In the case of a homogeneous half-space, with no cracks,  $\Phi(x) = \Psi(x)$ , and Eqs. (7) and (8) are known (see Muskhelishvili, 1962).

Integral equations on the contours of the cracks can be written in condensed form (Savruk, 1981):

$$\Phi_1(t') + \overline{\Phi_1(t')} + \frac{d\bar{t}'}{dt} \left[ t' \overline{\Phi_1'(t')} + \overline{\Psi_1(t')} \right] = p(t'), \quad t' \in L, \quad (9)$$

where  $\Phi_1(t')$  i  $\Psi_1(t')$  – direct values of complex potentials (4).

To Eq. (9) we also have to add displacement uniqueness conditions while considering each internal crack:

$$\int_{L_k} g'(t) dt = 0, \quad k = \overline{2, n} \quad (10)$$

Eqs. (7) and (9) form a system of singular integral equations of the first and second kind, which allows for the finding of normal contact pressure  $\sigma(x)$  and a derivative of the displacement jumps vector  $g'(t)$  on the contours of cracks. Including conditions (8) and (10) this system has a single solution for any right part in the function class, which have integrable singularities at the ends of the ranges of integration (Muskhelishvili, 1962).

It has to be noted that the system of integral Eqs. (7)–(9) was found under conditions (3). This means that there can be given loads on crack faces or, in a particular case, no load. Such boundary conditions can be realized only when the cracks are within the tensile stress fields. However, as a result of pressing the punch in, some or even all cracks can be found in the field of compression stresses, which is produced in the half-space under the punch. In that situation the faces of the cracks will be in contact. If this is so along the whole length of the crack, than Eqs (7)–(10) can be easily modified, including the continuity of normal displacement on the contours of the crack and friction according to Amonton's law. In the general case we receive a mixed problem on the faces of the crack, which significantly increases the complexity of the solution. However, most works in this field, including this one, analyze these questions without including contact between crack faces.

Complex potential (5) can be presented in the form:

$$\begin{aligned}
 \Phi_0(z) &= \frac{1}{\pi} \int_{L_0} f_{11}(t, z) \sigma(t) dt \\
 \Psi_0(z) &= \frac{1}{\pi} \int_{L_0} h_{11}(t, z) \sigma(t) dt \\
 \Phi_0'(z) &= \frac{1}{\pi} \int_{L_0} g_{11}(t, z) \sigma(t) dt \\
 \Phi(z) &= \frac{1}{\pi} \int_L [f_{21}(t, z) g'(t) dt + f_{22}(t, z) \overline{g'(t)} d\bar{t}] \\
 \Psi(z) &= \frac{1}{\pi} \int_L [h_{21}(t, z) g'(t) dt + h_{22}(t, z) \overline{g'(t)} d\bar{t}] \\
 \Phi'(z) &= \frac{1}{\pi} \int_L [g_{21}(t, z) g'(t) dt + g_{22}(t, z) \overline{g'(t)} d\bar{t}]
 \end{aligned} \tag{11}$$

where:

$$\begin{aligned}
 f_{11}(t, z) &= -\frac{1+i\rho}{2i} \frac{1}{t-z}, & f_{21}(t, z) &= \frac{1}{2} \left( \frac{1}{t-z} - \frac{1}{\bar{t}-z} \right) \\
 f_{22}(t, z) &= \frac{t-\bar{t}}{2(\bar{t}-z)^2}, & g_{11}(t, z) &= -\frac{1+i\rho}{2i} \frac{1}{(t-z)^2} \\
 g_{21}(t, z) &= \frac{1}{2} \left( \frac{1}{(t-z)^2} - \frac{1}{(\bar{t}-z)^2} \right), & g_{22}(t, z) &= \frac{t-\bar{t}}{(\bar{t}-z)^3} \\
 h_{11}(t, z) &= -\frac{1}{2i} \left[ \frac{1-i\rho}{t-z} - \frac{t(1+i)}{(t-z)^2} \right] \\
 h_{21}(t, z) &= -\frac{\bar{t}}{2} \left( \frac{1}{(t-z)^2} - \frac{1}{(\bar{t}-z)^2} \right) \\
 h_{22}(t, z) &= \frac{1}{2} \left( \frac{1}{t-z} - \frac{1}{\bar{t}-z} - \frac{(t-\bar{t})(\bar{t}+z)}{(\bar{t}-z)^3} \right)
 \end{aligned} \tag{12}$$

Taking into account Eqs. (11) and (12), the system of integral Eqs. (7) and (9) can be noted as:

$$\begin{aligned}
 \varepsilon \rho \sigma(x) + \frac{1}{\pi} \int_{L_0} \frac{\sigma(t) dt}{t-x} + \frac{1}{\pi} \operatorname{Im} \int_L [K_1(t, x) g'(t) dt + \\
 + L_1(t, x) \overline{g'(t)} d\bar{t}] = \frac{4G}{\kappa+1} f'(x), \quad x \in L_0
 \end{aligned} \tag{13}$$

$$\begin{aligned}
 \frac{1}{\pi} \int_L [K_2(t, t') g'(t) dt + L_2(t, t') \overline{g'(t)} d\bar{t}] + \\
 + \frac{1}{\pi} \int_{L_0} M(t, t') \sigma(t) dt = p(t'), \quad t' \in L
 \end{aligned} \tag{14}$$

Kernels of the system of Eqs. (13) and (14) are given by functions  $f_{ij}$ ,  $g_{ij}$  and  $h_{ij}$  ( $i, j = 1, 2$ ) described by relations (12), can be represent as follows:

$$\begin{aligned}
 K_1(t, x) &= \frac{2}{\kappa+1} \left[ \kappa f_{21}(t, x) - \overline{f_{22}(t, x)} - x g_{22}(t, x) - \overline{h_{22}(t, x)} \right] \\
 L_1(t, x) &= \frac{2}{\kappa+1} \left[ \kappa f_{22}(t, x) - \overline{f_{21}(t, x)} - x g_{21}(t, x) - \overline{h_{21}(t, x)} \right] \\
 K_2(t, t') &= f_{21}(t, t') + \overline{f_{22}(t, t')} + \frac{dt'}{dt} \left[ t' g_{22}(t, t') + \overline{h_{22}(t, t')} \right] \\
 L_2(t, t') &= f_{22}(t, t') + \overline{f_{21}(t, t')} + \frac{dt'}{dt} \left[ t' g_{21}(t, t') + \overline{h_{21}(t, t')} \right] \\
 M(t, t') &= f_{11}(t, t') + \overline{f_{11}(t, t')} + \frac{dt'}{dt} \left[ t' g_{11}(t, t') + \overline{h_{11}(t, t')} \right]
 \end{aligned} \tag{15}$$

Note, that function  $K_2(t, t')$  includes Cauchy's singular kernel. This part will not be specially singled out, unless numerical integration formulas will be used to carry out the numerical calculations, which are correct for both singular and regular integrals.

### 3. PARTICULAR CASE OF A SINGLE EDGE CRACK

Let us consider a case, where a half-space is weakened by only one straight crack (Fig. 2) Let us introduce a parametric notation of the contour of crack  $L$  and the zone of contact between the punch and the surface of half-space  $L_0$ :

$$t = a\xi, \quad x = a\eta, \quad -1 < \xi, \eta < 1, \quad (t, x \in L_0)$$

$$t = a\omega(\xi), \quad t' = a\omega(\eta), \quad -1 < \xi, \eta < 1, \quad (t, t' \in L) \tag{16}$$

$$\omega(\xi) = -b^* - \frac{l^*}{2} (\xi + 1) e^{i\varphi}, \quad b^* = \frac{b}{a}, \quad l^* = \frac{l}{a}$$

where  $\varphi$  is angle of crack orientation defined according to Fig. 2.

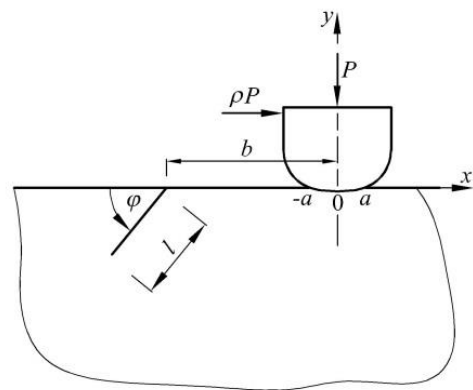


Fig. 2. Scheme of a pressed punch „sliding” on a surface of a single-cracked half-space

Moving to non-dimensional variables and functions the system of integral Eqs. (13) and (14) and the condition of solvability (8) has the following form:

$$\begin{aligned}
 \varepsilon \rho \sigma(\eta) + \frac{1}{\pi} \int_{-1}^1 \frac{\sigma(\xi) d\xi}{\xi - \eta} + \frac{1}{\pi} \operatorname{Im} \int_{-1}^1 [K_1(\xi, \eta) g'(\xi) + \\
 + L_1(\xi, \eta) \overline{g'(\xi)}] d\xi = F(\eta), \quad |\eta| < 1
 \end{aligned} \tag{17}$$

$$\frac{1}{\pi} \int_{-1}^1 \left[ K_2(\xi, \eta) g'(\xi) + L_2(\xi, \eta) \overline{g'(\xi)} \right] d\xi + \frac{1}{\pi} \int_{-1}^1 M(\xi, \eta) \sigma(\xi) d\xi = p(\eta), \quad |\eta| < 1 \quad (18)$$

$$\int_{-1}^1 \sigma(\xi) d\xi = A = \frac{-P}{a}, \quad (19)$$

where:

$$\begin{aligned} \sigma(a\eta) &= \sigma(\eta), & g'(a\omega(\xi))\omega'(\xi) &= g'(\xi) \\ p(a\omega(\xi)) &= p(\eta), & 4G(\kappa+1)^{-1} f'(a\eta) &= F(\eta) \\ aK_1(a\omega(\xi), a\eta) &= K_1(\xi, \eta) \\ aL_1(a\omega(\xi), a\eta) &= L_1(\xi, \eta) \\ aK_2(a\omega(\xi), a\omega(\eta)) &= K_2(\xi, \eta) \\ aL_2(a\omega(\xi), a\omega(\eta)) &= L_2(\xi, \eta) \\ aM(a\xi, a\omega(\eta)) &= M(\xi, \eta) \end{aligned} \quad (20)$$

A solution for the system of integral Eqs. (17)-(18), which satisfies condition (19) will be sought in the class of functions, which have integrable singularities:

$$\begin{aligned} \sigma(\xi) &= w(\xi)q(\xi) \\ w(\xi) &= (1-\xi)^\alpha (1+\xi)^\beta, \quad -1 < \alpha, \beta < 0 \\ g'(\xi) &= (1-\xi^2)^{-1/2} u(\xi) \end{aligned} \quad (21)$$

where  $q(\xi)$  and  $u(\xi)$  are continuous functions in a closed interval  $[-1, 1]$ , and parameters  $\alpha$  and  $\beta$  are roots  $\alpha = -0.5 + \mu$ ,  $\beta = -0.5 - \mu$ ,  $\mu = \arctan \varepsilon \rho$  of characteristic equations:  $\cot \pi \alpha = -\varepsilon \rho$ ,  $\cot \pi \beta = \varepsilon \rho$ .

Let us remind that only for internal cracks condition (10) must be satisfied. However for the case of the edge crack singularity is produced only at the one crack tip (i.e. for  $\xi = +1$ ). At the second tip ( $\xi = -1$ ), which extends to the surface, singularity disappears and also condition (10) can not be satisfied. So the solution of Eqs. (17)-(18) will be sought in the same class of functions (21) but condition (10) should be replaced by:

$$u(-1) = 0 \quad (22)$$

In the case of a homogeneous half-space, with no cracks, there is  $g'(\xi) = 0$  and a system of integral Eqs. (17) and (18) is reduced to a single Eq. (18) when condition (19) is satisfy.

#### 4. NUMERICAL SOLUTION OF SINGULAR INTEGRAL EQUATIONS SYSTEM

For a numerical solution of the system of Eqs. (17)-(19) we will use the quadrature method (or the mechanical quadrature method) (Savruk, 1981; Savruk et al., 1999, Savruk and Tomczyk, 2010) using Gauss-Chebyshev nodes. As a result we receive the following system of linear algebraic equations:

$$\sum_{k=1}^{\hat{n}} a_{mk} q(\xi_k) + \text{Im} \sum_{k=1}^{\hat{n}} \left[ b_{1mk} u(\widehat{\xi}_k) + c_{1mk} \overline{u(\widehat{\xi}_k)} \right] = F(\eta_m), \quad m = 1, \dots, n-1 \quad (23)$$

$$\sum_{k=1}^{\hat{n}} \left[ b_{2mk} u(\widehat{\xi}_k) + c_{2mk} \overline{u(\widehat{\xi}_k)} \right] + \sum_{k=1}^{\hat{n}} d_{mk} q(\xi_k) = p(\widehat{\eta}_m), \quad m = 1, \dots, \widehat{n}-1$$

$$\sum_{k=1}^{\hat{n}} a_{nk} q(t_k) = A, \quad \sum_{k=1}^{\hat{n}} (-1)^k \sqrt{\frac{1-\xi_k}{1+\xi_k}} u(\widehat{\xi}_k) = 0 \quad (24)$$

$$\begin{aligned} \xi_k &= \cos \frac{2k-1}{2n} \pi, & \widehat{\xi}_k &= \cos \frac{2k-1}{2\widehat{n}} \pi \\ \eta_m &= \cos \frac{\pi m}{n}, & \widehat{\eta}_m &= \cos \frac{\pi m}{\widehat{n}} \end{aligned} \quad (25)$$

The unknown values here are functions  $q(\xi)$  and  $u(\xi)$  respectively in nodes  $\xi_k$  and  $\widehat{\xi}_k$ . The coefficients of the unknowns in the system of Eqs. (23) are given by the following formulas:

$$\begin{aligned} a_{mk} &= -\frac{1}{n} (-1)^k \sqrt{1-\xi_k^2} \left\{ \frac{X_0}{1-\eta_m} \left[ \frac{1}{1-\xi_k} - \frac{T_n(\eta_m)}{\eta_m - \xi_k} \right] + \right. \\ &\quad \left. + \frac{R_0}{1+\eta_m} \left[ \frac{(-1)^n}{1+\xi_k} + \frac{T_n(\eta_m)}{\eta_m - \xi_k} \right] + X_3(\eta_m) + X_4(\eta_m) \frac{T_n(\eta_m)}{\eta_m - \xi_k} \right\} \\ a_{nk} &= \frac{\pi}{n} \sqrt{1-\xi_k^2} \left[ w(\xi_k) - (-1)^k \frac{X_0}{1-\xi_k} + (-1)^{k+n} \frac{R_0}{1+\xi_k} \right] \\ b_{1mk} &= \frac{1}{\widehat{n}} K_1(\widehat{\xi}_k, \eta_m), & b_{2mk} &= \frac{1}{\widehat{n}} K_2(\widehat{\xi}_k, \widehat{\eta}_m) \\ c_{1mk} &= \frac{1}{\widehat{n}} L_1(\widehat{\xi}_k, \eta_m), & c_{2mk} &= \frac{1}{\widehat{n}} L_2(\widehat{\xi}_k, \widehat{\eta}_m) \\ d_{mk} &= \frac{1}{n} \sqrt{1-\xi_k^2} \left[ M(\xi_k, \widehat{\eta}_m) w(\xi_k) - \right. \\ &\quad \left. - (-1)^k \frac{X_0 M(1, \widehat{\eta}_m)}{1-\xi_k} + (-1)^{n+k} \frac{R_0 M(-1, \widehat{\eta}_m)}{1+\xi_k} \right] \\ X_0 &= \frac{1}{2} \left[ \frac{2\alpha}{\sin \pi \alpha} - \frac{1}{n} \sum_{k=1}^n X(\xi_k) \sqrt{1-\xi_k^2} \right] \\ R_0 &= \frac{1}{2} \left[ \frac{2\beta}{\sin \pi \beta} - \frac{1}{n} \sum_{k=1}^n R(\xi_k) \sqrt{1-\xi_k^2} \right] \end{aligned} \quad (26)$$

$$X_1(x) = \frac{1}{2} \left[ X(x) \cot \pi \alpha - \frac{1}{\sin \pi \alpha} - R(x) \cot \pi \beta + \frac{1}{\sin \pi \beta} \right]$$

$$X_3(x) = \frac{1}{n} \sum_{r=1}^n w(\xi_r) \sqrt{1-\xi_r^2} F(x, \xi_r, \xi_k)$$

$$X_4(x) = \varepsilon \rho w(x) + X_1(x)$$

$$X(x) = \left( \frac{1-x}{1+x} \right)^\alpha, \quad R(x) = \left( \frac{1+x}{1-x} \right)^\beta$$

$$F(x, \xi_r, \xi_k) = \begin{cases} \frac{T_n(x)}{(x-\xi_k)(x-\xi_r)}, & x \neq \xi_k, x \neq \xi_r, \xi_k \neq \xi_r \\ -\frac{n(-1)^r}{\sqrt{1-\xi_r^2}(\xi_r-x)} + \frac{T_n(x)}{(\xi_r-x)^2}, & x \neq \xi_k = \xi_r \end{cases}$$

where  $Tn(x) = \cos(n \arccos x)$  is a first kind Chebyshev polynomial of  $n$  degree.

Using Lagrange's interpolating polynomial for nodes  $\xi_k$  we can find the values of function  $q(\xi)$  at any point:

$$q(\xi) = -\frac{1}{n} \sum_{k=1}^n (-1)^k q(\xi_k) \sqrt{1-\xi^2} \frac{T_n(x)}{\xi-\xi_k} \quad (27)$$

Particularly, at the ends of the interval  $[-1, 1]$  we receive:

$$q(\pm 1) = \mp \frac{(\pm 1)^n}{n} \sum_{k=1}^n (-1)^k \sqrt{\frac{1 \pm \xi_k}{1 \mp \xi_k}} q(\xi_k) \quad (28)$$

Similarly, we search for the values of function  $u(\xi_k)$  in nodes  $\xi_k$ :

$$u(\xi) = -\frac{1}{n} \sum_{k=1}^n (-1)^k u(\xi_k) \sqrt{1-\xi^2} \frac{T_n(x)}{\xi-\xi_k}, \quad -1 \leq \xi \leq 1 \quad (29)$$

$$u(\pm 1) = \mp \frac{(\pm 1)^n}{n} \sum_{k=1}^n (-1)^k \sqrt{\frac{1 \pm \xi_k}{1 \mp \xi_k}} u(\xi_k) \quad (30)$$

Stress intensity factors at the crack tip  $\xi = 1 (K_{I,II}^+)$  are found with these formulas (Savruk, 1981):

$$K_I^+ - iK_{II}^+ = -\sqrt{\pi a} \left| \omega'(1) \right| \frac{u(1)}{\omega'(1)} \quad (31)$$

It has to be noted that in the case of a flat-based punch contact zone  $L_0$  is known. However, if the punch base is rounded at one or both ends, the dimensions of the contact zone are not known. In these cases the stresses at both ends of the contact zone are finite and for the purpose of finding the location of this zone we have one or two additional conditions. Particularly, for the parabolic punch, which also was the subject of our research, we have additional conditions:

$$q(-1) = q(1) = 0 \quad (32)$$

thus we determine the half width of contact zone  $a$  and the eccentricity  $e$  (distance of the center of these zone from the punch axis).

### 5. ANALYSIS OF RESULTS

The theoretical relations presented in the previous paragraph were used to create numerical algorithms which allow to determine the distribution of contact pressure and the values of stress intensity factors at the crack tip. As it was already mentioned, two different shapes of the base of the punch were considered – flat and parabolic. It was analyzed in detail the influence of the shape of the punch base on the distribution of dimensionless stress intensity factors  $F_I = \frac{K_{I}\sqrt{a}}{P}$ ,  $F_{II} = \frac{K_{II}\sqrt{a}}{P}$ . It was assumed in the numerical calculations that the edges of the crack are free of load ( $N = T = 0$  in Eq. (3)).

Results of numerical analysis prove that existence of crack (or set of cracks) has a significant influence on contact pressure distribution (see Fujimoto et al, 1992, Tomczyk 2011; Savruk and Tomczyk, 2010). It corresponds with both flat and parabolic punch particularly for crack orientation angles from the range

(90°, 180°). For these angles crack tip can be found in material under contact zone directly and produce a “rapidly” perturbation of typical contact pressure distribution. Assuming regular contact pressure distribution in the place where punch acting can produce considerable errors in many contact problems. Only taking into consideration a mutual interaction between crack (or set of cracks) and punch gives a detailed information about character of pressure distribution. This interaction can be neglected for the case of homogenous half-space or when the crack is far away from the punch. As it was mentioned for the case of flat punch contact zone size  $a$  is known. For parabolic punch this size should be obtained by using condition of pressure reducing to zero in the ends of contact zone (see Eq. (32)).

In present analysis the dependence of stress intensity factors values on distance between crack and punch, crack length and its orientation and friction coefficient is discussed. It is also analysed the effect of punch shape (parabolic or flat) on stress intensity factors.

In the case of no friction or for small values of friction coefficient crack located close to the punch can be present in fields of compression stresses. Situation like this can take place for both: when  $0^\circ < \varphi < 90^\circ$  (Fig. 3a), and when  $90^\circ < \varphi < 180^\circ$  (Fig. 3b).

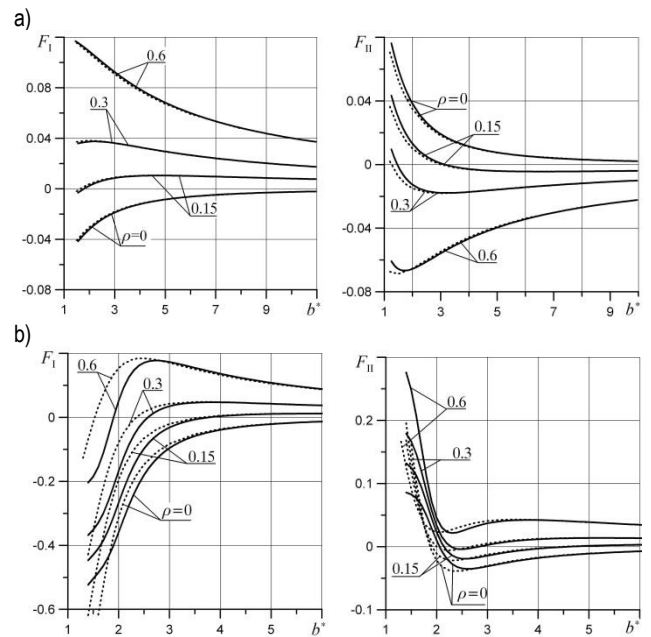


**Fig 3.** The effect of distance between crack and punch on dimensionless stress intensity factors  $F_I$  and  $F_{II}$  for different values of friction coefficient ( $f = 1, \nu = 0.3$ ): a)  $\varphi = 45^\circ$ , b)  $\varphi = 135^\circ$  (dashed lines – parabolic punch, continuous lines – flat punch)

The effect of punch shape is distinctly seen for  $\varphi \in (90^\circ, 180^\circ)$  particular for close cracks when  $b^* < 2.5$  (Fig. 3b, Fig. 4). For cracks defined by  $0^\circ < \varphi < 90^\circ$  the effect of punch shape can be neglected even for small values of distance between crack and punch. When the suitable conditions exist the crack can close when the flat punch is acting while for the case of parabolic punch the same crack is opened. The effect like this is more probable when the angle  $\varphi$  is close to 180° and values of  $b^*$  are very small (Fig. 5).

A very interesting situation we can observe in the Fig. 6. It presents the effect of translation of crack tip into material under

contact zone directly produced by increasing in crack length. It is clearly seen that crack starts to close for certain values of  $l^*$ . This effect appears for small values of friction coefficient earlier than for higher values. Increasing in friction delays crack closure process. Let us note that there is no any influence of punch shape on stress intensity factors in Fig. 6.

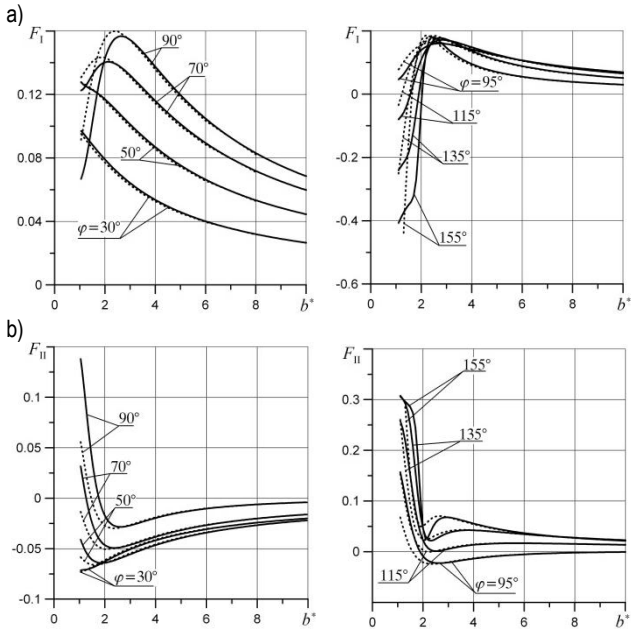


**Fig. 4.** The effect of distance between crack and punch on dimensionless stress intensity factors  $F_I$  (a) and  $F_{II}$  (b) for various crack orientations ( $l^* = 1, \nu = 0.3, \rho = 0.6$ ) (dashed lines – parabolic punch, continuous lines – flat punch)

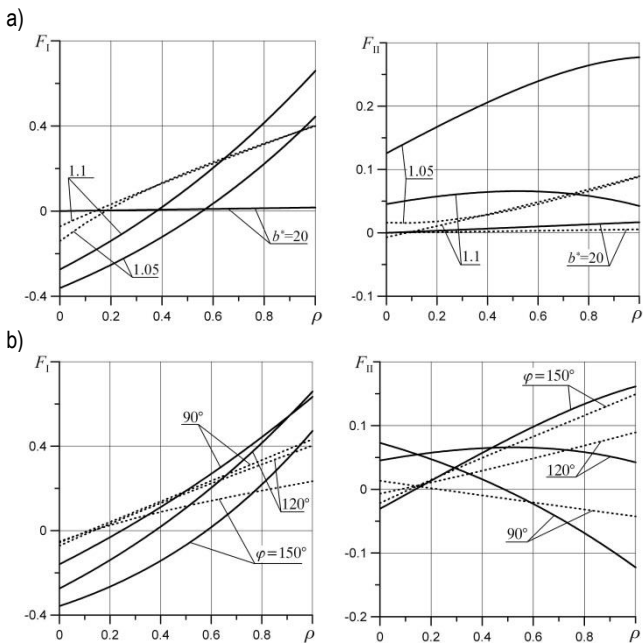


**Fig. 5.** Influence of friction on dimensionless stress intensity factors  $F_I$  and  $F_{II}$  for flat (continuous lines) and parabolic (dashed lines) punch: a) the effect of distance between crack and punch ( $l^* = 0.1, \nu = 0.3, \varphi = 120^\circ$ ), b) the effect of crack orientation ( $l^* = 0.1, b^* = 1.1, \nu = 0.3$ )

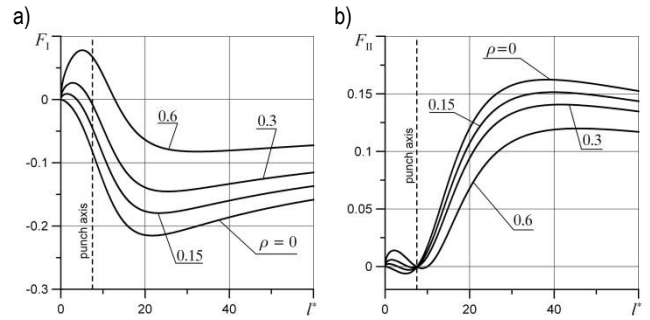


**Fig. 6.** The effect of crack length on dimensionless stress intensity factors  $F_I$  (a) i  $F_{II}$  (b) for various values of friction coefficient ( $b^* = 15, \nu = 0.3, \varphi = 120^\circ$ )

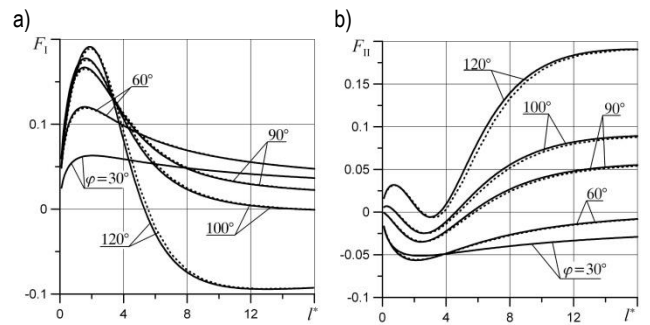


**Fig. 7.** The effect of crack length on dimensionless stress intensity factors  $F_I$  (a) i  $F_{II}$  (b) for various crack orientations ( $b^* = 5, \nu = 0.3, \rho = 0.75$ ) (dashed lines – parabolic punch, continuous lines – flat punch)

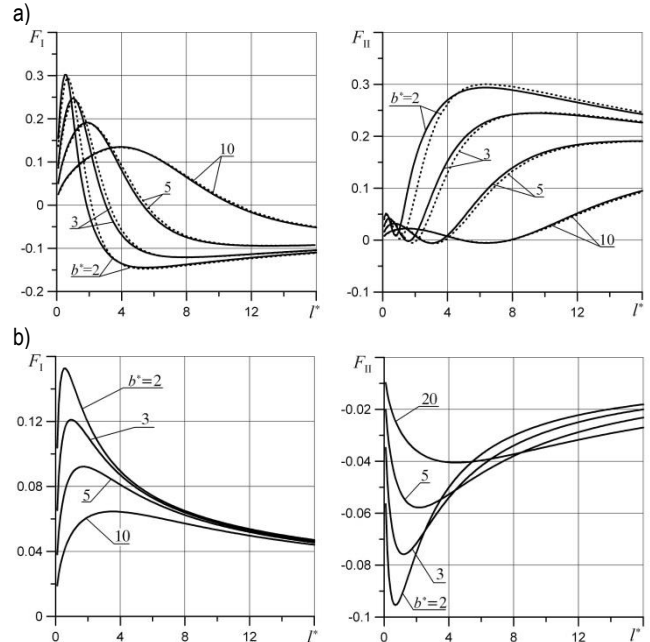


**Fig. 8.** The effect of crack length on dimensionless stress intensity factors  $F_I$  and  $F_{II}$  for various values of distance between crack and punch ( $\rho = 0.75, \nu = 0.3$ ): a)  $\varphi = 120^\circ$ , b)  $\varphi = 45^\circ$  (dashed lines – parabolic punch, continuous lines – flat punch)

It is very characteristic for  $90^\circ < \varphi < 180^\circ$  that factors  $F_I$  and  $F_{II}$  decrease to zero considerably slower (Fig. 8a) than for  $0^\circ < \varphi < 90^\circ$  (Fig. 8b). The effect of crack closure can be achieved much more earlier for higher values of  $\varphi$  (Fig. 7a). This

effect appears more distinctly for  $90^\circ < \varphi < 180^\circ$ . For the case of  $0^\circ < \varphi < 90^\circ$  it can be neglected particularly for small values of  $\varphi$  when it is not visible.

The effect of crack length is very strong in the region of short cracks where  $l < 6$  (Fig. 8). The most dangerous situations appear not for shortest cracks but for cracks where stress intensity factors reaches maximal values. This characteristic length depends on distance between crack and punch mainly and increases as  $b^*$  increases. The effect of punch shape is as clearly as crack is located closer to the punch and for  $90^\circ < \varphi < 180^\circ$  only.

## 6. CONCLUSIONS

This work presents a solution of the problem of a rigid punch acting on a half-space weakened by a set of cracks. In the analysis the method of singular integral equations has been used. It has been analyzed in detail the case of a half-space weakened by a single edge crack while the base of the punch is parabolic or flat. Therefore it has been observed the influence of shape of the base of the punch on the the values of  $K_I$  and  $K_{II}$ . This influence can be neglected for the crack orientation angle  $\varphi \in (0^\circ, 90^\circ)$  as opposed to  $\varphi \in (90^\circ, 180^\circ)$ . For a numerical solution of the system of integral equations the quadrature method has been used, which allowed to reduce this system to a system of linear algebraic equations.

Presented method gives possibility for simultaneously calculating the contact pressure and the values of stress intensity factors. This means that it is possible to take into account the mutual interaction between crack and punch. While analyzing the influence of the punch shape, it has to be noted that it has a significant influence not only on the characteristics of contact pressure distribution, but also on the values of stress intensity factors. This influence is particularly notable for cracks close to the contact zone and decreases as the crack "moves away". So it shows that for far cracks it doesn't matter a character of applied loading: parabolic, asymptotic or even in the form of concentrate force. On the other hand for close cracks it should be noted that even not accounting for friction the shape of the punch is not without importance. Furthermore, it was made a detailed analysis of the influence of the orientation and length of the crack on the values of stress intensity factors  $K_I$  and  $K_{II}$ . For vertically oriented cracks the shape of the punch has no influence on the values of stress intensity factors even for close cracks. Proposed method also allows for description of the changes in the contact zone size and the eccentricity of its center when the parabolic punch is applied.

The method presented here can be used for the analysis of problems concerning a half-space weakened by a set of edge or internal cracks. An attempt could also be made to use this solution to analyze problems of single cracks or sets of cracks under the surface of a half-space or internal curvilinear macroinclusions or holes. Furthermore, the singular integral equations method may be used in future to solve problems of bilateral contact, with the assumption that both the half-space and the punch are not rigid.

## REFERENCES

1. Bryant M.D., Miller G.R., Keer L.M. (1984), Line Contact Between a Rigid Indenter and a Damaged Elastic Body, *Q. J. Mechanics Appl. Mathematics*, Vol. 37, 467-478.
2. Dag S., Erdogan F. (2002), A Surface Crack in a Graded Medium Loaded by a Sliding Rigid Stamp, *Engng Fract. Mech.*, Vol. 69, 1729-1751.
3. Datsyshyn O.P., Panasyuk V.V., Pryshlak R.E., Terlets'kyi A.B. (2001), Paths of edge cracks in rolling bodies under the Conditions of Boundary Lubrication, *Materials Science*, Vol. 37: 363-373.
4. Fujimoto K., Ito H., Yamamoto T. (1992), Effect of Cracks on the Contact Pressure Distribution, *Tribology Transactions*, Vol. 37, 683-695.
5. Galin L.A. (1980), *Contact Problems of the Theory of Elasticity and Viscoelasticity*, Nauka, Moscow, (in Russian).
6. Goshima T. (2003), Thermomechanical Effects on Crack Propagation in Rolling Contact Fatigue Failure, *Journal of Thermal Stresses*, Vol. 26, 615-639.
7. Goshima T., Hanson M.T., Keer L.M. (1990), Three-Dimensional Analysis of Thermal Effects on Surface Crack Propagation in Rolling Contact, *Journal of Thermal Stresses*, Vol. 13, 237-261.
8. Goshima T., Kamishima Y. (1994), Mutual Interference of Multiple Surface Cracks Due to Rolling-Sliding Contact with Frictional Heating, *JSME International Journal Series A*, Vol. 37: 216-223.
9. Goshima T., Kamishima Y. (1996), Mutual interference of Two Surface Cracks in Semi-Infinite Body Due to rolling contact with Frictional Heating by a Rigid Roller, *JSME International Journal Series A*, Vol. 39, 26-33.
10. Goshima T., Keer L.M. (1990), Thermoelastic Contact Between a Rolling Rigid Indenter and a Damaged Elastic Body, *Journal of Tribology, Transactions of the ASME*, Vol. 112, 382-391.
11. Goshima T., Soda T. (1997), Stress Intensity Factors of a Subsurface Crack in a Semi-Infinite Body Due to Rolling/Sliding Contact and Heat Generation, *JSME International Journal Series A* 40, 263-270.
12. Guler M.A., Erdogan F. (2007), Frictional Sliding Contact Problems of Rigid Parabolic and Cylindrical Stamps on Graded Coatings, *International Journal of Mechanical Sciences*, Vol. 49, 161-182,
13. Hasebe N. (1981), An Edge Crack in a Semi-Infinite Plate Welded to a Rigid Stiffener, *Proc. Jap. Civ. Eng.*, Vol. 314, 149-157.
14. Hasebe N., Okumura M., Nakamura T. (1989), Frictional Punch and Crack in Plane Elasticity, *ASCE, J Eng. Mech.*, Vol. 115, 1127-1149.
15. Hasebe N., Qian J. (1995), Circular inclined punch problem with Two Corners to Contact with a Half-Plane with a Surface Crack, In: *Proc. 2<sup>nd</sup> Int. Conf. Computational Methods in Contact Mechanics.*, Computational Mechanics Publications, Southampton, Boston, 159-166.
16. Hasebe N., Qian J. (1997), Circular Rigid Punch with One Smooth and Another Sharp ends an a Half-Plane with Edge Crack, *Journal of Applied Mechanics*, Vol. 64, 73-79.
17. Hasebe N., Qian J. (1998), Edge Crack Due to Circular Rigid Punch in Incomplete Contact, *Mechanics of Materials*, Vol. 28, 271-279.
18. Hills D.A., Nowell D. (1994), *Mechanics of Fretting Fatigue*, Kluwer Academic Publishers, Dordrecht/Boston/London.
19. Hills D.A., Nowell D., Sackfield A. (1993), *Mechanics of Elastic Contact*, Butterworth, Oxford.
20. Keer L.M., Bryant M.D. (1983), A Pitting Model for Rolling Contact Fatigue, *Trans ASME, Journal of Lubrication Technology*, Vol. 105, 198-205.
21. Keer L.M., Bryant M.D., Haritos G.K. (1982), Subsurface and Surface Cracking Due to Hertzian Contact, *Trans ASME, Journal of Lubrication Technology*, Vol. 104, 347-357.
22. Muskhelishvili N.I. (1962), *Some basic problems of the Mathematical Theory of Elasticity*, Nauka, Moscow, (in Russian).
23. Okumura M., Hasebe N., Nakamura T. (1990), Crack due to Weld Shaped Punch With Friction, *ASCE, Journal of Engineering Mechanics*, Vol. 116, 2173-2185.

24. **Panasyuk V.V., Datsyshyn O.P., Marchenko H.P.** (1995), Contact Problem for a Half-Plane with Cracks under Action of a Rigid Punch on its Boundary, *Physicochemical Mechanics of Materials*, Vol. 31, 7-16.
25. **Panasyuk V.V., Datsyshyn O.P., Marchenko H.P.** (2000), Stress State of a Half-Plane with Cracks under Rigid Punch Action, *International Journal of Fracture*, Vol. 101, 347-363.
26. **Qian J., Hasebe N.** (1997), Circular Rigid Punch on a Semi-Infinite Plate with an Oblique Edge Crack Subjected to Concentrated Forces on Point Dislocations, *Proc. Jap. Civ. Eng.*, Vol. 570, 149-159.
27. **Savruk M.P.** (1981), *Two-Dimensional Problems of elasticity for Bodies with Cracks*, Naukova Dumka, Kiev, (in Russian)
28. **Savruk M.P., Madenci E., Shkarayev S.** (1999), Singular Integral Equations of the Second Kind with Generalized Cauchy-Type Kernels and Variable Coefficients, *International Journal of Numerical Methods in Engineering*, Vol. 45, 1457-1470.
29. **Savruk M.P., Tomczyk A.** (2010), Pressure with friction of an Absolutely Rigid Punch on an Elastic Half-Space *with Cracks*, *Physicochemical Mechanics of Materials*, Vol. 46, No 3, 5-15.
30. **Tomczyk A.** (2011), The Effect of Crack on Contact Pressure Distribution in a Plane Problem Accounting for Friction, *Acta Mechanica et Automatica*, Vol. 5, No 1, 106-113.

The investigations described in this paper are a part of the research project No SWM/1/13 realized at Białystok University of Technology.